Digitally Controllable Large-scale Integrated Microfluidic Systems

LAM Raymond Hiu-wai

A Thesis Submitted in Partial Fulfillment
of the Requirements for the Degree of
Master of Philosophy

in

Automation and Computer-aided Engineering

June 2005

ABSTRACT

Due to the maturing MEMS technology, research in microfluidics has advanced rapidly in the past decade. The polymer-MEMS fabrication technology realized the development of biocompatible devices, which was requisite in Bio-MEMS applications. With various microfluidic devices, many operations on chemicals and bio-fluids could be miniaturized to micro-liter scale. Therefore, developing a technology to integrate polymer-based microfluidic devices into a system would be a contributing direction of the research in microfluidics.

This thesis describes several types of polymer-based vortex micropumps and piezoelectric active micromixers developed by the author. In a vortex micropump, fluid transmission with steady flow rate is driven by the circumrotating motion of the impellers. The discharge and pressure of micropumps have been investigated with experiments and an analytical model. The operation principle of the mixer is based on the mechanical vibration generated by a lead zirconate titanate (PZT) ceramic diaphragm. The characterization of micromixers has also been analyzed through experiments. The microfluidic devices discussed in this thesis can be fabricated with a compatible fabrication process and are all digitally controllable. Therefore the devices can be integrated into a single-chip system that can be controlled by digital signals.

Two integrated microfluidic systems, 1) microfluidic flow planning system and 2) microfluidic mixing module array, were also successfully developed. The flow planning system was designed and fabricated with four microchambers and sixteen vortex micropumps. Based on the experimental result of the micropumps, a computer-controllable system, which consisted of multiple voltage generators, was also developed for the real-time microfluidic operation control. The approach of integrating an array of vortex micropumps with the control system will eventually automate many bio-molecular detection and drug discovery processes. Furthermore, the mixing module array integrated with active microfluidic mixers, micro vortex pumping devices and tesla microvalves were successfully fabricated using a single polymer-based fabrication process. The integrated mixing module further demonstrated the feasibility of chemical mixing and concentration control. The digitally controllability of the pumping and mixing systems could improve the accuracy, efficiency and, hence, the functionality of the microfluidic operations. Further integration of the microfluidic systems with other micro-sensing or micro-valving devices can potentially miniaturize the entire bio-fluid/chemical preparation systems in the future.

Submitted by Raymond Hiu-wai Lam

Supervised by Professor Wen J. Li

ABSTRACT (CHINESE)
摘要

現今微電機系統技術變得成熟，微流體學在近十年得以大大發展。基於聚合物的製程技術實現了其生物微電機系統所須的生物相容性。化學藥品及生物液體的處理程序亦能以多種微流體器件縮小至微公升的容積單位。因此，開發一種將微流體器件組成系統的技術將會有助於微流體學的研究發展。

此論文描述了多種新開發的聚合物製的微泵和壓電式主動微混合器。對於微泵，葉輪片的旋轉是用作推動液體的流動，其流量及水壓會以實驗探討。而微混合器的運作則是基於壓電性所產生的振動，其特性亦會以實驗作分析。所有在此討論的微流體器件也具有相容的製程及數控特性。由此可知，以這些器件組成的單片系統亦能以數字信號操控。

兩種合成微流體系統(微流體水流導向系統和微流體混合組列)已成功研製。水流導向系統擁有四個水腔和十六個微泵。基於微泵的性能，一個具有多個電壓輸出的計算機可操控系統已製成並滿足實時微流體運作的要求。此種以微泵及數控系統的組合方式將能使多種生物份子和藥物的測試程序自動化。另外，微流體混合組列是由主動混合器、旋渦式微泵和特斯拉微活門以單一的聚合物製程所製成。這系統能進一步展示其化學藥物的混合功能和濃度控制。這兩種輸水及混合系統的數控性質能改善其運作的精確度、效率以及功能。以此系統與其他微測量或微活門器件作進一步組合將可以令整個生物液體/化學藥品產成系統得以微型化。

ACKNOWLEDGMENT

I would like to express my most sincere gratitude to my supervisor Professor Wen Jung Li, who has given me the invaluable opportunity to work in the laboratory since I was only a first year undergraduate student. I also thank him for his assistance, guidance, encouragement and kindly consideration, especially when I had difficulties in my research work. I am so grateful that Professor Li has educated me a lot with not only the academic knowledge, but also the appropriate attitude to solve problems.

I sincerely thank Professor Michael Yu Wang, Professor Aaron HO Pui Ho and Professor Gwo-Bin Lee for serving as my graduate committee members, providing me many contributing comments and revising this manuscript with their patience and kindly judgment. I would like to thank also Professor Ruxu Du for giving me suggestions in my yearly presentation.

Many thanks go to all my close colleagues in the CMNS team. I was indebted to them throughout either formal or casual discussions. Particularly, I would like to thank Thomas Lei for his previous work on the vortex pump development. I also thank Johnny Lee, who has been saying 'Hello' with me throughout the previous years. Hearty thanks to my friends Simon Tong, Harry Ng, Tak Sing Wong, Turkey Kwok, Joe Wong and Davey Fong for sharing my worry and happiness throughout my university life in Hong Kong.

Finally, a big thank you to my parents, Kam Por Lam and Chun Lung Ip, and my brothers, Alan and Josh. I believe they will know how much I thank them when they read this. I also thank my experiences in these years that pushed me to grow up and provided me many unique and unforgettable memories.

CONTENTS

LIST OF FIGURES

CHAPTER
ONE

INTRODUCTION

1-1 OVERVIEW OF MEMS AND MICROFLUIDIC TECHNOLOGIES

1-1-1 Microelectromechanical Systems (MEMS)

Since early 1960s, integrated circuit fabrication was developed and enabled many laboratories to design and fabricate manifold integrated circuits (ICs). Some of the ICs included sensing and actuating components and greatly enhanced the applicability of the electronic chips. This kind of devices can be categorized as MEMS, which is defined as the device or system containing functional components, by electromechanical or electrochemical means, of sizes in 1 micrometer/micron (μm) to 1 millimeter (mm) [1]. The mature development of MEMS has given a great impetus to improve the preciseness, robustness and operation performance of microsystems in the past decade.

With the MEMS technology, miniaturized systems could be designed as either sensors or actuators, such as micromotors [2], microaccelerometers [3], microgyroscopes [4], microtubrines [5], inkjet print heads and micro-optical switches. In the silicon-based microsystems, energy transduction was typically based on electrostatic force, electromagnetic force, thermal expansion, piezoelectricity, electrokinetic effect, capacitive force, polymerase chain reaction (PCR), etc [6]. This rapidly extended the applications of MEMS in many areas such as, inertial measurement, microfluidics, optics, pressure measurement and radio-frequency (RF) devices.

The technologies used to manufacture such miniaturized devices are called microfabrication or micromachining technologies [6]. In the early stage of the MEMS fabrication development, the substrate of most MEMS devices was restricted to silicon wafer. Photolithography, thermal oxidation, physical/chemical vapor deposition focused only on the silicon-compatible micromachining processes [1]. Since the past decade, MEMS devices could also be fabricated on non-silicon substrates due to the mature Polymer-MEMS fabrication technology [7]. Such technology enabled micro-devices and microsystems to achieve the biocompatibility and, hence, to improve greatly on the applicability. One of the reformed areas was the Bio-MEMS application. The existing treatments on chemicals and bio-fluids, which contained organisms such as DNA and living cells, could also be miniaturized to micro-liter scale. Consequently, it induced the great demand on the development of the MEMS for micro-fluid treatments, i.e., the microfluidic systems.

1-1-2 Microfluidic Systems

Research on microfluidics has developed rapidly in the past years – from single channel devices [9] to complicated and multifunctional systems integrated with manifold microfluidic devices [10]. A Microfluidic system is defined as a system composed of one or more of the various microfluidic devices and it usually has chip area in the order of 1 cm^2 with several layers. Research in microfluidic device have emerged as a hot area and has been an essential branch of MEMS (It can be indicated by the increment of research publications from 1989 to 2000 as shown in Figure 1). Micropump [11] – [13], microvalve [14] – [15], micromixer [16] – [17], microneedle [18] and microfluidic flow sensor [19] are some of the key microfluidic devices. Researchers have contributed to both of the implementation and theoretical analyses [20] – [22] on each device.

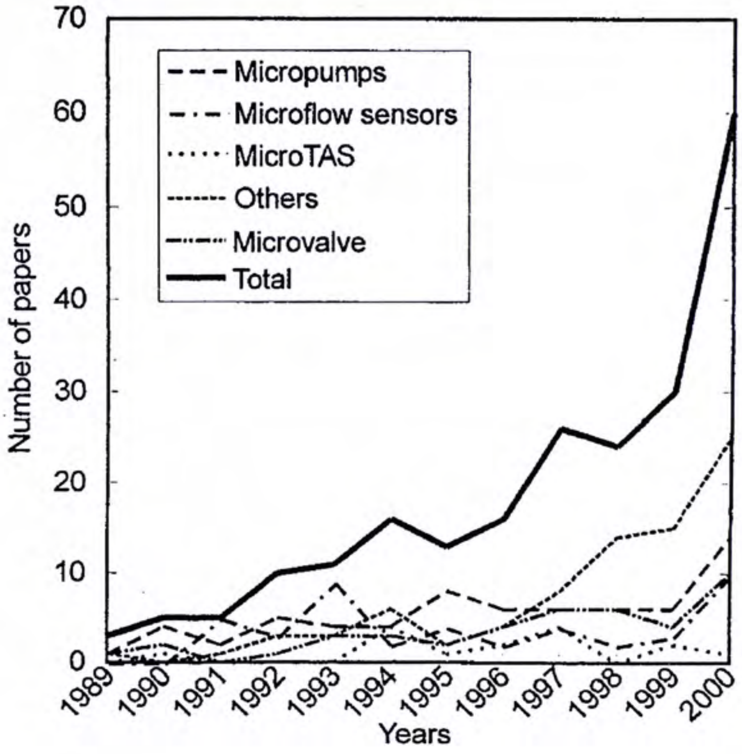

Figure 1. Publications of microfluidics-related papers in international journals and conferences [8].

Device material is an important issue since many microfluidic devices are used in the applications of biochemistry and life sciences [23]. Therefore, the structural material of microchambers and microchannels is necessary to be transparent, chemically inactive and biocompatible. Otherwise, the chemical reactions between structural materials and fluid samples will affect the sample properties and should be avoided. With the advancement of MEMS technology, contemporary microfluidic devices can have complicated structures and multiple layers and are no longer restricted to silicon-based. Polymer has been a vital material in microfluidic devices since it fulfills the above criteria, especially in bio-optical detection applications. Polymer-based microfluidic devices can be used in wide scope of applications. Many designs of the polymer-based devices have borrowed the concept of the traditional MEMS fabrication technique, i.e., the "layer-by-layer" fabrication. Moreover, with the channels and chambers made by polymer, microfluidic devices can reduce superfluous effects in their operations.

Due to the superior performance of the existing microfluidic devices, biological and chemical sensing systems and analyses can be practically miniaturized. However, besides improving the signal acquisition capabilities of these miniaturized sensing systems, the preciseness of biochemical sample preparation and handling is also a vital requirement for the system miniaturization. This makes the integration of microfluidic devices become the next challenge of the microfluidic technology.

1-2 LITERTURE REVIEW ON MICROFLUIDIC DEVICES

1-2-1 Micropumps

Micropump is an actuator that provides pressure to induce fluid flow inside a microchannel. In the device design, the main concerns are its occupied area, the applied voltage (or power), the flow rate induced and how much back pressure it can overcome. Some of the micropumps attain flow rates up to 1 ml/min and some are able to work against a back pressure higher than 105 Pa [24]. The lead zirconate titanate (PZT) valveless rectification micropump [25] is one of the conventional micropumps. The nozzle geometry of the inlet and outlet channels can increase the unidirectional back pressure. The rectification property can also be achieved by check valves [26]. Rotary micro-pumping is another type of mechanical pumping approach, which can be based on electromagnetic force [27] or a compact disc (CD) platform [28]. Furthermore, fluid flow can also be driven by non-mechanical actuation forces such as electrophoresis force [29] and electro-osmosis effect [30].

1-2-2 Microvalves

Microvalve is an important microfluidic component for fluidic flow control. The device size, response time, pressure resistance and biocompatibility are the major considerations in microvalve design. A passive valve does not require any external driving energy. Such device is usually applied in micropumps to reduce the fluid flow in a particular direction, which is called the rectification effect. Check valve [31], diffuser [32] and tesla valve [33] are some of the typical designs. Besides, active microvalves can be actuated by various forces such as pneumatic, thermomechanical [34], piezoelectric [35] and electrostatic forces [36]. Moreover, the active valves can be operated with other microfluidics components and, so, enable the internal flow control capability of the microfluidic devices.

1-2-3 Micromixers

For more complicated microfluidic systems, mixing of more than one fluid is often required. Fluid mixing is affected by the diffusion rate and the turbulence of fluid flow. However, because of the channel dimension, most fluid flow in microfluidic devices is laminar. Consider the Reynolds number (Re) of the flow inside a microchannel,

$$\mathrm{Re} = \frac{\rho V D}{\mu} \tag{1.1}$$

where ρ is the fluid density; μ is the viscosity coefficient; V is the flow velocity and D is the length scale of flow, which is in the order of 10^{-4} m in microchannels. Re is very small (<< 1000) in microchannel flows, so it is necessary to design micromixers to enhance the mixing rate of fluid. The first micromixer uses four hundred micronozzles inside a microchamber to increase the fluid diffusion rate [37]. This micromixer is defined as a passive micromixer since no external energy is used to induce the turbulence of fluid flow and enhance the mixing rate of fluid. Other examples of the passive micromixing principles are parallel lamination and sequential lamination [38]. Moreover, micromixing can also be enhanced by actuation forces. Acoustic streaming and magneto hydrodynamic force are feasible mixing methods, which have been practically demonstrated ([17], [39] and [40]). The active micromixers can provide adjustable mixing rate, so they are more flexible in the microfluidic applications.

1-2-3 Integration of Multiple Devices: Microfluidic Systems

Integrating individual microfluidic devices into systems could miniaturize and intensifying many fluidic processes. The approach of microfluidic integration with external fluidic connection is called modular integration. Many research groups demonstrated various modular integrated microfluidic systems with promising operation performance [41] – [42]. Nevertheless, the systems did not standardize the fluidic and electrical connections and so they were inconvenient for chip reconfiguration. A stacked modular integration approach, which was developed by the Motorala Labs [43], provided a more universal connection mechanism on an electrical circuit board platform. Multiple microfluidic chips could be vertically plugged into the sockets on the electrical circuit base board while fluidic connection was achieved by linking the passageways between chip modules.

Furthermore, the large-scale integrated microfluidic systems comprising of valves and channels using multiplayer soft lithography were developed by Quake's group in Stanford University [10]. The microfluidic chips consisted of thousands of microvalves and hundreds of microchambers, which could potentially perform multiple bio-optical detection tasks. However, due to the limitations on fabrication processes, they could not integrate pumps or mixers into their chips. Furthermore, two silicon-based single chip integrated systems designed for multiphase mixing and reaction were developed by the MicroSystems Technology Laboratories of Massachusetts Institute of Technology [44]. In the first system, filter-like structures were fabricated near the outlets to accumulate catalytic particles and, so, to conduct heterogeneously catalyzed multiphase reactions. The other system trapped catalytic particles with an array of 50 μm diameter columns, which provided an additional mixing capability. It is believed that the functionality of integrated microfluidic systems can be greatly enhanced by further integrating with the miniaturized detection devices.

1-3 MOTIVATION AND RESEARCH OBJECTIVES

The integration of microfluidic devices is a great challenge in the advancement of microfluidic technology. In microelectronics manufacturing, the external connection often involves only electricity. However, the fluidic connection is also an essential factor in microfluidic systems. The preparation of fluids becomes an important issue for the system operations such as the tiny gas bubble filtering and the insufficient mixing rate due to the low Re laminar flow in microchannels.

On the other hand, the operations of microfluidic systems involve fluid transmission, fluid multiplexing, fluid mixing, temperature and electrical potential controls, etc. Some of the applications require complicated microfluidic systems, so designing microfluidic chips for specific applications may not be a cost effective approach. To achieve the microfluidic system with adjustable or even programmable functionality, all the microfluidic components in the system need to be digitally controllable. Hence, the development of small, low voltage-required microfluidic devices can highly improve the applicability of microfluidic systems.

The structures of microfluidic devices are needed to be high aspect ratio. And optically transparent materials have to be used for bio-optical detection applications. In addition to the traditional polymer photolithography, micro molding replication technique [45] – [47] of transparent materials is a feasible approach to achieve the cost effectiveness and capability of bio-optical detections.

The major objective of this research project is to develop integrated microfluidic systems that can perform digitally controllable operations on micro-fluid delivery and mixing, which are the most fundamental issues of the microfluidic operations. And such systems can be further integrated with other detection and manipulation devices, as an essential technology upon the multi-functional digitally controllable microfluidic systems. As mentioned previously, micropumps, micromixers and microvalves should also be developed with compatible the fabrication processes, such as 1) polymer photolithography, and 2) micro molding replication technique. Characterization of the developed devices is needed to be investigated, and potentially help develop a technology for the device operation and integration. Furthermore, a computer-controllable electronic system would also be designed based on the input signal requirements of the individual microfluidic devices. Integrating the control system with the fluid manipulation and preparation chips could potentially achieve fast and precise microfluidic operations and potentially automating the bio-fluidic processes, for example the (SPR) detection [48].

1-4 THESIS OUTLINE

Chapter 1 introduces an overview of the existing MEMS and microfluidics technology. This includes various device designs, actuating and sensing principles. The objectives of the research project and this thesis outline are described in the latter sections. *Chapter 2* provides the fundamental theory on microfluidic flow, including the velocity profile, the pressure reduction and the bubble filtering technique. The preliminary understanding is useful to the device/system design considerations and the experimental results analysis presented in this manuscript. *Chapter 3* describes the details of polymer-based vortex micropumps. The design and fabrication of different micropumps and rotary impellers are presented. It also discusses the principal design parameters based on the macro centrifugal pump theory, which can help analyze the experimental results described in the last section of this chapter. *Chapter 4* presents two types of polymer-based mixers: the flat-surface diaphragm (FSD) and the pillared-surface diaphragm (PSD). This also involves the design, fabrication and performance characterization of both mixers. *Chapter 5* describes an integrated microfluidic flow planning system based on the modular integration approach. The system consists of microfluidic channels, a chamber array and a computer-operated digital controller. An experiment result of multiple fluids delivery is also reported. *Chapter 6* presents the design and fabrication of a microfluidic mixing module array integrated with six vortex micropumps, six tesla valves and three PSD active micromixers. It also presents the operation principle and simulation result of the tesla valve. An approach of the mixing ratio estimation is described. Moreover, the experiment results are reported to illustrate the capability of the digitally-controlled mixing. *Chapter 7* concludes this manuscript and *Chapter 8* addresses the potential future development. *Appendices* include an adhesion test on the UV-epoxy resin, the circuit schematics of the digital controller and an additional microfluidic controlling system with superior functionality for future development.

CHAPTER
TWO

FLUID FLOW IN MICROCHANNEL

2-1 VELOCITY PROFILE IN A MICROCHANNEL

Miniaturization of the bio-optical detection is one of the major applications in the research of microfluidic devices and systems. The structural material is necessary to be transparent so that the characteristics of fluids can be analyzed by the color or flow pattern inside an output chamber/channel. Therefore many microfluidic devices were fabricated with polymers and so the channel geometries were different from that of the silicon-based devices. Besides channel geometry, velocity profile is one of the major factors affecting the flow pattern in a microfluidic device and, hence, the performance of the whole detection process. In this section, the velocity profile inside a microchannel will be discussed.

As a simple analysis, the velocity profile of an internal fluid flow inside a microchannel will be estimated based on the Newtonian laminar flow as illustrated in Figure 2. Distinct from the silicon-based microfluidic devices, the microchannels fabricated with polymer-MEMS technology are often rectangular in shape (width $2X$ and height $2Z$). For a Newtonian laminar flow, the shear stress of a flowing fluid τ is equivalent to that upon the yz-plane and along the y-axis direction $\tau_{yz|y}$ [49]. It also decreases with the horizontal distance z from the center of channel. The flow profile *u(x, z)* on the plane $x = 0$ can be approximated as,

$$\tau = \tau_{yz|y} = \mu \frac{du(0,z)}{dz} = -k_1 z \tag{2.1}$$

where μ is the dynamic viscosity and k_1 is a constant.

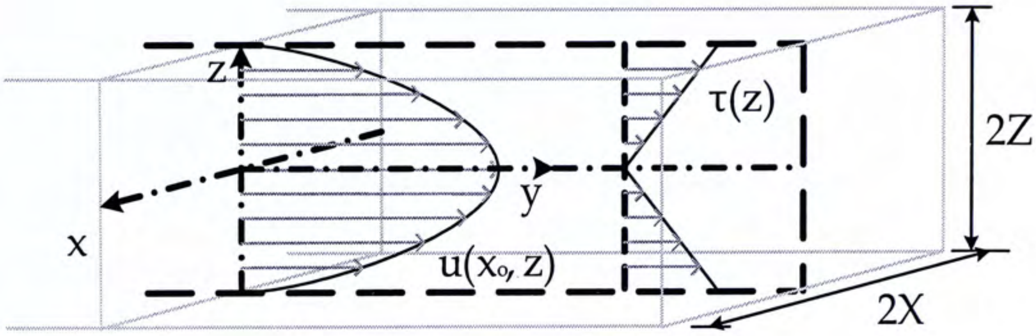

Figure 2. Velocity profile and shear stress distribution of the steady laminar flow in a microchannel.

Integrating the above equation, *u(0, z)* can be resolved as

$$u(0,z) = -\frac{k_1 z^2}{2\mu} + C \tag{2.2}$$

where *C* is a constant.

Substituting the boundary condition $u(0, \pm Z) = 0$, we get

$$u(0,z) = \frac{k_1 Z^2}{2\mu}\left(1 - \frac{z^2}{Z^2}\right). \tag{2.3}$$

Considering a velocity profile on a given plane $z = z_0$, we can obtain the expression similar to equation (2.3), that is,

$$u(x,z_0) = \frac{k_2 X^2}{2\mu}\left(1 - \frac{{z_0}^2}{Z^2}\right)\left(1 - \frac{x^2}{X^2}\right) \tag{2.4}$$

where k_2 is another unknown positive constant.

Since $u(x, z_o)$ for all $z_o \varepsilon z$ can be expressed as equation (2.3) at $x = 0$, equation (2.4) becomes

$$u(x,z) = k\left(1-\frac{z^2}{Z^2}\right)\left(1-\frac{x^2}{X^2}\right) \tag{2.5}$$

where

$$k = \frac{k_1 Z^2}{2\mu} = \frac{k_2 X^2}{2\mu} = u_{\max}\,. \tag{2.5}$$

It is obvious that the flow velocity is maximal along the centerline of channel. The velocity dissipation is mainly due to the shear force constrained by the zero boundary conditions of the channel walls.

In the steady laminar flow condition, the discharge of the microchannel Q is the integral of velocity upon the cross-section area $A = (2X)(2Z)$. Integrating $u(x, z)$ in equation (2.5), we obtain

$$Q = \int u dA = \int_{-Z}^{Z}\int_{-X}^{X} k\left(1-\frac{z^2}{Z^2}\right)\left(1-\frac{x^2}{X^2}\right)dxdz = \frac{4}{9}k(2X)(2Z)\,. \tag{2.7}$$

The average flow velocity V is defined as the discharge over the cross-section area, thereby

$$V = \frac{Q}{A} = \frac{4}{9}k = \frac{4}{9}u_{\max}\,. \tag{2.8}$$

The velocity profile $u(x, z)$ can then be approximated by equations (2.5) and (2.8) with a given discharge value and a cross-section dimension. In the laminar flow, any initial velocity profile would gradually change to $u(x, z)$ after flowing for a certain distance and so $u(x, z)$ is also called the developed velocity profile [49]. A simulated example with an initial flow velocity profile $u(x, 0)|_{y=0} = 1 + \sin(\pi x / 0.06\ [\mu m^2])$, $[cms^{-1}]$ discharge 0.032 ml/min and channel dimension 600 μm × 100 μm is illustrated in Figure 3 (a). The theoretical velocity profile can be calculated as $u(x, 0) = 2 \times (1 - z^2 [\mu m^2] / 100^2)) [cms^{-1}]$. It indicates that the velocity profile at $y = 3$ cm, $u(x,0)|_{y=3[cm]}$, is similar to the expected profile (Figure 3 (b)).

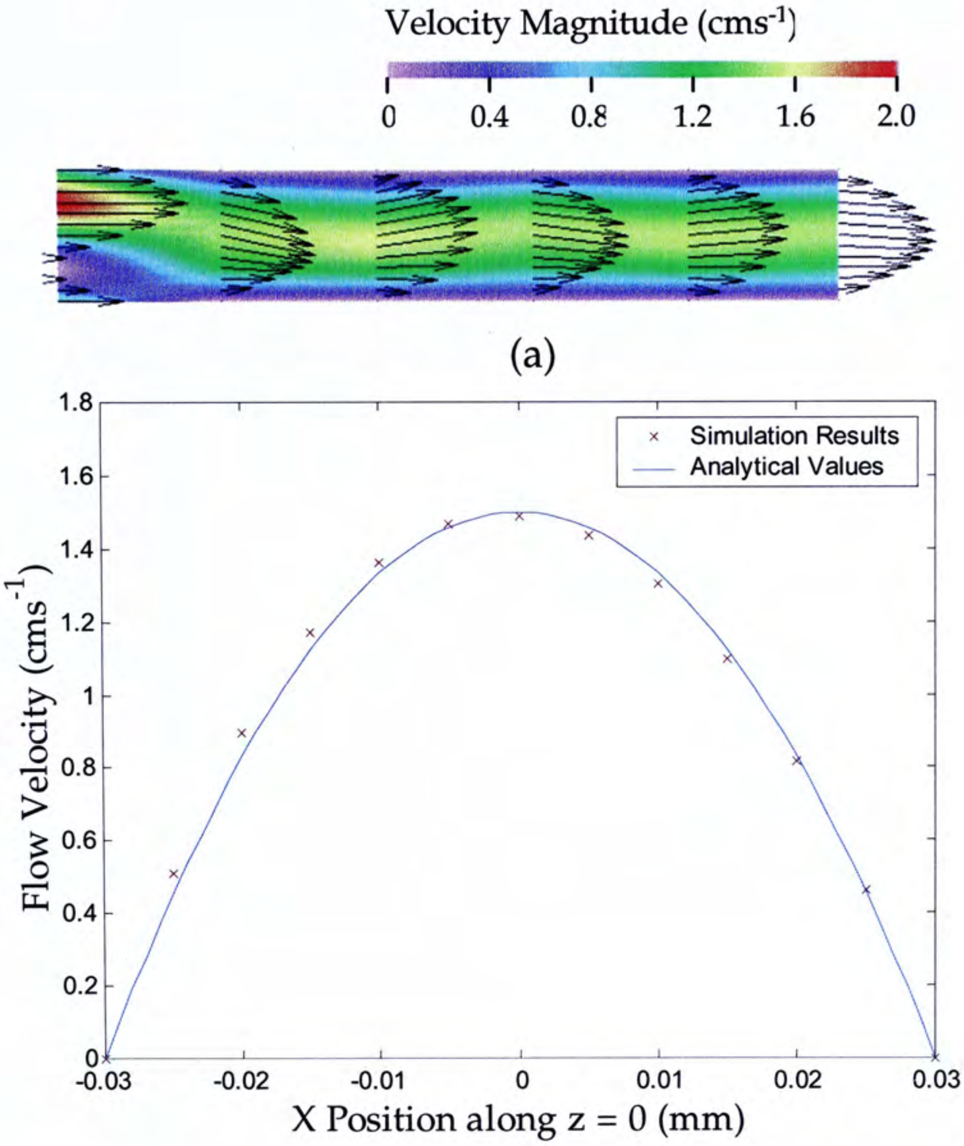

(a)

(b)

Figure 3. (a) Simulated velocity variation and (b) comparison between the simulated and analytical developed profile inside a microchannel.

As mentioned previously, the velocity profile of fluid flow in a microchannel varies little with the geometry change, which is the major factor of insignificant mixing. A simulation experiment on an "L"-shape microchannel is shown in Figure 4 (a). The dimension of channel cross-section (600 μm × 100 μm) and the discharge (0.032

ml/min) are the same as the previous example. In the simulation, the initial velocity was set as the analytical profile in order to investigate the change of flow velocity profile caused by the channel width variation. The simulation result in Figure 4 (b) illustrates that the velocity profile in the "L"-shape channel could be fully developed with a delivery distance $y < 1$ mm.

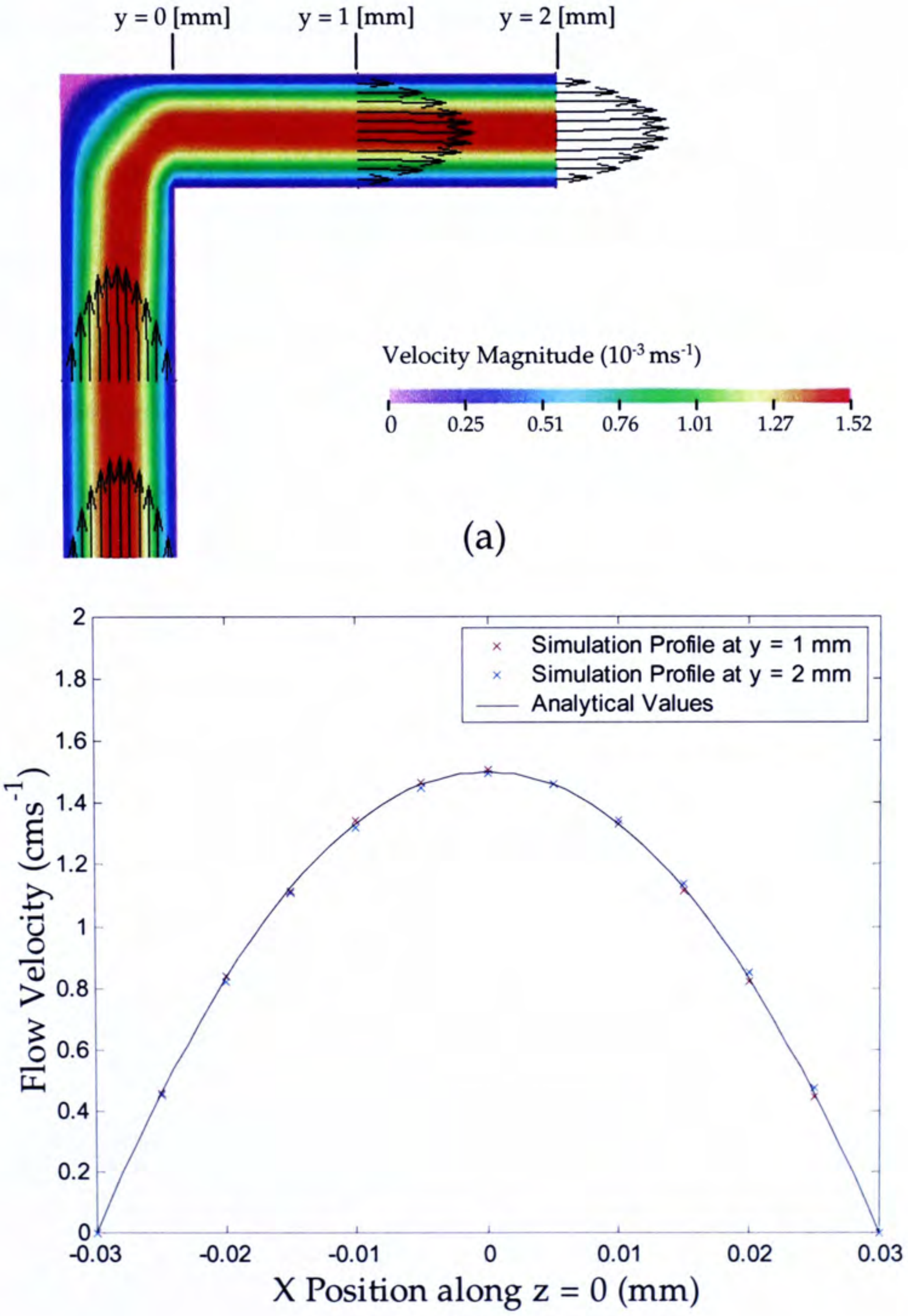

(a)

(b)

Figure 4. (a) Simulated velocity variation and (b) comparison between the simulated and analytical developed profile inside an "L"-shape microchannel.

2-2 PRESSURE DISSIPATION BY LAMINAR FRICTION

In the macro-scale fluid flow, the pressure reduction due to laminar friction along a channel is often negligible. However, the flow pressure would dissipate significantly in a microchannel. In micro-scale steady flow, the flow velocities at the input and output cross sections are equal, which means the portion of fluid is in the equilibrium state. Hence, the net force acting on the fluid in a particular portion with length ΔL should be zero. The force diagram of the steady flow in a microchannel is illustrated in Figure 5. The balanced force is composed of shear force, gravitational force, normal force of the bottom channel wall, and forces induced by input and output flow pressures. The shear force F_{sf} is caused by the viscous resistance between the considered fluid body and its surrounding fluid. It is equal to the flow shear stress along the circumjacent area. Besides, the gravitational force would be cancelled by the normal force of the channel wall. So the net force becomes

$$\sum F = P_1 A_1 - P_2 A_2 - F_{sf} = 0\,. \tag{2.9}$$

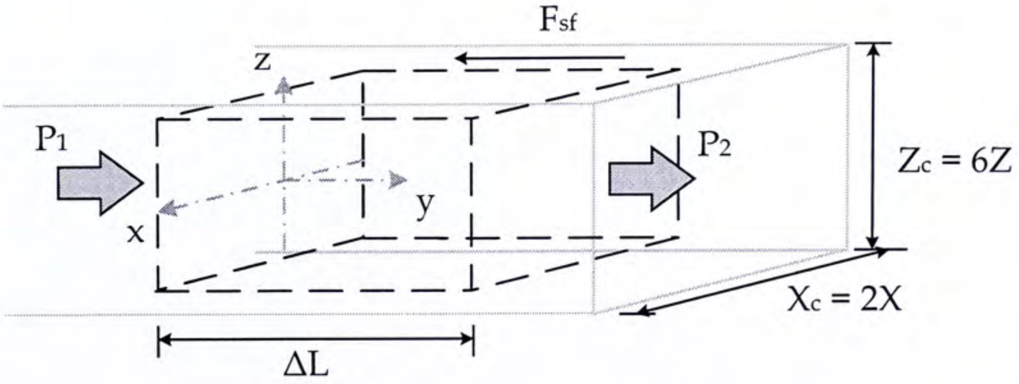

Figure 5. Force diaphragm of the laminar flow inside a microchannel.

Substituting $X_c = 2X$, $Z_c = 2Z$, $P_2 = P_1 + \Delta P_{sf}$ in equation (2.9) and assuming $F_g = 0$,

$$X_c Z_c P_1 - X_c Z_c (P_1 + \Delta P_{sf}) - 2(X_c + Z_c)\Delta L \tau_w - 0 = 0. \qquad (2.10)$$

where τ_w is the shear stress of channel wall.

Rearranging equation (2.10), the pressure reduction by surface tension can be expressed as

$$\Delta P_{sf} = -2\tau_w \Delta L\left(\frac{X_c + Z_c}{X_c Z_c}\right). \qquad (2.11)$$

From the Bernoulli equation, the head loss h_{sf} of a control volume with a horizontal steady-state laminar flow is

$$h_{sf} = \frac{-\Delta P_{sf}}{\rho g} \qquad (2.12)$$

where ρ is the fluid density.

Substituting equation (2.11), the head loss becomes

$$h_{sf} = \frac{4\mu\Delta L}{\rho g D} = \frac{2\tau_w \Delta L}{\rho g}\left(\frac{X_c + Z_c}{X_c Z_c}\right). \qquad (2.13)$$

From the above equation, it is obvious that the hydraulic diameter of the channel is $D = 2\, X_c Z_c / (X_c + Z_c)$. This result can also be used to calculate the Re of a rectangular microchannel [50].

In equation (2.13), the shear stress τ_w can be resolved by the Hagen-Poiseuille flow profile. τ_w can be estimated by the average shear stress along the channel wall surface, that is,

$$\tau_w = \overline{\tau_w} = \frac{\int \tau(x,z)\,|_{x,z\in s}\, ds}{2(X_c + Z_c)} \qquad (2.14)$$

where s represents the set of points along the boundary of a channel cross section.

From equation (2.1) and (2.3), it is shown that

$$\tau_w\big|_{x=\pm X} = \mu \frac{du}{dx}\bigg|_{x=\pm X} = \frac{2\mu u(z)\big|_{\max}}{X} = \frac{2\mu u(0,z)}{X}, \tag{2.15}$$

and
$$\tau_w\big|_{x=\pm Z} = \mu \frac{du}{dz}\bigg|_{z=\pm Z} = \frac{2\mu u(x)\big|_{\max}}{Z} = \frac{2\mu u(x,0)}{Z}. \tag{2.16}$$

Thereby equation (2.14) can be rewritten as

$$\tau_w = \frac{2\int \tau_w\big|_{x=\pm X} dz + 2\int \tau_w\big|_{z=\pm Z} dz}{2(X_c + Z_c)}, \tag{2.17}$$

and so
$$\tau_w = \frac{16\mu k}{3(X_c + Z_c)} = \frac{12\mu V}{X_c + Z_c} \quad \textit{(using equation (2.8))}. \tag{2.18}$$

Therefore, the laminar head loss of a rectangular microchannel becomes

$$h_{sf} = \frac{24\mu V \Delta L}{\rho g X_c Z_c}. \tag{2.19}$$

In addition to the pressure dissipation due to the laminar friction ΔP_{sf}, fluid pressure can also be reduced by the geometry variation ΔP_{gv}. The total pressure loss along a channel for incompressible flow P_{loss} is,

$$P_{loss} = -\Delta P = -\sum \Delta P_{sf} - \sum \Delta P_{gv}\ . \tag{2.20}$$

The geometry factor of pressure loss ΔP_{gv} includes 1) pipe entrance or exit, 2) sudden widening or reduction of channel, 3) gradual channel expansion or contraction, and 4) deformation of channel cross-section or any obstacle inside channel [49]. Though the analytical expressions of the pressure dissipation are complicated, it can be observed with experiments that similar channel geometries would have similar reduction properties. To approximate such pressure reduction, the loss coefficient *K* is used to characterize for the profile singularities. It is a factor of the kinetic energy converted to irreversible internal energy by some impediment to flow. The pressure loss is expressed by

$$\Delta P_{gv} = -\frac{1}{2} K \rho V^2 . \tag{2.21}$$

The factor *K* depends on the shape factor *S*, which is equal to the perimeter ratio between the smaller cross section and the larger cross section of a profile singularity. A simple approximation of *K* (from reference [51]) is

$$K(S) = \begin{cases} (S-1)^2 & \text{, channel enlargement} \\ \left(\dfrac{1}{0.59 + 0.41 S^3} - 1 \right)^2 & \text{, channel reduction.} \end{cases} \tag{2.22}$$

The detailed approximation of *K* can be found in reference [50].

The estimation approach of pressure dissipation can be used in different microfluidc devices. As an example, the approach was applied to a diffuser geometry, with pattern and dimension illustrated in Figure 6. Substituting the parameters of diffuser ($\varDelta L$ = 2000 μm, X_c = 500 μm and Z_c = 100 μm), water (μ = 10e^{-3} kg/ms) and fluid flow ($V = Q / X_c Z_c$ = 1.333 ms^{-1}), the laminar pressure loss of the diffuser $-\varDelta P_{sf}|_{diffuser}$ could be resolved as 0.512 kPa. The pressure loss caused by geometry change could be divided into three portions: the sudden channel reduction at inlet (S_1 = 0.2), the gradual channel enlargement along the diffuser (S_2 = 0.5) and the sudden channel enlargement at outlet (S_3 = 0.4). Hence the overall pressure loss should be estimated as

$$\begin{aligned} P_{loss}\big|_{diffuser} &= -\Delta P_{sf}\big|_{diffuser} + \frac{1}{2}\left[\left(\frac{1}{0.59 + 0.41 S_1^3} - 1 \right)^2 + (S_2 - 1)^2 + (S_3 - 1)^2 \right] \rho V^2 \\ &= 1.264 kPa \end{aligned} \tag{2.23}$$

where ρ = 998 kg / m^3.

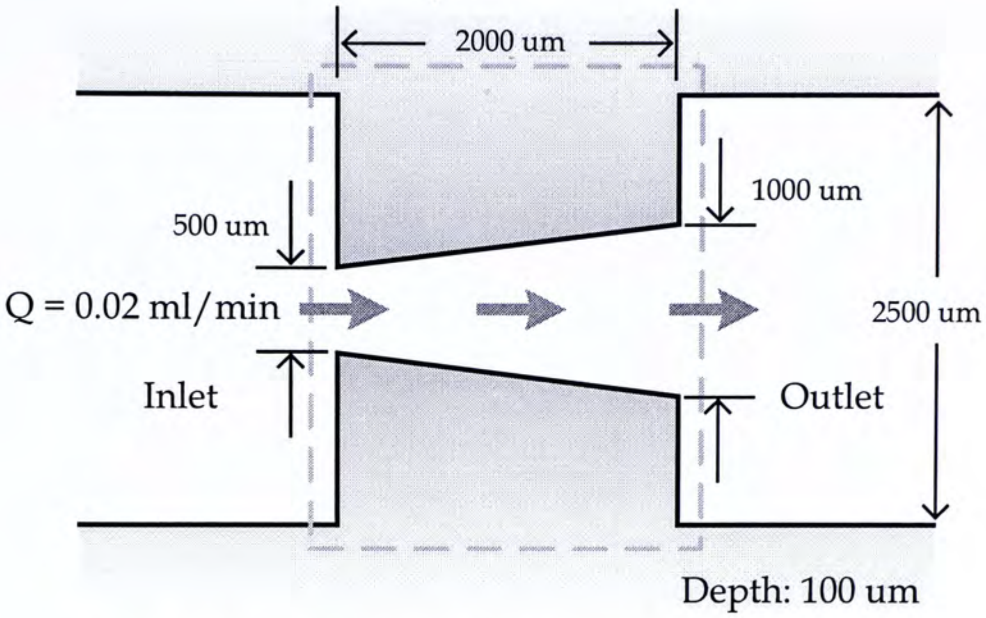

Figure 6. Top view of a diffuser geometry.

2-3 BUBBLE FILTERING

When fluid is delivered into a microfluidic device, some tiny air bubbles would follow the fluid flow and enter the device. The air bubble problem is one of the important issues in microfluidic devices, especially in the integrated systems. Air bubble may greatly affect the operation performance of some devices, by blocking the sub-channel fluid flow or occupying the detection areas in the bio-optical measurement applications. This problem should be particularly avoided in the integrated systems since the failure of a single component would probably impair the functionality of the entire system. Therefore, bubbles should be filtered before delivering them into microfluidic devices/systems.

To eliminate the air bubble problem, a microfluidic device, which included a microchamber with an array of pillars, was designed and fabricated successfully. The pattern of the component is illustrated in Figure 7. The latter half area of microchamber was fabricated with pillars, which were used to filter the air bubbles inside fluids. And bubbles can then be trapped and accumulated at the former half of chamber.

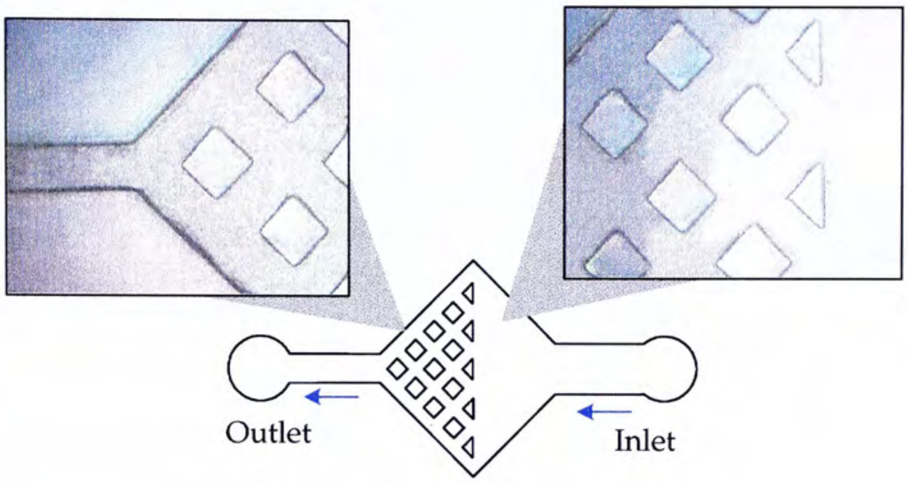

Figure 7. Flow pattern and microscopic images of the bubble filtering module.

An experiment was performed to examine the bubble filtering capability of the device as shown in Figure 8. A bubble from the inlet pipe was trapped inside the microchamber and was avoided further flowing to the outlet. This result indicates that bubbles can be excluded by designing such chamber structure along the microchannels.

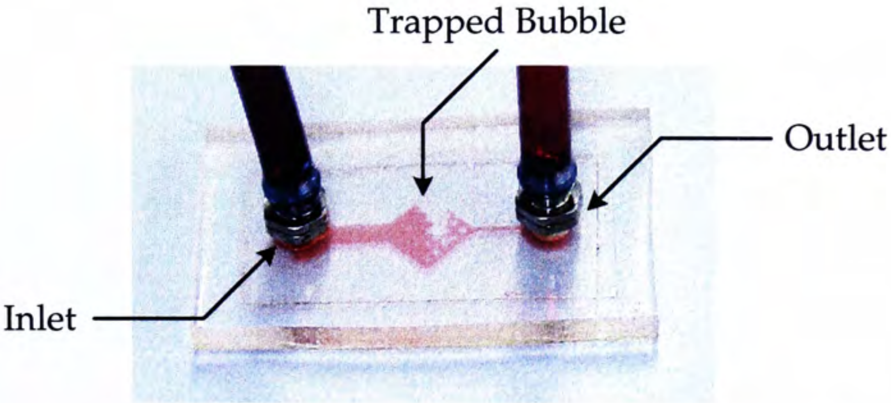

Figure 8. Result of the bubble filtering experiment.

In the initialization stage of microfluidic devices, air bubbles often adhere along the internal surfaces of inlet tubes and inside chambers. And only few more bubbles will be delivered from the inlet reservoirs during operation. Hence, in addition to the inlet channels, the bubble filtering structure should be placed after each microchamber. This configuration would be effective to minimize the internal bubble problem in the microfluidic devices.

CHAPTER

THREE

MICROFLUIDIC CENTRIFUGAL PUMPING

3-1 VORTEX MICROPUMP

3-1-1 Operation Principle and Device Design

A vortex micropump can be viewed as the miniaturized version of a centrifugal pump, a kind of classical rotodynamic pumps. The vortex micropump uses the kinetic energy of an impeller and a circular pump chamber to move fluid. The micro impeller is placed inside the pump chamber. When fluid enters the micropump from the center of impeller axially, the rotating impeller blades would whirl the fluid to the perimeter, tangentially and racially. Hence, fluid pressure and velocity can be induced by the momentum increment of the continuous flow.

The impeller blades can be designed as backward-curved, radical or forward-curved as illustrated in Figure 9 (a), (b) and (c), respectively. Different designs of impeller blades slightly affect, mainly, the pressure enhancement of the micropump (The details will be discussed in section 3-3-3). The forward-curved design could cause pump surge when the impeller rotates at certain rotation speed [49]. The surge may greatly reduce the stability of pumping pressure and velocity thereby the backward-curved and radical blades are often applied in the impeller design.

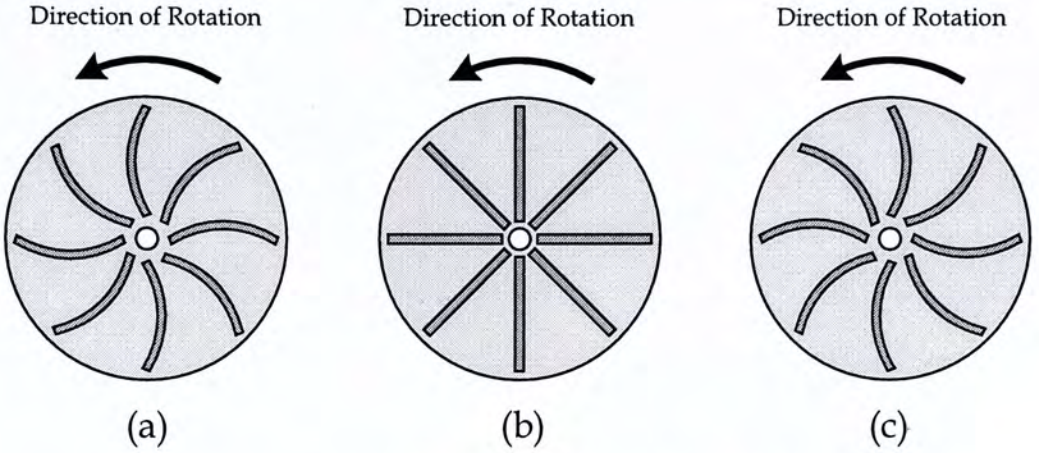

(a) (b) (c)

Figure 9. Top views of impellers designed with (a) backward-curved, (b) radical and (c) forward-curved blades.

A fabricated vortex micropump module (length 30 mm, width 20 mm and height 18 mm) consists of two layers of structures as shown in Figure 10. The top layer structure provided inlet and outlet connections while the bottom layer contained a pump chamber, right below the inlet, and a flow channel. An impeller was mounted inside the 5 mm diameter pump chamber and was driven by a DC motor. The rotation of impeller, with diameter 4 mm, would induce pump pressure and velocity as mentioned previously.

Since microfluidic devices are required to be transparent for bio-optical detection applications, we chose polymethyl methacrylate (PMMA) to be the structural material for both layers. The chamber and microchannel profiles of the micropump have been successfully fabricated by the micro molding replication technique and the photolithography of SU-8 negative photoresist. Detailed fabrication processes of both impeller and pump configuration designs will be presented in section 3-2.

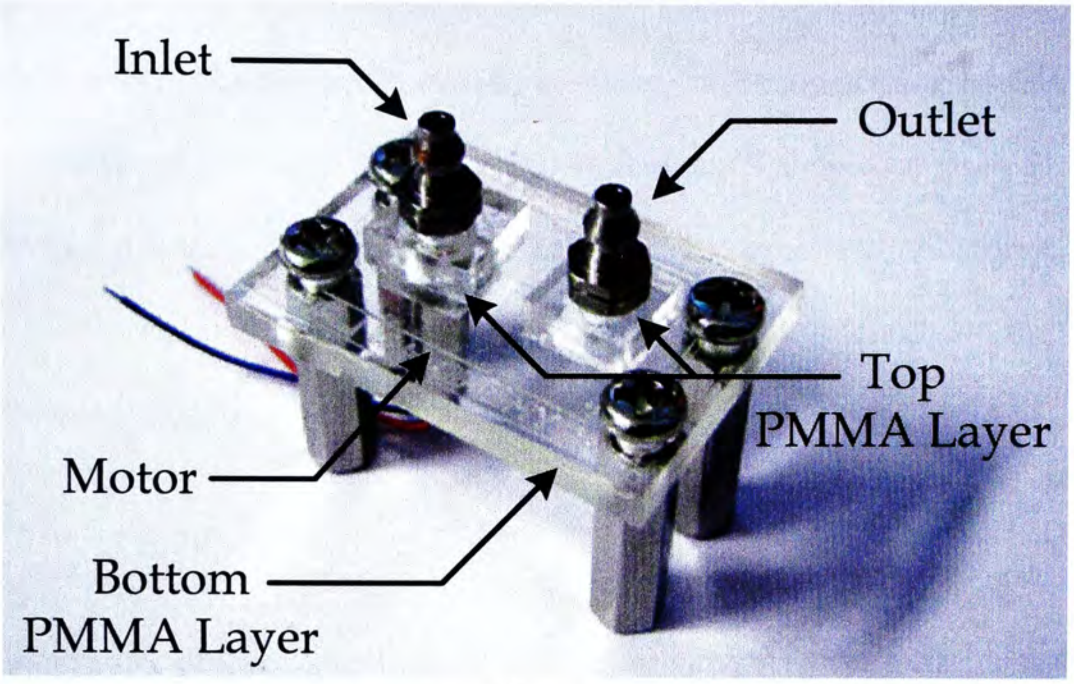

Figure 10. Photograph of a fabricated vortex micropump.

In the device design, the vortex micropump could transmit fluid through a 500 μm wide and 80 μm deep microchannel. Microchannels were enclosed by attaching a layer of polyester on the canaliform patterns on the bottom PMMA layer. The design of microchannel is one of the major factors of the pumping performance. A micropump containing flow channel with smaller cross-section area can resist higher back pressure and deliver with lower pump rate, and vice versa.

3-1-2 Alternative Pump Design

In the previous design, the motor is mounted below the PMMA substrate. Because of the length of motor (11 mm), stands should be added to lift up the whole device. The configuration is insignificant to the pumping performance, but this would highly increase the device height and constrain the compatibility to integrate with other microfluidic devices into a single substrate. The micropump stands can be eliminated by the modifications on motor orientation and channel path arrangement. The fluid in microchamber can be supplied from the bottom, instead of the top as the original design. The motor can then be mounted on the top of the substrate using the inverted-chamber design. Besides, the output channel should be retained at the upper part of chamber. Fluid would fill up the entire microchamber before flowing into the output channel. This configuration is also effective to eliminate the initial air-trapping problem inside the chamber.

The fabrication of the inverted-chamber micropump is slightly more complicated than the original process. SU-8 layers should be fabricated on both sides of the PMMA substrate. The microchannels on the top and bottom sides can be connected by drilling 1 mm diameter holes through the PMMA substrate. The inverted-chamber design can be achieved by the modified microchannel route as illustrated in Figure 11 (a). Fluid can flows into the microchamber through the channel at the bottom SU-8 layer (broken line in Figure 11 (a)). A fabricated product without stands at the device corners is shown in Figure 11 (b).

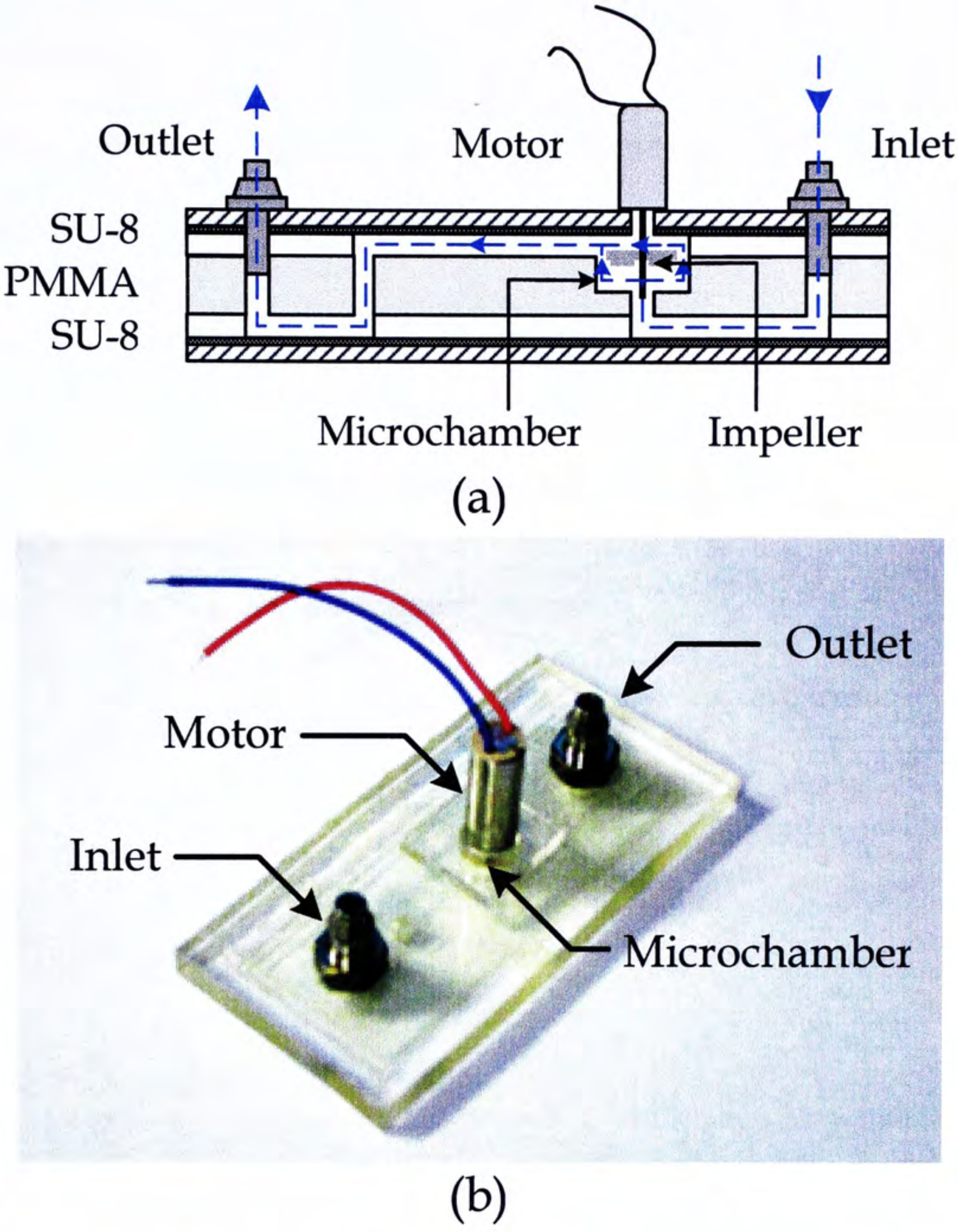

Figure 11. (a) Schematic and (b) photograph of the vortex micrompump fabricated with the inverted-chamber design.

3-2 MICROPUMP FABRICATION

3-2-1 Electroplated Impeller

The rotating impeller is used to induce pressure and generate the fluid flow. The fabrication process of the single layer nickel structured impeller is shown in Figure 12. A layer of 200 μm thick SU-8 negative photoresist should be spun on a nickel substrate and be exposed under UV light with the mask of impeller pattern. After developing the SU-8 layer, a 100 μm thick nickel layer should be electroplated on the substrate. The micro impeller can then be fabricated after removing the nickel and SU-8 substrate.

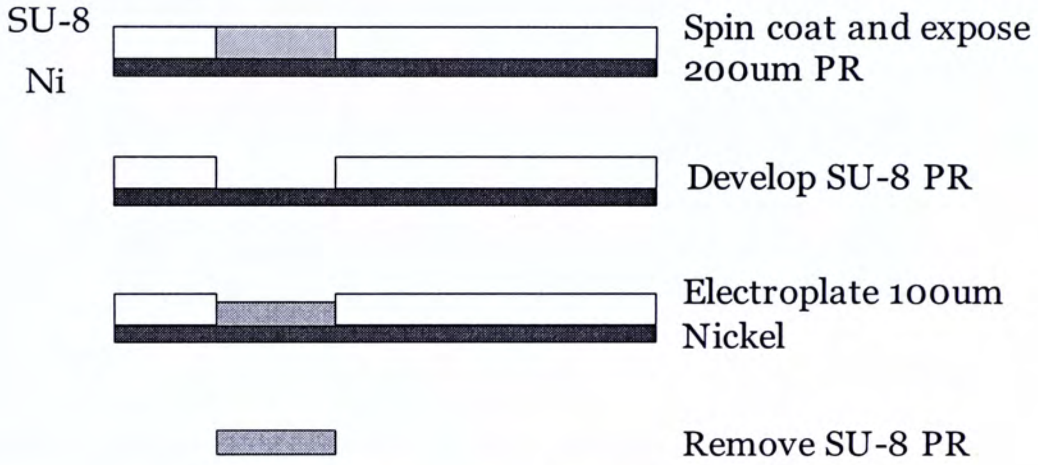

Figure 12. Nickel micro impeller fabrication process [53].

Different designs and dimensions of impellers could be fabricated by the electroplating technique as shown in Figure 13 (a). The top view shape and dimension were defined by the mask design while the impeller thickness was controlled by the electroplating duration. The fringe profile highly depended on the developed edges of the SU-8 layer. An SEM image of the impeller blade (Figure 13 (b)) showed that the edge surface is smooth enough for the pumping application.

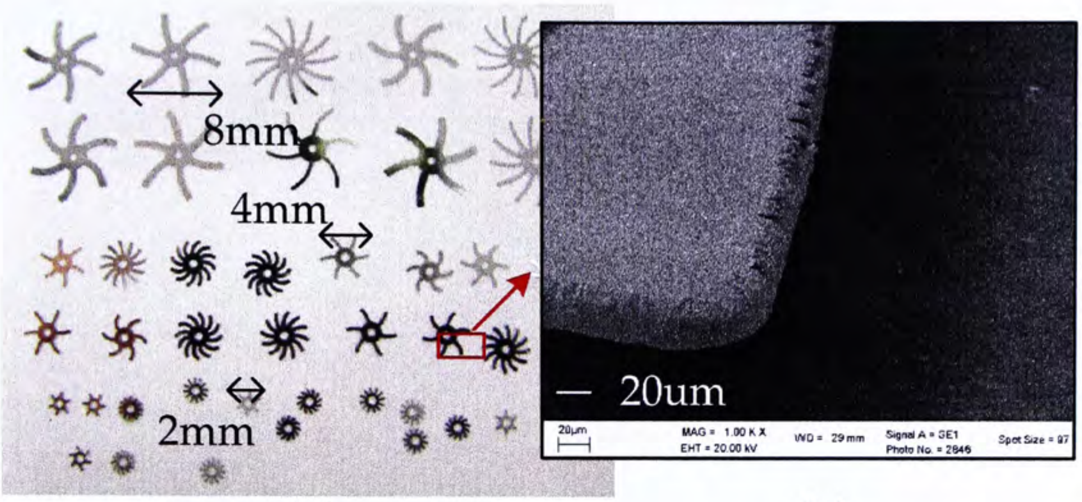

(a) (b)

Figure 13. (a) Photograph of different sizes of nickel micro impellers and (b) SEM image of one edge of the impeller blade.

The pumping performance of the nickel impeller has been improved by a double layer design [52]. Retaining the blade pattern at the top layer, a circular plate was added to the bottom impeller layer at shown in Figure 14. The circular plate could constrain the direction of fluid flow on the plate to be tangential. This modification would greatly increase the pumping efficiency. The fabrication of the double layer design is similar to the single layer one except the photolithography process. Double layer of SU-8 should be patterned on the nickel. The top and bottom SU-8 layers contain the patterns of circular plate and blades, respectively. The electroplating time should be doubled because of the thickness increment of the patterned SU-8 layers.

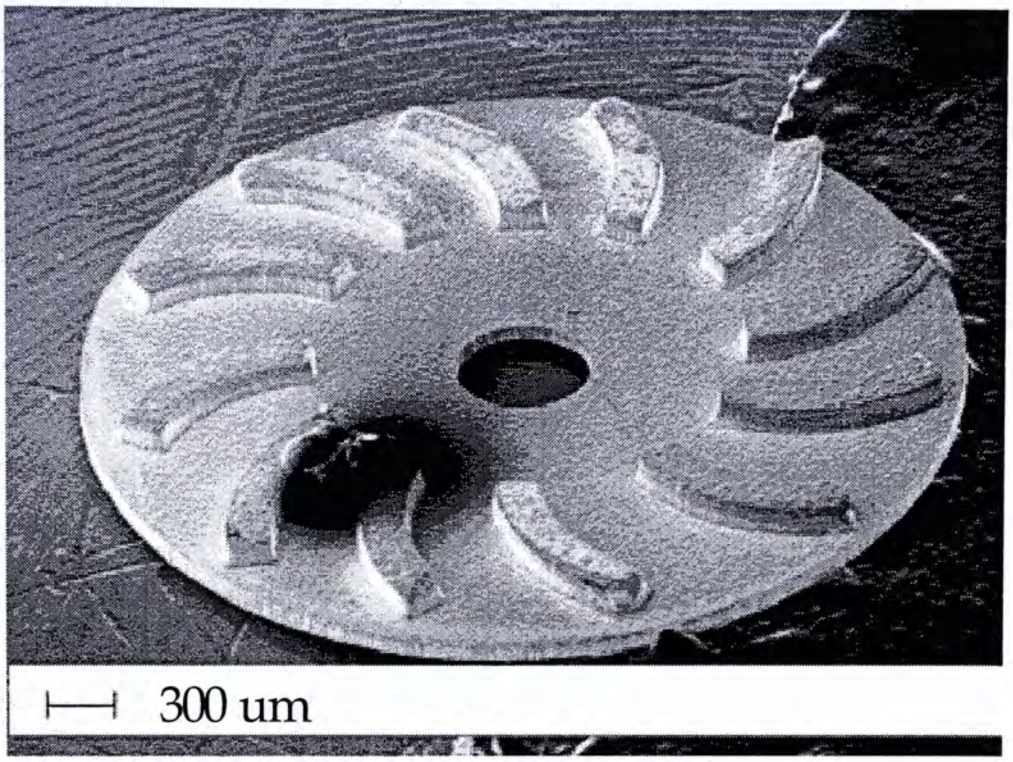

Figure 14. SEM image of the double layer structured nickel impeller .

3-2-2 SU-8 Impeller

A biocompatible impeller can be achieved by the SU-8 photolithography. The fabrication process of the SU-8 impeller is a sacrificial release of the patterned SU-8 layer as shown in Figure 15. Gold should be firstly sputtered on a PMMA substrate. Thickness of the copper layer could be increased by electroplating (this copper-deposited substrate can be simply replaced by a photoresist-purged printed-circuit board). Afterwards the pattern of impeller should be fabricated by the photolithography of the circular plate layer and, then, the blades layer. Both layers of structures should be around 100 μm thick. After removing the copper layer by the corresponding enchant, SU-8 impeller would be eventually sacrificial-released. Replacing the copper-deposited substrate with a polyester sheet is another feasible fabrication approach. Impellers could be torn off after patterning two layers of SU-8 structures.

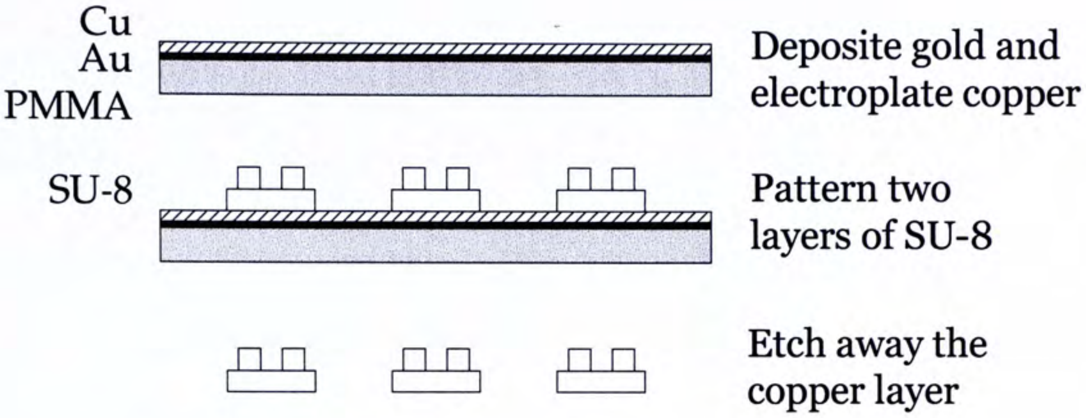

Figure 15. Fabrication process of SU-8 Impeller.

Multiple impellers can be manufactured by a single chain of fabrication process. The yield of impellers is determined by the substrate size and mask design. For example, we fabricated 100 identical impellers on the 55 mm × 55 mm polyester substrate as shown in Figure 16. The compacted impeller mask design can highly enhance the fabrication productivity.

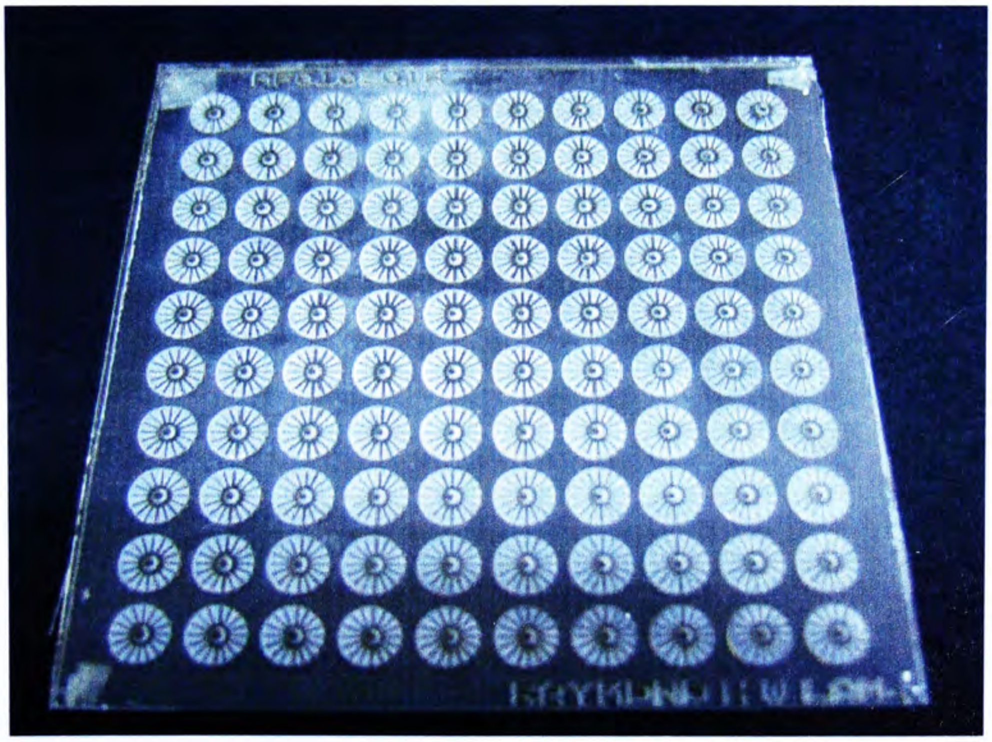

Figure 16. Photograph of an array of fabricated impellers.

3-2-3 Micropump Fabricated by Micro Molding Replication Technique

Micro molding replication technique is a low cost and flexible microfabrication method for the polymer-based microfluidic systems (the work on vortex micropump fabrication applied with micro molding replication technique was presented in [53]). It includes the mastering, replication and bonding processes. Closed microfluidic structures, e.g. channels and chambers, can be achieved by bonding the patterned substrate with a flat substrate.

The fabrication of the mastering process is illustrated in Figure 17 (a). High aspect ratio photolithography, electroforming and resist stripping are used to fabricate a micro mold, which functions as a replication master. The mold includes the pattern of the vortex micropump structure, which is shown in Figure 17 (b). A layer of 200 μm thick SU-8 negative photoresist is patterned on a nickel substrate by photolithography. Then, a 3000 Å thick sliver conductive layer should be sputtered on the substrate. The 300 μm thick nickel mold should then be fabricated on the silver layer by electroplating.

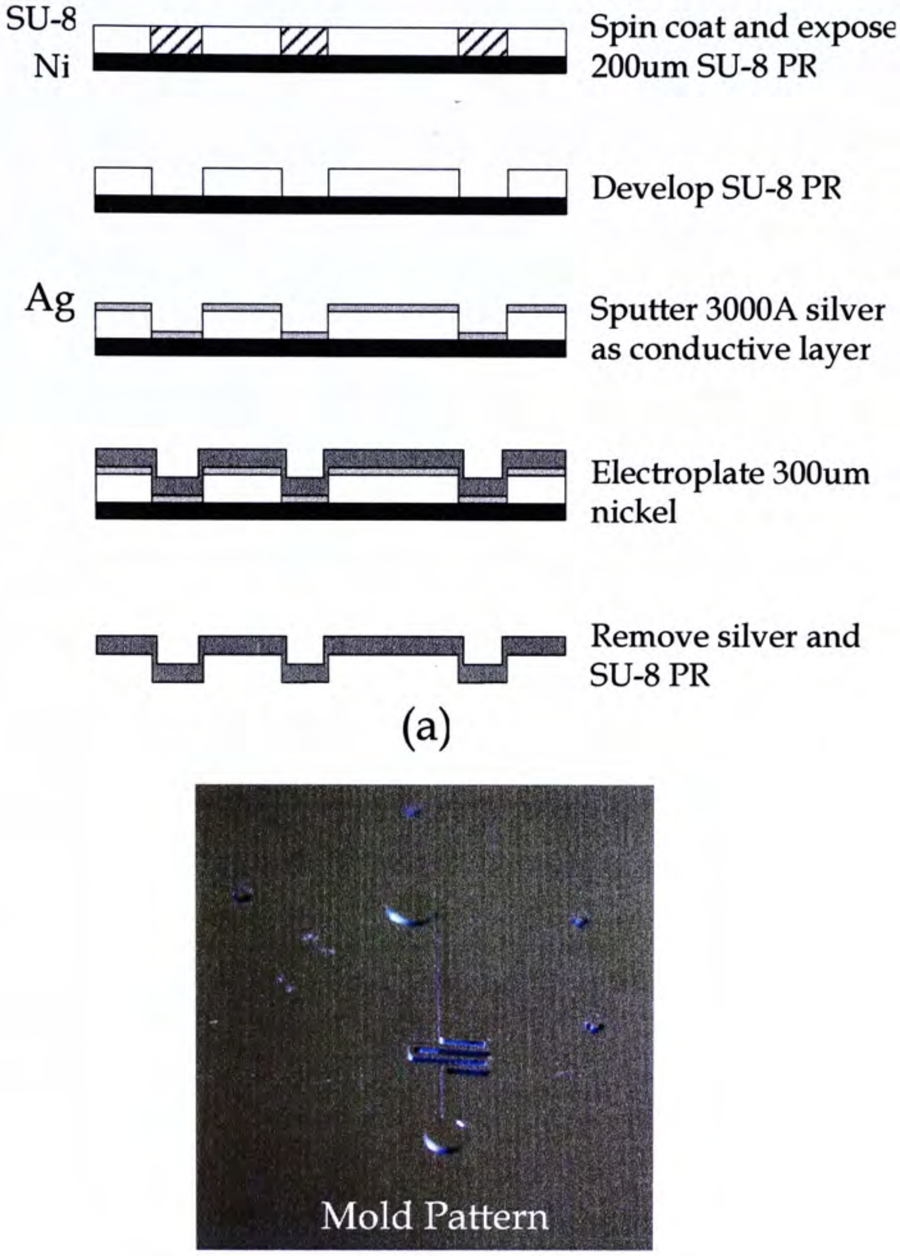

(a)

(b)

Figure 17. (a) Nickel micro mold fabrication process and (b) photograph of nickel micro mold pattern.

The micropump replication and assembly processes are shown in Figure 18. Microstructures on the replication master can be transferred to a polymer substrate by the hot embossing machine. The microfluidic channels and chambers can be replicated by the hot embossing technique. To produce the micropump, a PMMA substrate should be firstly heated to 120 °C, which is slightly above its glass transition temperature (T_g = 105 °C). Then a pressure of 7 MPa is applied by a hydraulic press to compress the mold towards the PMMA substrate. This causes the pattern of micro mold transformed to the PMMA substrate negatively. After the substrate and the mold cool down, the substrate should be released from the nickel mold. To increase the pump chamber volume, machining tools are used to deepen the chamber. An impeller and a DC motor should be assembled on the top and the bottom of the chamber, respectively. The inlet and outlet of micropump are produced by drilling holes through another flat PMMA substrate. Afterwards the flat substrate should be spun on with the UV-curing epoxy resin as the adhesive layer. Bonding the patterned PMMA with the flat PMMA forms closed channels between the two substrates eventually.

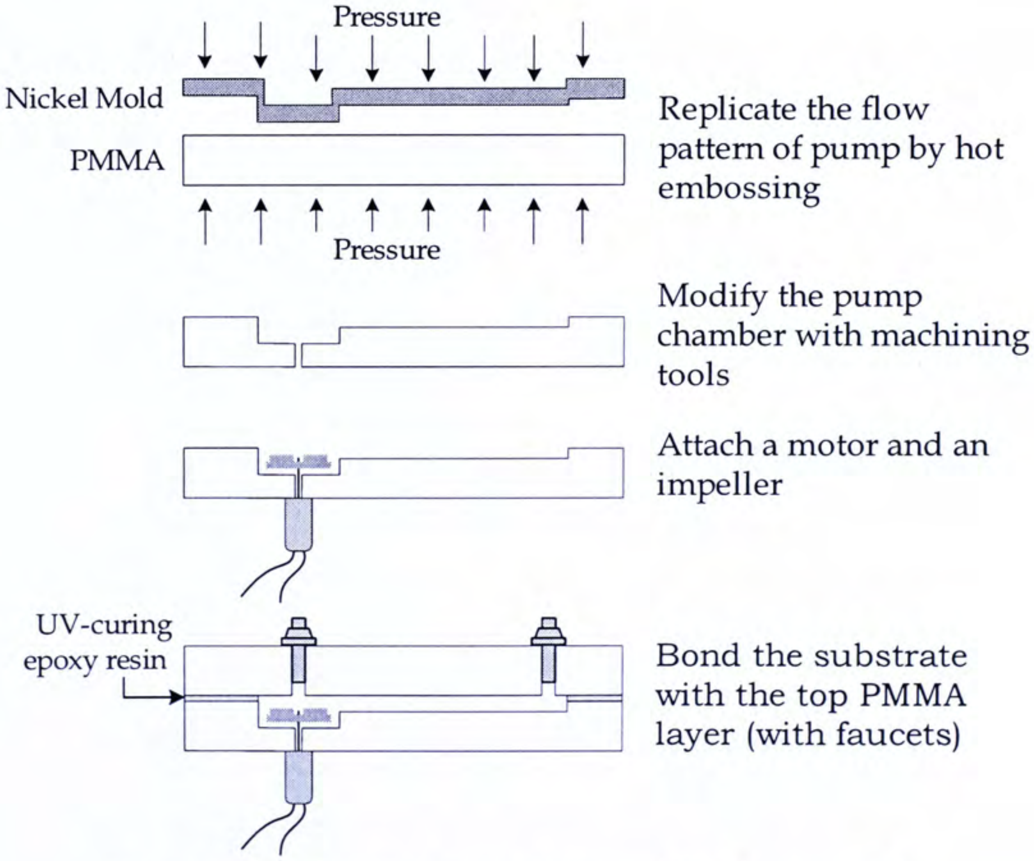

Figure 18. Replication and Assembly Processes of the vortex micropump.

3-2-4 Inverted-chamber Vortex Micropump

In the inverted-chamber design, a vortex micropump requires two layers of flow channels. The fabrication process is illustrated in Figure 19. The two layers of 80 μm deep channel patterns can be fabricated by the photolithography of SU-8. Afterwards machining processes should be performed to manufacture the inlet, the outlet, the 2 mm deep pump chamber and the 1 mm diameter connecting channels between flow layers. The microchannels can be enclosed by attaching a polyester film on each side of the substrate using UV-curing epoxy resin. Faucets should then be inserted to provide the inlet and outlet connections. An impeller can be fixed inside the microchamber by attaching it to a DC motor. Moreover, the motor should be lifted up by a 2 mm thick PMMA with a 2 mm diameter hole at the center. When fluid is filled inside the chamber, air will be trapped at the hole of the 2 mm thick PMMA to prevent the fluid flows inside the motor.

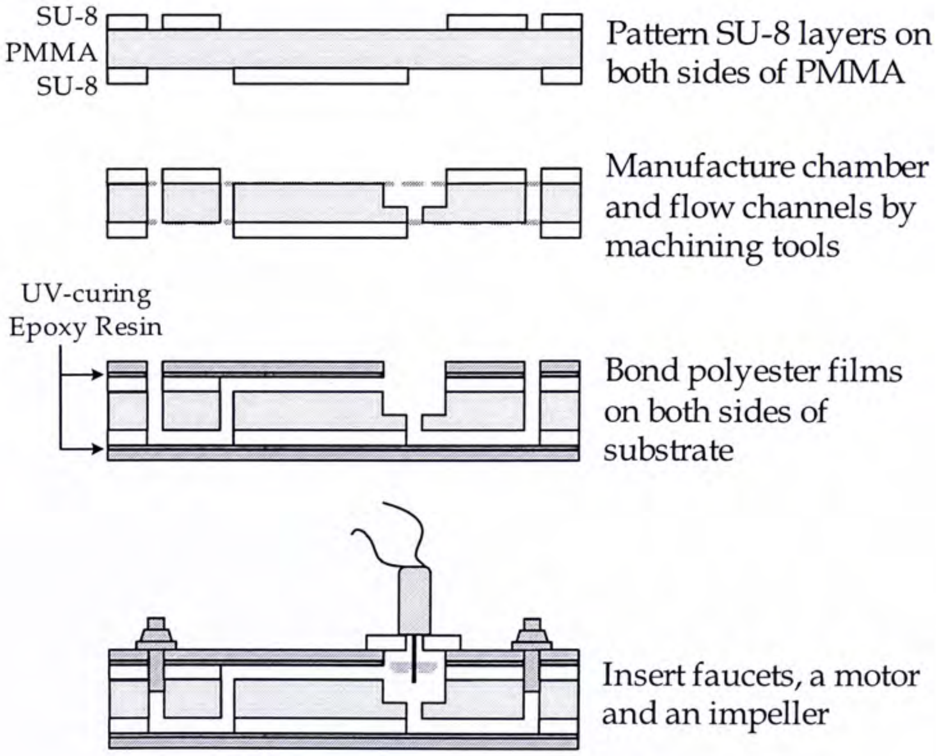

Figure 19. Fabrication process of the vortex micropump applied with inverted-chamber design.

3-3 ELEMENTARY CENTRIFUGAL PUMP THEORY

3-3-1 Pumping Pressure and Discharge

A vortex micropump consists of a flow chamber, a rotary impeller and the inlet and outlet channels. Its structure and operation principle are similar to the classical centrifugal pump as mentioned previously. In this section, a simplified model of the vortex micropump will be introduced, with extended description on the design considerations. Since the control volume of fluid is still far larger than the limiting volume, 10^{-9} mm^3, in microchannels, fluid can be viewed as a continuum in the microfluidic pump and the classical centrifugal pump model is still adoptable. Not only are the fundamental characteristics of the pump described, but also the design considerations are discussed in the later section. Our group has recently developed a more applicable analytical model of the vortex micropump (Details of the analytical model were described in [55]). Nevertheless, the pumping performance will be analyzed mainly with the basic model in the following sections. In the centrifugal pump, it could be assumed that fluids are pumped from the center, or the eye, to the perimeter of the rotary impeller as illustrated in Figure 20. The impeller rotation, with rotational speed ω, induces the fluid flow with velocities v_1 and v_2 at the inner and outer blade terminals, respectively. The pumping discharge is related to the effective flow velocities v_{n1} and v_{n2}, which are normal to the inner and outer tangent vectors of impellers u_1 and u_2. Therefore, the effective flow velocities would affect the pump rate and pressure of flow chamber and, hence, the whole pumping mechanism.

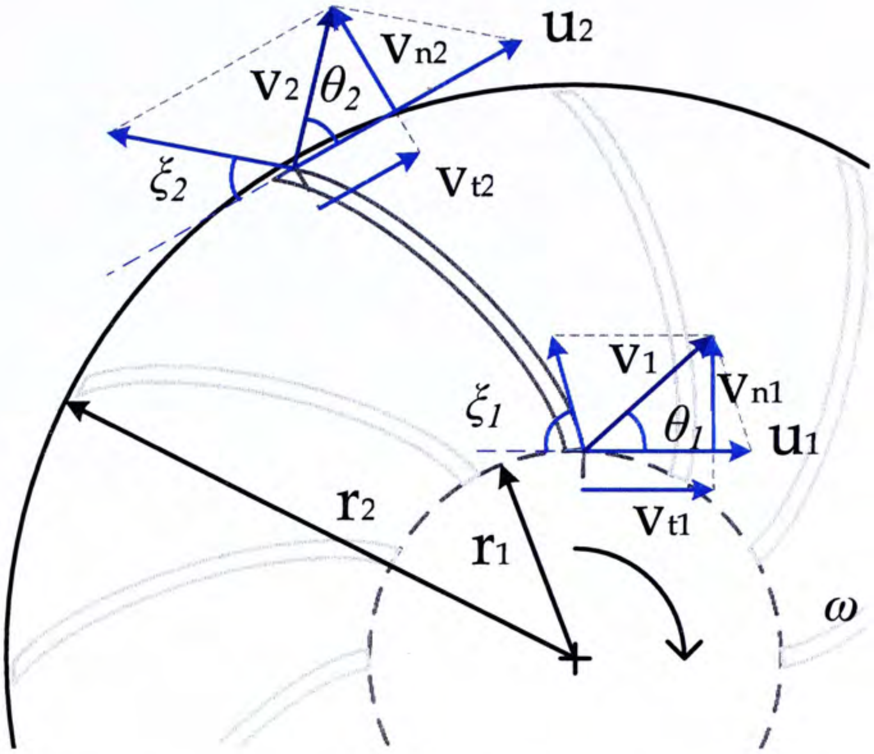

Figure 20. Top view diagram of fluid velocities at blade terminals for a micropump impeller.

The vortex micropump basically activates fluid flow by enhancing the Bernoulli head of flow between the input and output channels of microchamber. Since the identical structure of the input and output channels, the difference between the channel flow rates is negligible. The 3 mm elevation of channel height, or the thickness of PMMA substrate, is also insignificant, comparing to the pressure increment. Assuming steady incompressible flow, the change of Bernoulli head, or pumping pressure, can be approximated as

$$H = \left(\frac{p_o}{\rho g} + \frac{v_2^2}{2g} + z_o \right) - \left(\frac{p_i}{\rho g} + \frac{v_1^2}{2g} + z_i \right) \approx \frac{p_o - p_i}{\rho g}, \tag{3.1}$$

or

$$p = p_o - p_i = \rho g H, \tag{3.2}$$

where ρ is fluid density, g is the constant of gravity, p_i, p_o, v_1, v_2, z_i and z_o are the input and output pressures, the input and output flow velocities, and the heights of input and output channels, respectively.

The output flow rate of the vortex micropump is equal to the rate of input fluid mass based on the conservation of mass transfer. The fluid flow rate from the impeller eye can be approximated by the curved surface area of the virtual eye cylinder times the normal velocity, v_{n1} and v_{n2}, of inlet fluid on the surface. The discharge of the micropump then becomes

$$Q = 2\pi r_1 h v_{n1} = 2\pi r_2 h v_{n2} \tag{3.3}$$

where h is the thickness of impeller blades.

Both discharge and pump pressure can be regulated by the rotation speed of impeller. It is easy to observe that v_{n1} and v_{n2} are related to ω in equation (3.3). The Bernoulli head can also be varied with ω and the relation will be explained in the next section.

3-3-2 Fluid Horsepower

The fluid horsepower required for the fluid delivery at certain discharge and pump pressure can be estimated by the rotational speed and shaft torque of the motor. The ideal torque of the impeller is expressed by *Euler's turbine formula*. Choosing the control volume as the ring region between radii r_1 and r_2, the total moment about the center of rotation can be simplified as

$$\sum \vec{M} = (\vec{r}_2 \times \vec{v}_2)\dot{m}_o - (\vec{r}_1 \times \vec{v}_1)\dot{m}_i \tag{3.4}$$

where $\dot{m}_i$ and $\dot{m}_o$ are the rates of change of input and output fluid masses, respectively.

Since the steady flow is assumed, the rates of change of fluid masses are both equal to the product of density and discharge. Hence the torque, in clockwise direction, becomes

$$T = \sum M = \rho Q(r_2 v_{t2} - r_1 v_{t1}) = \frac{P}{\omega}. \tag{3.5}$$

The power delivered to the fluid is defined as the product of specific weight, the net change of Bernoulli head and the fluid discharge, that is,

$$P = \rho g H Q \tag{3.6}$$

where Q is the fluid discharge.

The above equation indicates that the Bernoulli head is related to the discharge of vortex micropump. The relation also induces the controllability of pumping pressure by the variation of impeller rotation. A vortex micropump with desired working discharge and pumping pressure could be designed and estimated by regulating the related parameters discussed above.

Furthermore, the horsepower of a vortex micropump can also be related to the radical velocity. Thereby equation (3.5) can be rewritten as

$$P = \rho Q(u_2 v_{n2} \cot\theta_2 - u_1 v_{n1} \cot\theta_1) \tag{3.7}$$

and $$v_{n1} = \frac{Q}{2\pi r_1 h},\quad v_{n2} = \frac{Q}{2\pi r_2 h} \quad \text{(recalled from equation (3.3)).} \tag{3.8}$$

The micropump can be designed with $\theta_1 = 90°$, such that $v_{n1} = v_1$, for the optimal pumping efficiency [49]. The direction of fluid flow could eliminate the tangential velocity. The discharge with optimal efficiency is called the design flow rate. It is often used as the reference value of the flow rate performance.

3-3-3 Effect of Blade Angle

Recall equation (3.5), the theoretical fluid horsepower can be expressed as

$$P = \rho Q(u_1 v_{t1} + u_2 v_{t2}). \tag{3.9}$$

Substituting $v_{t1} = u_1 - v_{n1}\cot\xi_1$ and $v_{t2} = u_2 - v_{n2}\cot\xi_2$, the theoretical Bernoulli head from equation (3.1) should be

$$H = \frac{u_1^2 + u_2^2}{g} - \frac{Q}{2\pi hg}\left(\frac{u_1\cot\xi_1}{r_1} + \frac{u_2\cot\xi_2}{r_2}\right). \tag{3.10}$$

Since $u_1 = r_1\omega$ and $u_2 = r_2\omega$, the head becomes

$$H = \frac{\omega^2}{g}\left[(r_1^2 + r_2^2) - \frac{Q}{2\pi h\omega}(\cot\xi_1 + \cot\xi_2)\right], \tag{3.11}$$

or in the dimensionless form,

$$H^* = \frac{Hg}{(r_1^2 + r_2^2)\omega^2} = 1 - \frac{Q}{2\pi h\omega(r_1^2 + r_2^2)}(\cot\xi_1 + \cot\xi_2). \tag{3.12}$$

The Bernoulli head of vortex micropump varies with the discharge as described in equation (3.11) and (3.12). Substituting the related parameters of the typical vortex micropump (r_1 = 500 μm, r_2 = 2.25 mm and h = 100 μm) and assuming the case of optimal pumping (θ_1 = 90°) such that $v_{n1} \approx r_1\omega\tan\beta_1$, the heads and discharges can be calculated with different blade angles. A plot of the head against the pumping discharge in the dimensionless form is shown in Figure 21. For the radical blades design ($\xi 1 = \xi 2 = 90°$), the head is constant at the shifting value $\omega^2(r_1^2 + r_2^2)/g$. The slope is negative for the backward-curved blades ($\cot\xi 1 + \cot\xi 2 > 0$), and positive for the forward-curved blades. In the forward-curved design, the micropump can enhance the pumping pressure at a low fluid discharge. However, it will cause the surge problem of the pumping for a high flow rate. The rapid increment of pumping pressure induces turbulences inside the pump chamber and so the performance of pumping will become unsteady.

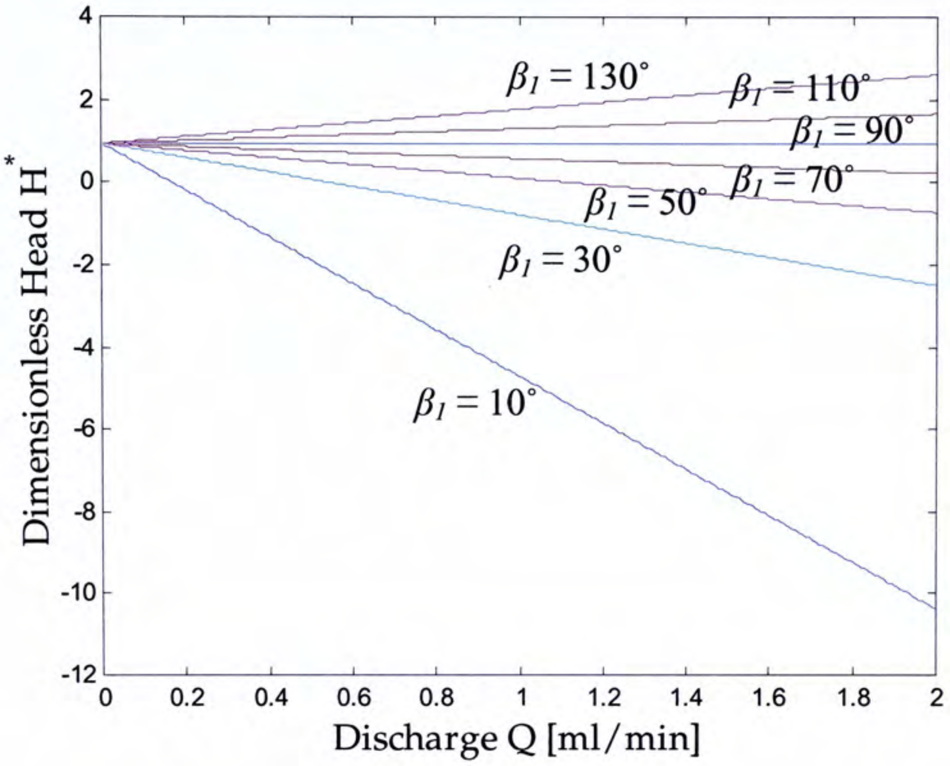

Figure 21. The analytical dimensionless Bernoulli head values corresponding to different design flow rates for different blade angles.

3-4 PUMPING SPECIFICATION

Pump pressure and discharge are the two essential considerations for the micropump applications. When a vortex micropump operates with a microfluidic chip containing complicated microchannel structure, the back pressure of the channel array would become significant. The micropump should generate sufficient pumping pressure to retain the fluid flow. Furthermore, an appropriate fluid flow rate is requisite in some microfluidic devices. For instance, some bio-chemical detection chips function only within a discharge range [48]. An optimal fluid discharge could also shorten the delivery time. For an integrated microfluidic system, delivery time is one of the major considerations since the delay in the microfluidic components would accumulate and affect the performance of the entire system. The characteristics of the fabricated vortex micropumps will be analyzed by experiments in this section.

The calibration result on the relationship between the rotational speed of impeller and its applied voltage is showed in Figure 22. In the experimental setup, the half portion of impeller was shaded with black paint. An infrared light beam was illuminated from the topside of micropump while an infrared light receiver was mounted at the bottom of pump. When the impeller was driven with a variable voltage to pump water, the paint of the impeller blocked the beam and hence the infrared receiver would obtain pulse signals. The rotational speed of impeller could be eventually obtained by counting the signal frequency. The calibration result can be viewed as the reference characteristics of pumping aqueous solutions. In some applications, the micropump could be used to pump colored fluid. Such operation would make the real-time measurement of rotational speed become difficult. In the later sections, the experiments related to vortex micropump will only show the input voltages, because of the measurement restriction. Nevertheless, the rotational speed can be estimated by the instantaneous input voltage based on the reference characteristics.

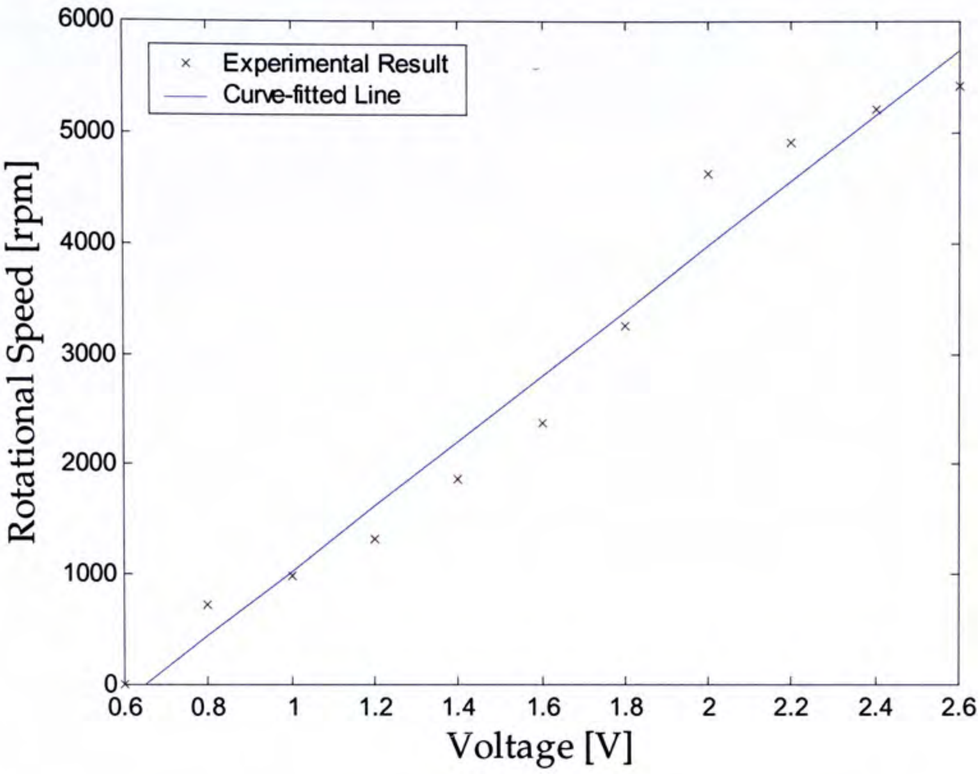

Figure 22. Calibration result of the impeller rotational speed corresponding to different input voltages.

Another experiment of the micropump was performed to investigate the relationship between the impeller rotational speed and the flow rate. The inlet and outlet of pump were connected to the reservoirs filled with distilled water. Before experiment, the liquid in the reservoirs were regulated to same liquid level to eliminate the initial flow due to gravitation. Water was pumped to the outlet with different driving voltage throughout the experiment. The pump discharge could be calculated by measuring the weight increment at the outlet reservoir with the relation $Q = \Delta m / (\rho_w \times \Delta t)$, where Δm is the change of outlet mass, ρ_w is the density of water and Δt is the pumping duration. Because of the insignificant volumetric delivery, comparing to the water masses in reservoirs, the fluid flow actuated by the fluid level change was negligible. Experiments were performed for the single-layer impeller design, the double-layer design with original and inverted chamber configurations. Based on the micropump characteristic in Figure 22, the analytical and measured flow rates with different input voltages were calculated as illustrated in Figure 23. The micropump impellers were designed with the same dimension (r_1 = 500 μm, r_2 = 2.25 mm and h = 100 μm). The flow rate increases linearly with the applied voltage for both designs. However, different levels of discharge loss could be observed in the micropumps. The loss is caused by 1) the friction loss by laminar and turbulent fluid flows and 2) the geometry and surface roughness of impeller and pump chamber [49]. It indicates the pumping efficiency of the double-layer impeller pump (~80.22 %) is higher than that of the single-layer design (~63.73 %). This is because the circular plate of the double-layer impeller can constrain the flow direction and enhance the normal fluid velocity. The inverted chamber configuration slightly reduces the pumping efficiency by ~7.69 %. It also indicates the flow rate of the vortex micropump can achieve 0.758 ml/min, 1.02 ml/min and 0.850 ml/min at ~ 2.5 V applied voltage for the single-layer design, the double-layer impeller designs with original and inverted chamber configurations, respectively.

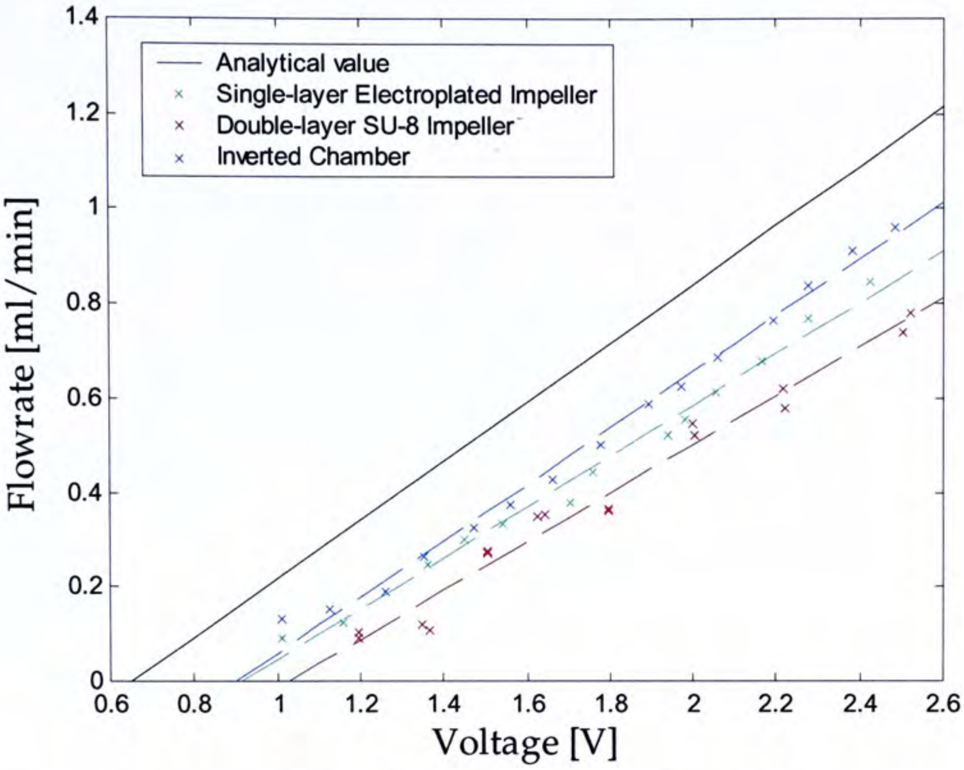

Figure 23. Relationship between the flow rate of different micropumps designs and the applied voltage.

The pump pressure analysis was based on the elevation of outlet fluid level generated by a vortex micropump. The micropump outlet was connected to a vertical polyurethane tube in the experimental setup. Different constant voltages were applied to pump distilled water throughout the experiment. The fluid level of pump outlet raised and stopped at a maximum height. Similar to the flow rate experiment, the change of inlet fluid level was also neglected. The weight of elevated fluid would balance the pump pressure and therefore the pumping pressure could be estimated by $P = \rho_w \times g \times h_t$, where ρ_w is the density of water and h_t is the elevation of fluid level. Different output pressure values were measured on the original and inverted-chamber micropumps, actuated with the double-layer impellers as shown in Figure 24. Pump pressure increased with the applied voltage for both micropumps. It could reach 1.831 kPa and 1.556 kPa, at ~2.5 V input voltage, for original and inverted-chamber designs, respectively.

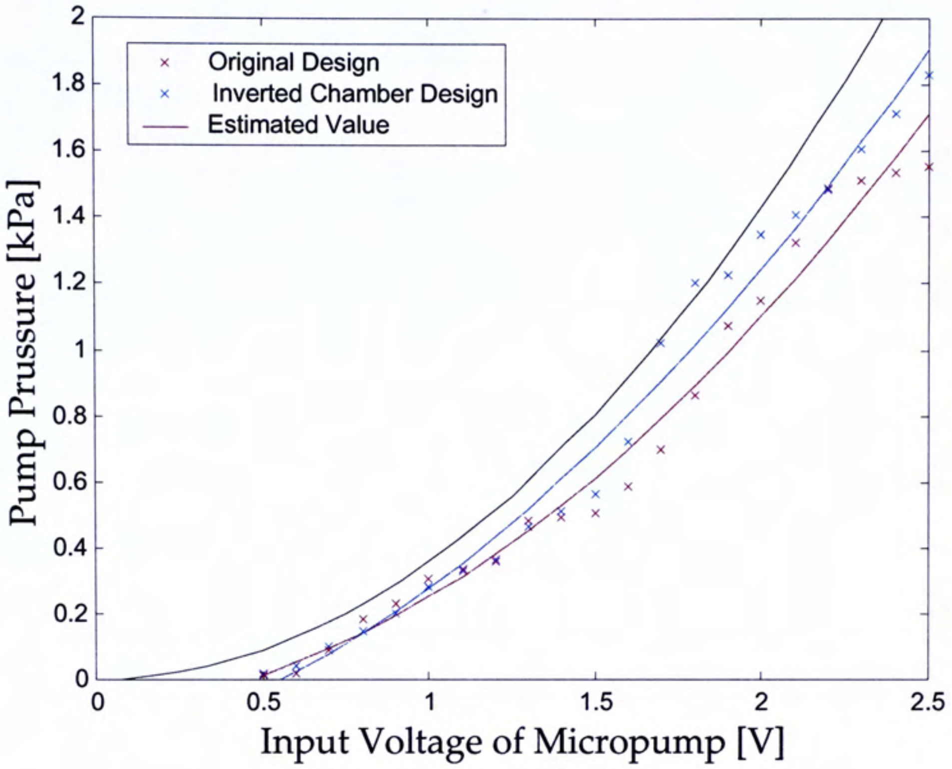

Figure 24. The pumping pressures of vortex micropump actuated with double layer SU-8 impeller corresponding to different input voltages.

CHAPTER

FOUR

MIXING BASED ON MECHANICAL VIBRATION

4-1 MICROMIXER DESIGN

4-1-1 Oscillating Diaphragm Actuated Microfluidic Mixing

A thorough micromixing of two of more fluids is based on the molecules diffusion. The effective mixing requires low interfacial tensions along the interface fluids, low fluid viscosities and large concentration gradient between fluids [57]. However, the requirements are arduous to be achieved in the microfluidic devices. The extensively high velocity of fluid in microchannel with $<10^{-7}$ m^2 cross-section area is essential in microchannels for the significant discharge of 1 – 10 ml/min. This will cause a considerable interfacial tension of fluids and greatly reduce the mixing rate.

The mixing of microfluidic flow can be enhanced by multiplying the interfacial area or generating the vorticity of fluid. Our group has practically demonstrated the swap pumping approach that could effectively increase the interfacial area between the sample fluids (water and red dye) [54]. The interfacial area was further increased by passing fluids into a microchamber with larger cross-section area, $\sim10^{-5}$ mm. The fluids would be mixed after certain distance of flow. Furthermore, the turbulence induction is another feasible approach for mixing enhancement. The microfluidic active mixing originated by the PZT driven mechanical vibration was presented in [58]. The silicon-based micromixer contained a 6 mm × 6 mm × 600 μm chamber. The laminar flows of water and uranine solution were mixed under the PZT-diaphragm oscillation with ultrasonic-range frequency (~60 kHz). The diaphragm vibration could generate vorticity, acting as convection current, and agitate the fluids inside the mixing chamber. In this project, biocompatible microfluidic mixers based on the PZT diaphragm oscillation were designed, fabricated and experimentally investigated. The details will be described in the following sections.

4-1-2 Flat-surface Diaphragm Active Micromixer

The polymer based flat-surface diaphragm (FSD) active micromixer consists of a PMMA substrate, a polyester layer, a metallic diaphragm and a piezoelectric lead zirconate titanate (PZT) ceramic. The mixing operation is based on the mechanical vibration generated by the PZT ceramic as mentioned previously. In the design of the FSD active micromixer, the mixing chamber, which contains an oscillating diaphragm, acts as an active microfluidic mixing component. When voltage is applied with the same direction of the poling field, the PZT ceramic will contract laterally, and vice versa. Moreover, when a square wave signal is applied to the PZT film, the residual stress will cause the ceramic to contract and to expand continuously and therefore the metallic diaphragm will vibrate horizontally. The material of diaphragm should be manufactured with metal, or other materials that are electrically conductive and provide sufficient Young's modulus for the horizontal vibration. However, some metal may react with particular bio-fluids or chemical solutions. The biocompatibility can be achieved by selecting appropriate substrate material, i.e. PMMA, and coating the metallic diaphragm with polymer. The polymer layer should be thin and deformable to minimize its interference in the diaphragm vibration (parylene C and poly-dimethylsiloxane (PDMS) are feasible choices).

The mixromixer was designed to combine the fluid flow from the two device inlets, to amalgamate the fluids in the microchamber, and to export the mixed fluid to the outlet. The substrate was fabricated with an 80 μm deep cavernous pattern containing a mixing chamber with 11 mm diameter, two 300 μm wide inlet channels and a 600 μm wide outlet channel. The profile of the patterned PMMA substrate is illustrated in Figure 25. The flow of inlet fluids are combined at the confluence region at the "Y"-shape channel (the 100X microscopic image in Figure 25). The microchamber, which has a larger cross-section area around 8.8×10^{-7} m^2, reduces the fluid velocity and, hence, extends the duration of fluid staying inside the chamber. This can also provide a more applicable condition for mixing as described in section 4-1-1. A cross-section view of the mixing chamber is shown in Figure 26. A circular brass layer, with 11 mm diameter and 100 μm thickness, is bonded with the pattern side of the PMMA substrate. A piezoelectric PZT ceramic, with 9 mm diameter and 20 μm thickness, adheres to the brass layer. The PZT ceramic can be driven by a signal generator and a power amplifier to provide the mechanical oscillation. Furthermore, the mixed fluids will eventually pass to the outlet after full mixing occurs.

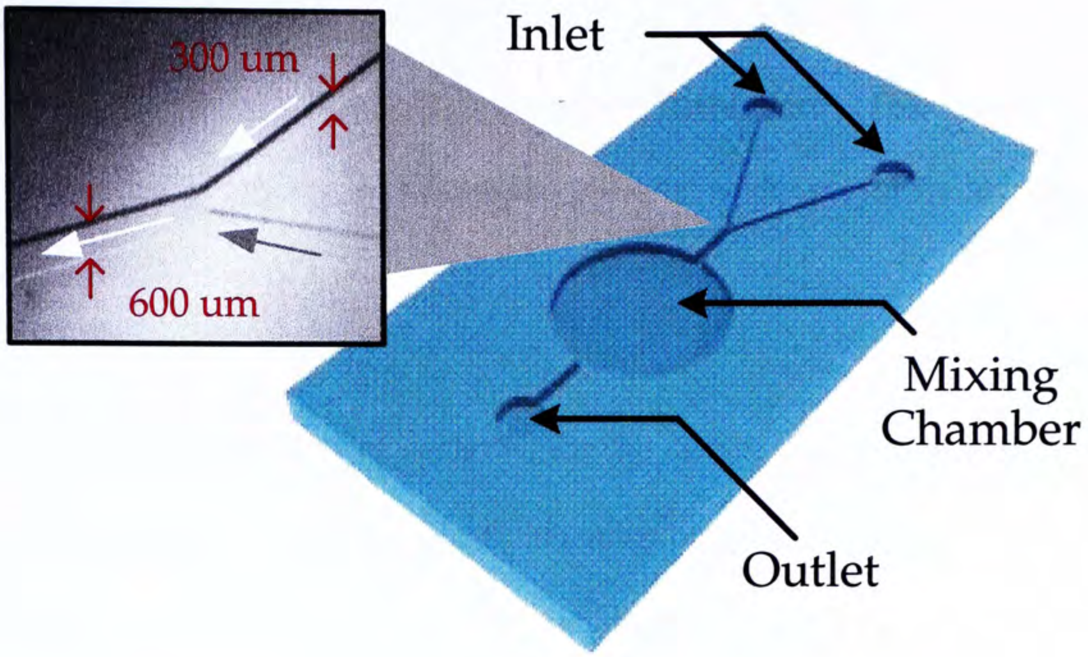

Figure 25. Pattern on the PMMA substrate designed for the vibration-driven active micromixers.

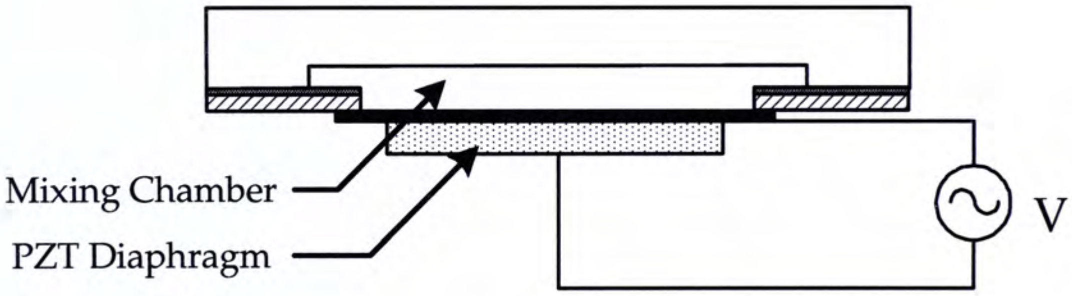

Figure 26. Cross section view of the fluid chamber.

4-1-3 Mixing Enhancement by Pillared Chamber Profile

The mixing time of the FSD micromixer (~1 – 2 min) would be a significant factor in some microfluidic applications. Microfluidic mixing can be viewed as a result of the turbulent flow of multiple fluids inside a channel or chamber. In the previous micromixer design, mixing is enhanced by the external PZT diaphragm-driven vibration, which is one of the factors for turbulent flow [57]. The turbulent flow can further enhance by the chamber geometry design. Some previous researches showed that the passive microfluidic mixing could be achieved by particular channel structures [31]. Thereby the pillared-surface diaphragm (PSD), which had a modified chamber geometry, was designed to improve the performance of vibration based mixing.

The PSD active micromixer was designed for the mixing of chemicals since the flow of the bio-molecules or cells in bio-fluids may be blocked by the pillars. In the modified micromixer, the device structure is identical to the FSD micromixer except the chamber profile as shown in Figure 27. An array of Pillars should be fabricated on the topside of the chamber wall (The pillar design and dimension will be described in section 4-2-2). Because the chamber should provide a vertical gap for the fluid flow and diaphragm vibration, the chamber wall must be thicker than the pillars. The pillared surface can effectively reduce the laminar flow at the upper portion of the microchamber, so a smaller amplitude of the diaphragm vibration is required for the thorough mixing.

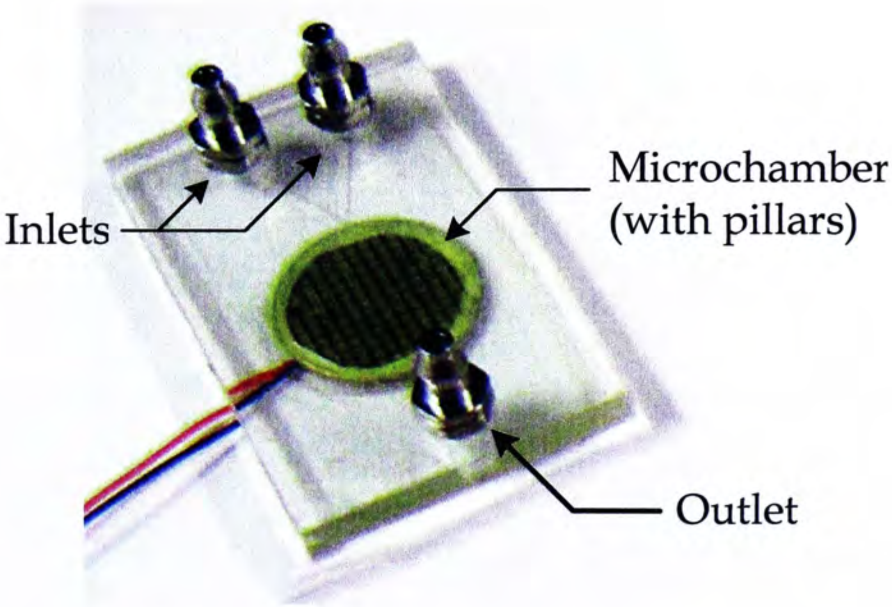

Figure 27. Photograph of a fabricated PSD active micromixer.

4-2 FABRICATION PROCESS

4-2-1 Flat-surface Diaphragm Active Micromixer

The fabrication process of the FSD active micromixer is illustrated in Figure 28. PMMA substrate is used because of its biocompatibility. The walls of channels and chamber are patterned by photolithography. MicroChem™ SU-8 2075 photoresist was spun on the substrate at 3000 rpm rotational speed. After soft bake at 65 °C for 5 min and 80 °C for 40 min, the SU-8 layer should be exposed under the mask with the channels and chamber pattern for 60 s. Post bake should be performed at 50 °C for 30 min. The baked SU-8 should then be immersed in MicroChem's SU-8 Developer for 60 min at room temperature. The channels and chamber profile could be obtained after brief rinse with isopropyl alcohol (IPA) and DI water. The inlets and outlet can be made by drilling holes with diameter 2.8 mm at the pattern terminals to allow the insertion of faucets. Then a polyester film, with a 10 mm diameter hole, should be bonded with the substrate using a layer of UV-curing epoxy resin, spun on at 4,000 rpm for 40 s. After UV-exposure, the closed channels can be built between the substrate and the film. The biocompatible diaphragm can also be fabricated by spinning a 40 μm layer of PDMS, with 10:1 ratio, on an 11 mm diameter brass diaphragm. The PDMS layer should then be baked at 90 °C for 90 min. The biocompatible diaphragm can also be achieved by depositing a layer of 0.1 μm parylene C instead of PDMS. Then the diaphragm can be bonded around the hole of polyester layer. Since a PZT ceramic layer is adhered under the diaphragm, the region below the mixing chamber could provide the mechanical oscillation of fluid. The upper and lower sides of the PZT ceramic are connected with electrical wires to receive the driving voltage.

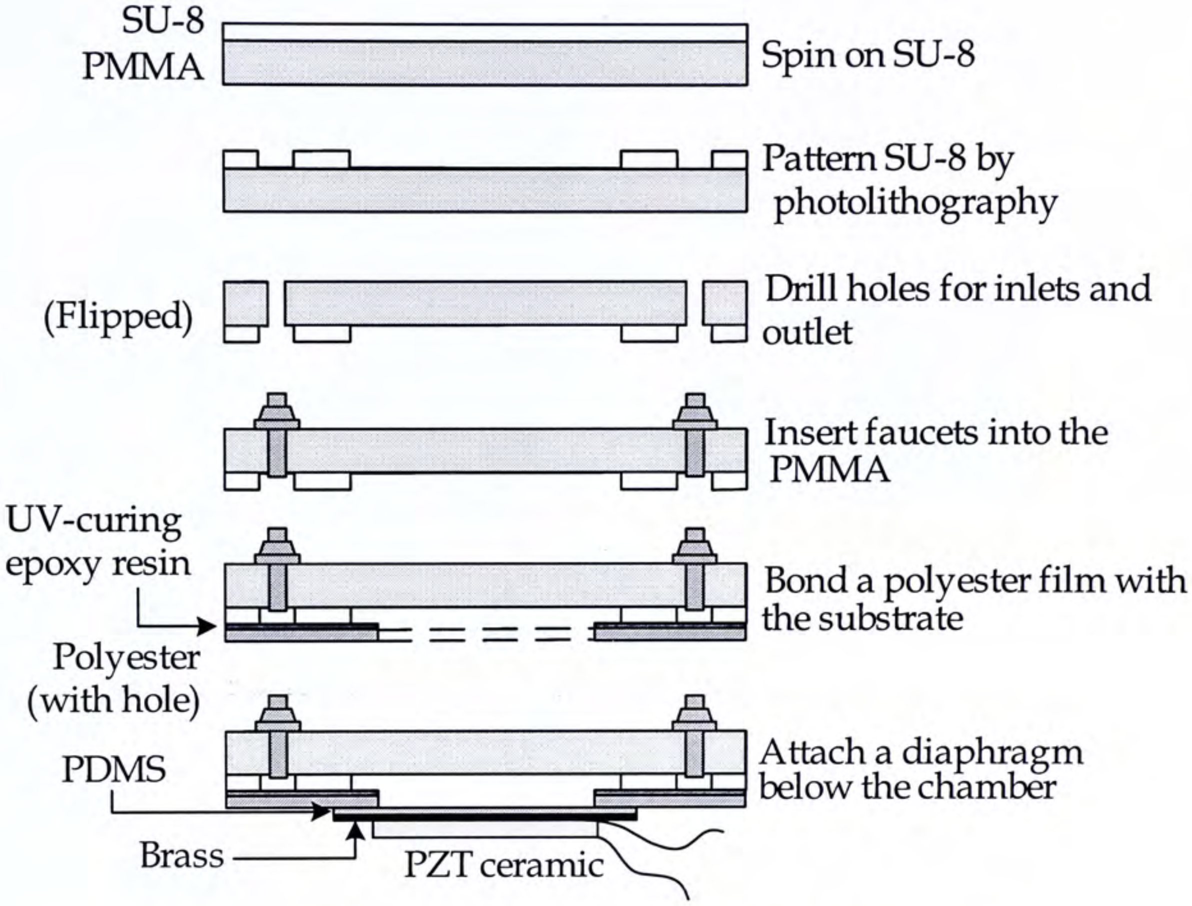

Figure 28. Fabrication process of the FSD active micromixer.

A photograph of the fabricated micromixer is shown in Figure 29. Red ink was inserted inside the channel to illustrate the pattern of fluid flow. After the sample was cut by a diamond saw, the cross-section view of the 600μm wide microchannel was captured by the microscope with 250X magnification. Another 100X microscope image was captured at the merging region of the fluid. It indicates the UV-curing epoxy resin can provide a satisfying bonding profile (A detailed bonding experiment of UV-curing epoxy resin will be discussed in Appendix A).

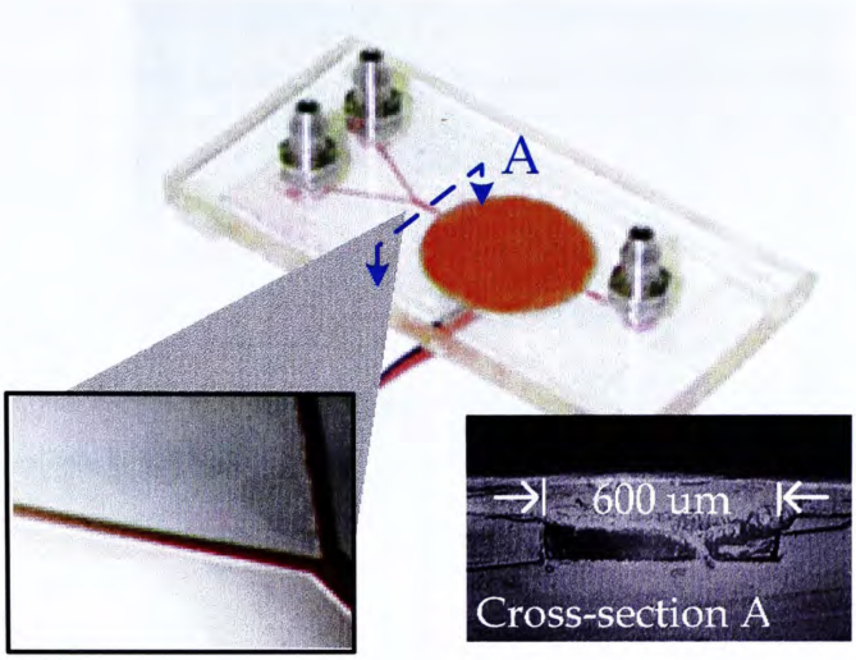

Figure 29. Photograph of the micromixer and microscope images of the channel features.

4-2-2 Pillared-surface Diaphragm Active Micromixer

A PSD active micromixer was successfully developed and fabricated to further enhance the mixing performance. The fabrication of the PSD active micromixer (Figure 30) was the similar to the FSD one except for the photolithography process. The PSD active micromixer used double layer of SU-8 to create a more complicated geometry. In the fabrication process, the first 80 μm thick SU-8 layer is patterned with the pillars, the walls of channels and chambers. The height of the chamber and channel walls should then be doubled by the second SU-8 layer. Thereby pillars can be created on the topside of the mixing chamber after flipping the substrate. The height of the chamber wall is twice that of the pillars, so the diaphragm can vibrate freely under the chamber. The inlets and outlet are made by drilling holes and inserting faucets. Afterwards the microchannels should be closed by bonding a polyester film, which contains a 10 mm diameter hole at the chamber region, below the SU-8 layer using UV-curing epoxy resin. The mixing chamber can be accomplished by attaching a brass-PZT diaphragm, which is pre-coated with PDMS, below the hole in polyester film.

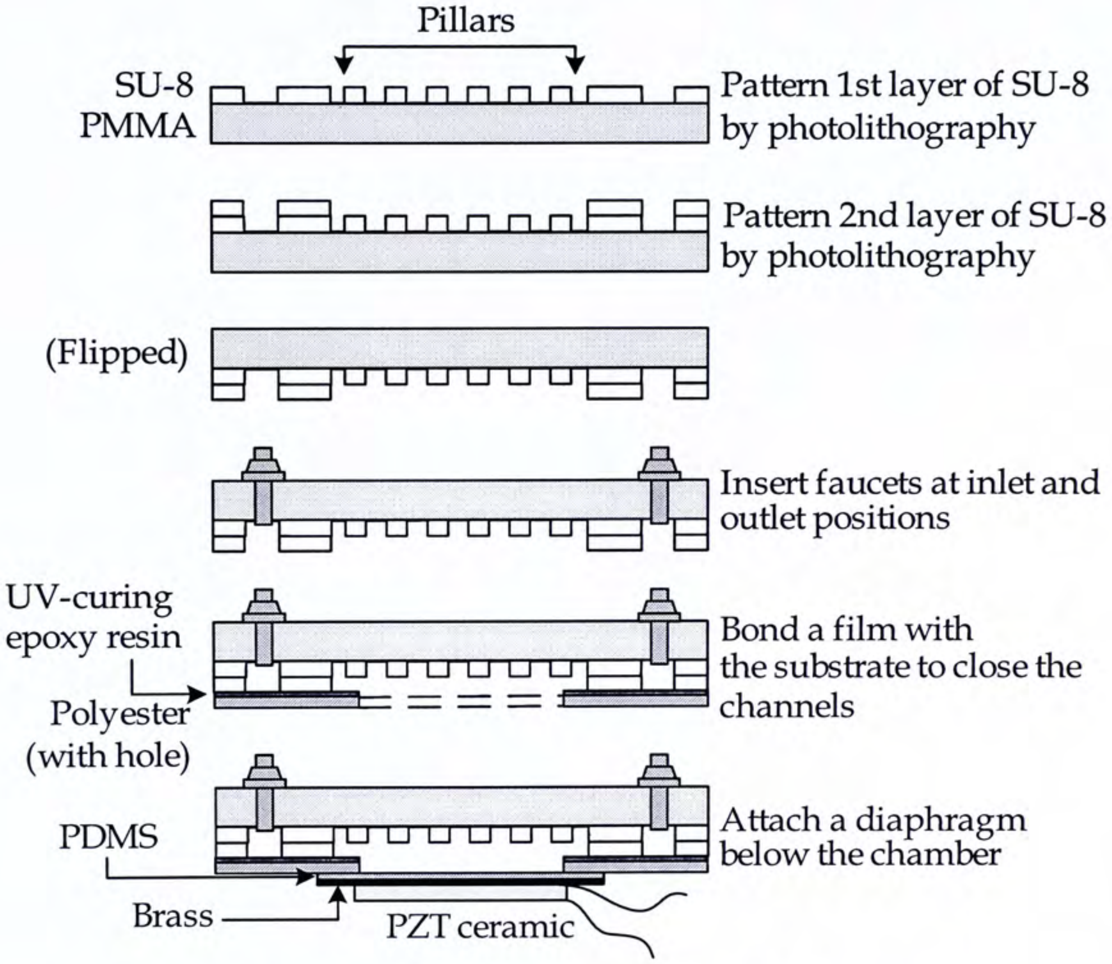

Figure 30. Fabrication process of the PSD active micromixer.

The chamber profile of a fabricated PSD active micromixer is illustrated in Figure 31. Pillars with dimensions 500 μm × 500 μm × 80 μm was evenly distributed inside the chamber (Figure 31 (a) and (b)). The walls of the chamber and microchannels were 160 μm in height (Figure 31 (c)) and so the distance between pillars and the diaphragm was around 80 μm. Fluid could flow fluently in the chamber since the amplitude of the diaphragm oscillation was around 2 μm. A thorough comparison of the experimental mixing time between the FSD and PSD active micromixers will be presented in section 4-3.

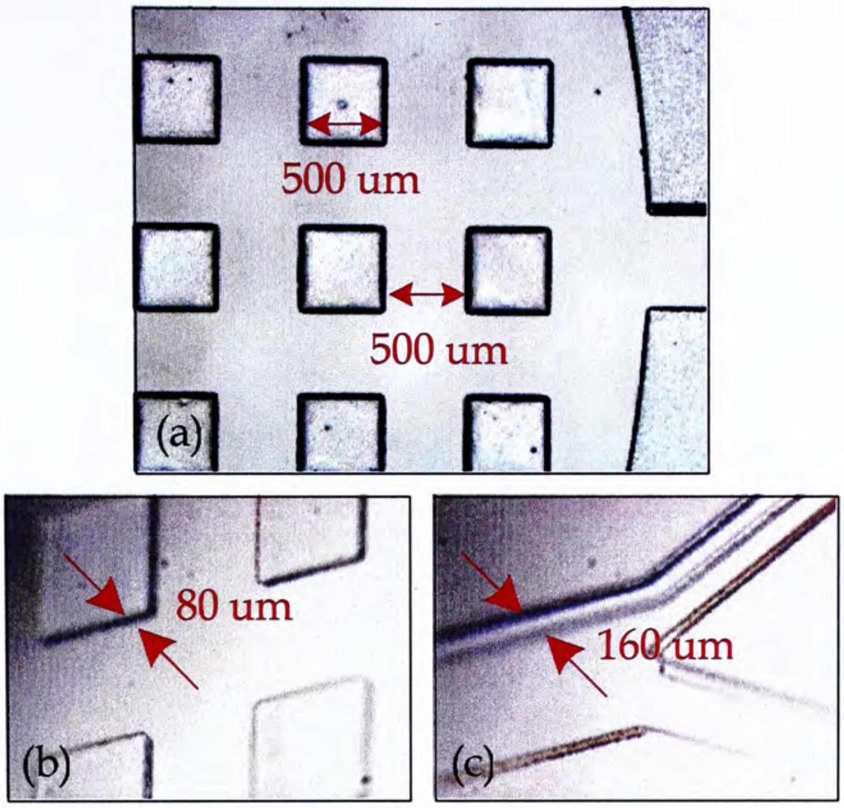

Figure 31. (a) Top view of mixing chamber and (b) isometric views of pillars and (c) microchannels.

4-3 EXPERIMENTAL ANALYSIS OF MIXING PERFORMANCE

An experiment was performed to analyze the mixing performance of the FSD and PSD active micromixers as shown in Figure 32 (a). For the FSD-based experiment, two vortex micropumps were connected to the FSD active micromixer with 2.0 mm internal diameter tubes (Figure 32 (b)). A dual-output power supply was used to drive the micropumps. The working voltages of the micropumps were 0.4 – 2.5 V. To illustrate the mixing performance, two fluids with different colors (water and red dye) were chosen as solution entering through the inlets. In the mixing chamber, the mechanical vibration of the piezoelectric diaphragm was used to enhance mixing rate. The voltage input of the diaphragm was produced by a signal generator and a power amplifier. Afterwards, the mixed fluid was passed to the mixer outlet.

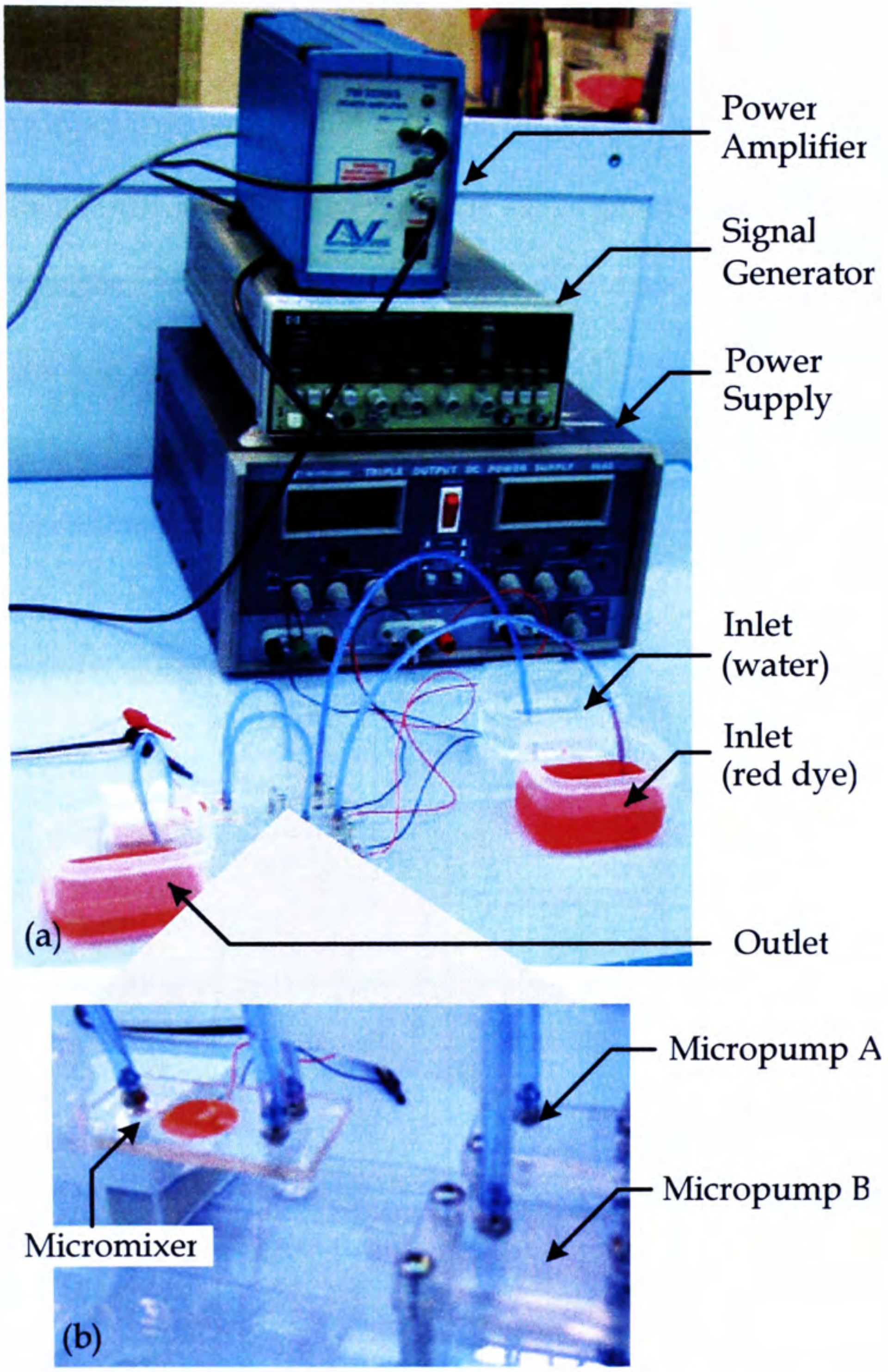

Figure 32. Configuration of the mixing performance experiment.

In an initial experiment, both micropumps were driven by 0.9 V input voltage. When fluids were pumped into the chamber, they could not mix up because of the laminar flow as shown in Figure 33 (a). A sharp and straight interfacial line between water and red dye indicated the balanced pump pressure between the two micropumps. A 55 V peak-to-peak square wave signal was applied to the FSD active micromixer at

10 s. The mechanical vibration could greatly enhance the mixing rate inside the chamber (Figure 33 (b)). The resonant frequency of the diaphragm was obtained with 0.9 kHz input frequency. Fluid could be thoroughly mixed and be retained after 1 min (Figure 33 (c)). After we turned off the signal generator at 1 min 20 s, the fluid inside the chamber was reverted to be half red and half transparent. The typical restoring time was around 1 min 30 s (Figure 33 (d) – (e)). At 4 min 0 s, the input signal was applied to the micromixer again. Then the mixer was turned off at 5 min 5 s. Repeatable results could be obtained in our experiment (Figure 33 (f) – (i)).

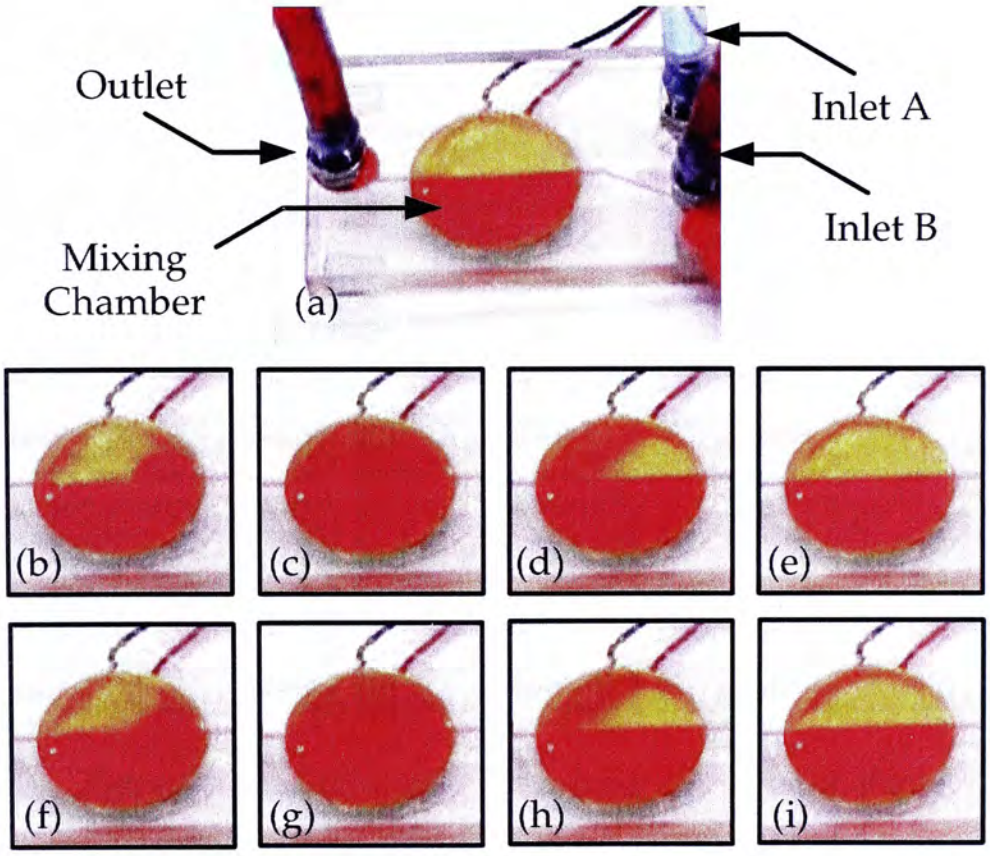

Figure 33. Fluid inside mixing chamber during experiment at (a) 0 s, (b) 20 s, (c) 1 min 10 s, (d) 1 min 47 s, (e) 2 min 55 s, (f) 4 min 18 s, (g) 5 min 5 s, (h) 5 min 45 s and (i) 6 min 40 s.

Another initial experiment was also performed to verify the mixing capability of the PSD active micromixer. The experimental setup was the same as the one shown in Figure 32 except for the micromixer and the variation of the input frequency. The

FSD active micromixer was replaced with the PSD active micromixer, which was driven by 55 V peak-to-peak bipolar square wave voltage at a frequency of 1.4 kHz. The fluid pattern inside the chamber during experiment is shown in Figure 34. The mixing time was about 5 s (Figure 34 (a) – (c)) and the restoring time remained 1 min 30 s (Figure 34 (c) – (e)). Moreover, the results are reproducible (Figure 34 (e) – (i)). This demonstrated that adding pillars inside the mixing chamber could help further induce significant improvement on the mechanical vibration based fluid mixing.

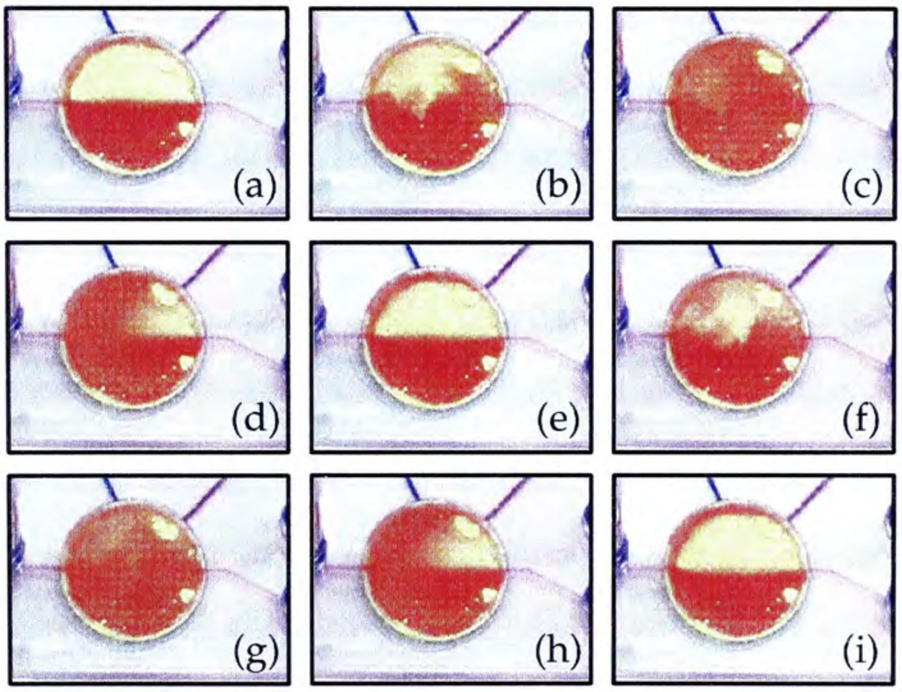

Figure 34. Fluid inside the mixing chamber of the PSD active micromixer during experiment at (a) 0 s, (b) 1 s, (c) 5 s, (d) 15 s, (e) 95 s, (f) 97 s, (g) 100 s, (h) 111 s and (i) 176 s.

The input voltage frequency, peak-to-peak voltage and fluid flow rate are the important factors for the FSD and PSD active mixing performance, other than the chamber geometry. The relationship between the mixing time and the related factors were investigated experimentally. The mixing time of the FSD and PSD active micromixers for different input frequencies, peak-to-peak voltages and fluid flow rates are shown in Figure 35. For the microfluidic mixing with 55 v peak-to-peak voltage and 1.2 ml/min fluid flow rate (Figure 35 (a)), the mixing time could be regulated by the oscillating frequency. Thorough mixing occurred when the input frequencies were greater than 0.6 kHz and 0.5 kHz for the FSD and PSD active micromixers, respectively. For input frequency greater than 9 kHz, the mixing enhancement by the diaphragm vibration became insignificant. The optimal mixing time of the FSD active micromixer was 60 s at a frequency of 0.9 kHz, and the optimal mixing time of the PSD active micromixer was 2 s at a frequency of 1.5 kHz. In the mixing experiment with controlled 1.5 kHz oscillating frequency and 1.3 ml/min flow rate (Figure 35 (b)), a driving power with higher peak-to-peak voltage could contribute to the mixing performance. Mixing inside the chamber could be obtained with 44 V and 49 V peak-to-peak voltages for the FSD and PSD mixers, respectively. With 83 V peak-to-peak voltages, the mixing time could be shortened to 11 s for FSD mixer, and 2 s for PSD mixer. Furthermore, less mixing time was required for the slow fluid flow. In the experiment with constant input frequency (1.5 kHz) and peak-to-peak voltage (55 V), the pumping discharge was a determinative factor for the microfluidic mixing (the fluids could not be mixed with >1.6 ml/min discharge in the FSD active micromixer). When the fluids were in static state, 0 ml/min discharge, the mixing performance could be further improved to 23 s and 2 s for the FSD and PSD micromixers, respectively.

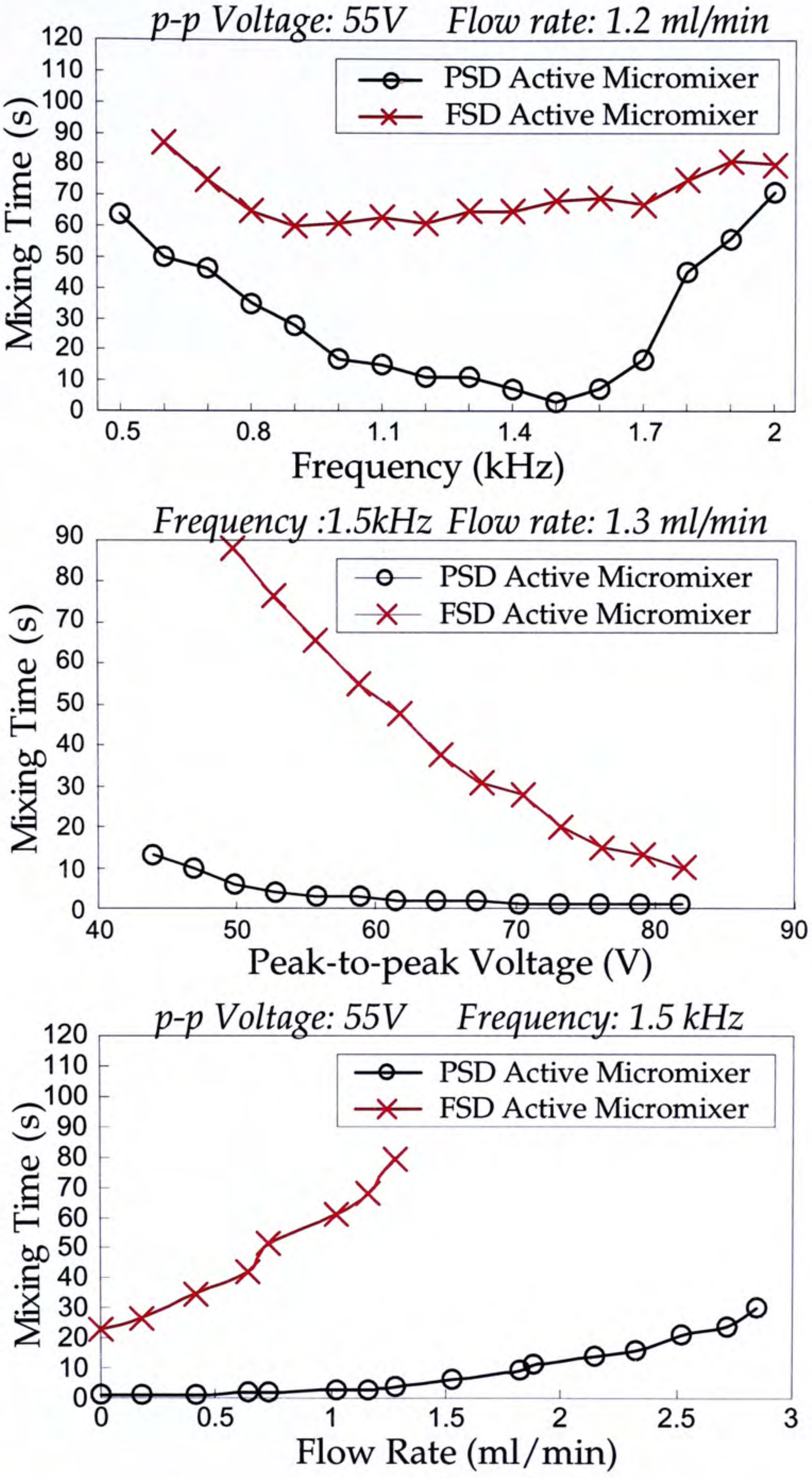

Figure 35. Mixing Time of the FSD and PSD active micromixers corresponding to different (a) input frequencies, (b) peak-to-peak voltages and (c) fluid flow rates.

It can be observed that the optimal input frequency for the mixing of the FSD active micromixer is 0.9 kHz, and the optimal input frequency for the mixing of the PSD active micromixer is 1.5 kHz, which are related to the resonant frequencies of the diaphragms. The mixing performance can be enhanced by higher peak-to-peak voltage and lower fluid flow rate. The experimental results are coincident to the conditions discussed in section 4-1-1. Moreover, all experimental results indicate that the pillars could further shorten the required mixing time. The exhaustive experimental data obtained from our micromixers can greatly help microfluidic device designers to develop optimal and effective FSD or PSD micromixers for different applications in the future.

CHAPTER
FIVE

MICROFLUIDIC FLOW PLANNING SYSTEM

5-1 SYSTEM DESIGN

5-1-1 Chip Design and Fabrication

Most microfluidic devices are designed with planar structures, which contain inlets and outlets for fluidic connections. With the conformable fluidic adaptors, tubes can be used to link up the individual devices as an integrated system. The microfluidic system can perform the complete functionality for a particular application. The experimental setup introduced in section 4-3 is an example of the modular integration. In this section, a microfluidic system integrated with a polymer-based 2 × 2 chamber array and sixteen vortex micropumps is presented. This can also demonstrate the capability of fluid flow control using the controllable pumping sequence of multiple micropumps.

The schematic of the integrated microfluidic system, which has multiple detection chambers that can allow diverse bio-solutions to be transported, is illustrated in Figure 36. This system was successfully built and tested with rudimentary experiments. The microfluidic chip consisted of four microchambers and sixteen inlets. Solutions were pumped to the inlets by vortex micropumps. In each chamber, any combination of the four inlet chemicals could be prepared by adjusting the flow rate of micropumps (A – D). With the designed channel configuration, samples could be delivered to the four target chambers (1 – 4) by micropumps. Each micropump was used to adjust the fluid flow rate from a particular chemical inlet to a target chamber. The combination and concentration of chemicals were controlled by the pump rate ratios among the micropumps. Integrating with the motor control system discussed in the next section, the system enabled the parallel sample preparations of the four microchambers, with different pump rates and chemical combinations.

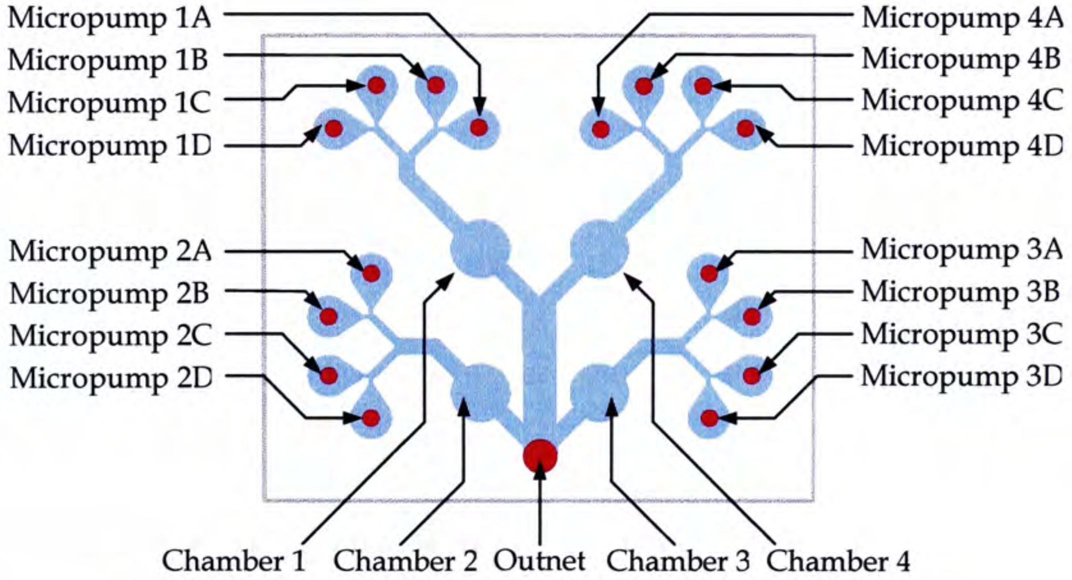

Figure 36. Pattern design of the microfluidic system integrated with four microchambers and sixteen inlets connected with micropumps.

The complete polymer microfluidic chip is shown in Figure 37. Red dye was inserted into the channels and chambers to illustrate the fluid flow pattern. The chamber and channel patterns on the substrate were fabricated with SU-8 photoresistive polymer. Further machining processes were performed to construct the sixteen inlets.

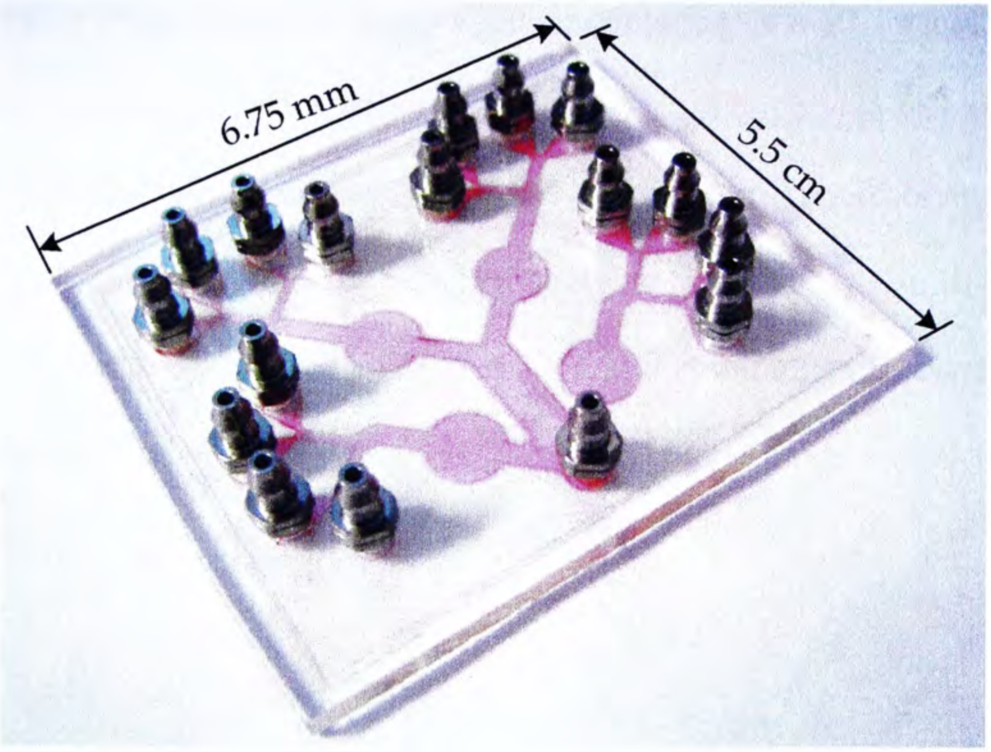

Figure 37. Photograph of the SU-8 channels on the PMMA substrate of the microfluidic system with parallel sample preparation capability.

5-1-2 Digital Controlling System

The interface hardware and software were developed to control the vortex micro pumps and eventually automate the entire bio-fluid delivery and transport process. As mentioned earlier, fluid pump rate can be controlled by the rotational speed of pump impeller. Hence, the real-time automatic fluid delivery can then be controlled by a computer. A motor control system was developed to operate multiple micropumps as shown in Figure 38 (a) and the schematic is shown in Figure 38 (b). Users could input commands with an interface program to control the pump rates of micropumps. Transmitting signals via the serial port, the motor controller would collect and decode the received commands. The motor controller was integrated with IC chips AT90S8515, MAX232 and two operational amplifier arrays (The detailed circuit design is illustrated in Appendix B). It could simultaneously activate up to sixteen micropumps simultaneously. The output signals of the motor controller were programmed in pulse-width modulation (PWM) format. Since the ratio of the equivalent output voltage V_{eq} and the peak voltage V_{peak} was equal to the ratio of its pulse width t_{pulse} and signal period T, the rotational speed of micromotors, and hence the pump rate, could be adjusted by the output pulse width. In our system, V_{peak} was 5 V and T is 3.9 ms. The desired V_{eq} could be obtained by regulating t_{pulse} between ~0.4 ms and ~2 ms.

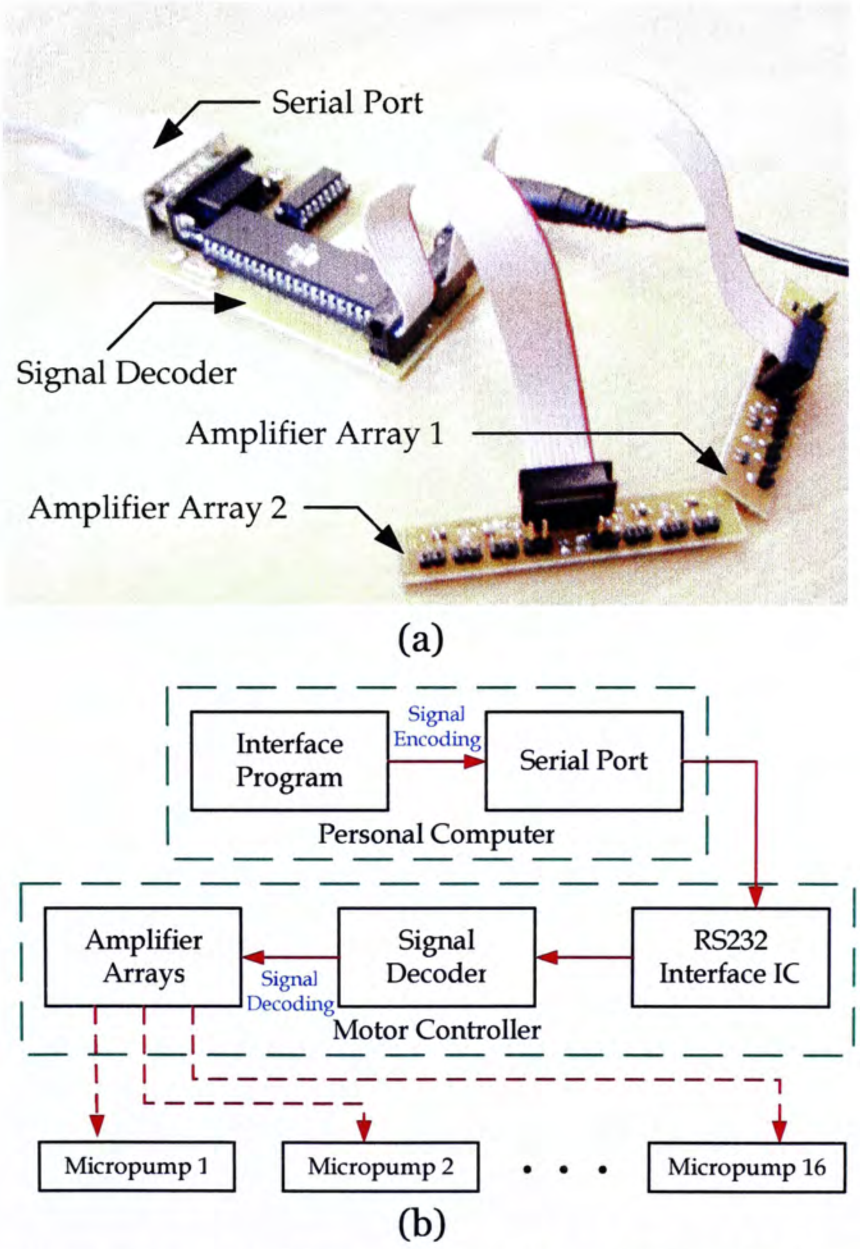

(a)

(b)

Figure 38. (a) Motor controller developed for micropump operations and (b) schematic design of the motor control system.

The interface program for the motor controller is illustrated in Figure 39. Users can control the operation of the flow planning system by switching the check boxes on the interface. After the 'Update' button is pressed, computer will encode and send the commands to the controlling circuit and so the driving voltages of vortex micropumps would update simultaneously. Besides the manual operation, the interface program can load a text file containing prescheduled operation scripts. Consequently, the operation of the flow planning system can be fully automated.

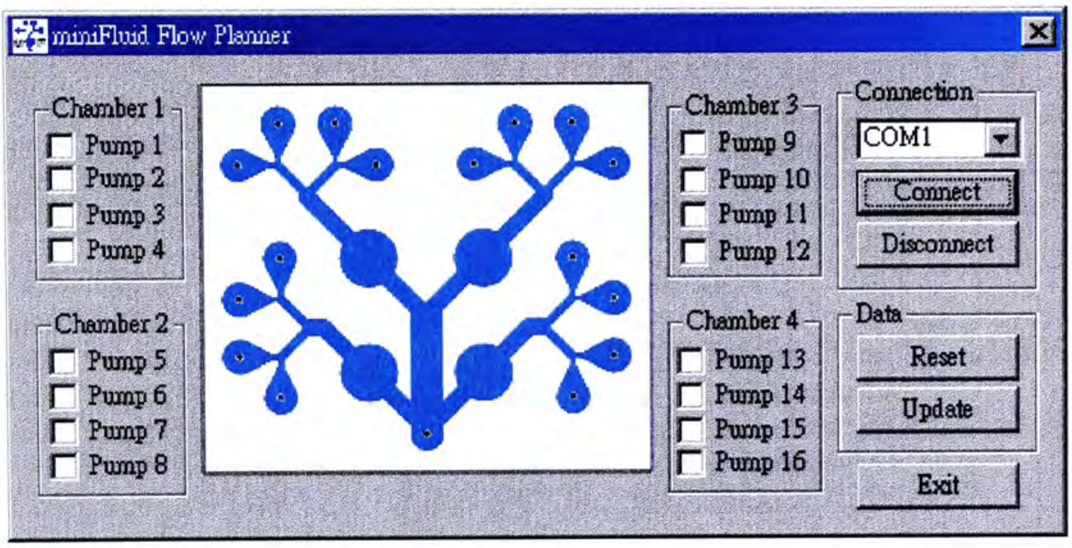

Figure 39. Interface program of the microfluidic flow planning system.

5-1-3 Operation Mechanism

The operation of the microfluidic system often requires parallel operation, i.e., multiple micropumps can operate with different pump rates at the same moment. However the information contained by each serial port data package is limited to 8 bits. An appropriate transmission protocol was designed for our application. In the motor control system, the rotational speed values of target micropumps were temporarily stored in the controller buffer. The micropumps would keep their previous rotational speeds until the updated command is sent. This approach could ensure the parallel operation of micropumps. The flow diagrams of implementation are illustrated in Figure 40. In the system, the microcontroller AT90S8515 processed the command data and the output PWM signals with UART and timer interrupt functions, respectively. The microcontroller kept swapping the output voltages and generated PWM signals by the timer interrupt. When an external command was received from the serial port, the UART interrupt function would instantly transfer the rotational speed values to the buffer storage and check whether the updating of the output voltages was needed. To update the signal outputs, the system would change the pump rates of all micropumps instantaneously.

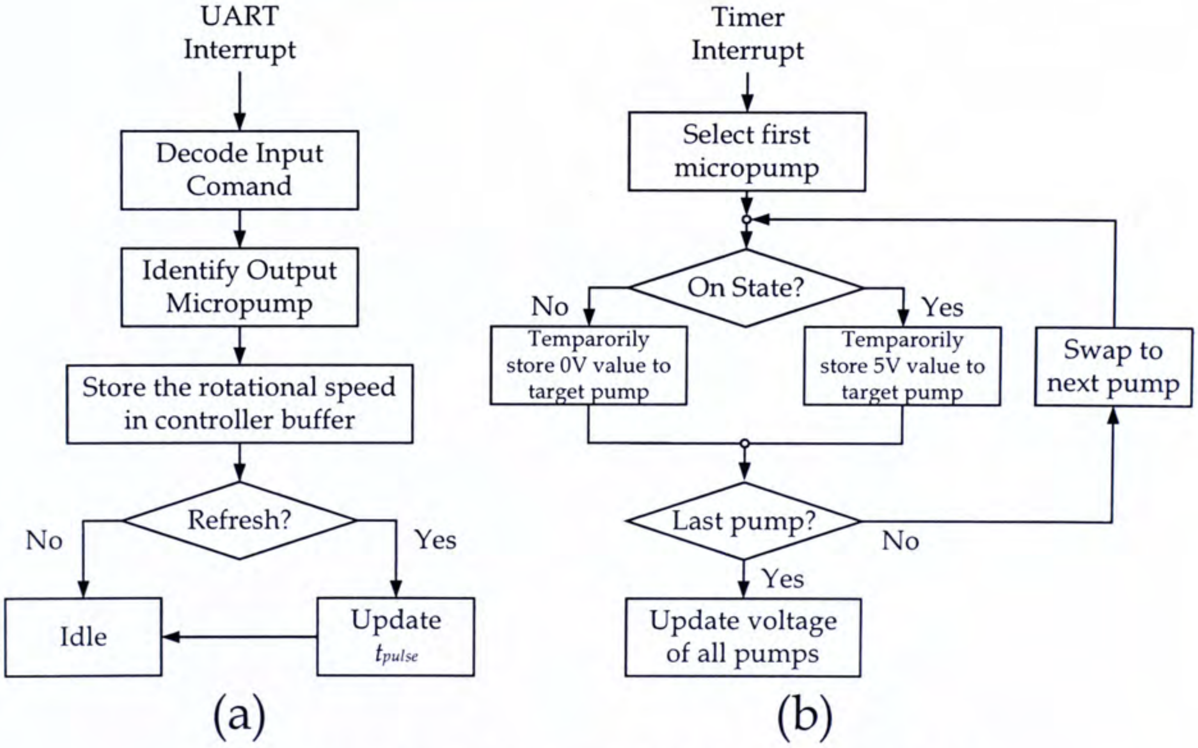

Figure 40. Flow diagrams of (a) UART and (b) timer interrupt functions adopted in the motor control system.

5-2 EXPERIMENTAL RESULTS

An experiment was also performed to illustrate the flow pattern inside the microchambers. Micropumps A and C were inserted with DI water while micropumps B and D were used to pump red dye. The flow pattern (Figure 41) indicates that all micropumps could successfully deliver inlet fluids into the target microchambers. This result shows that the parallel fluid manipulation can be achieved by 1) fabricating an array of chambers on a transparent polymer substrate, and 2) using an array of micropumps to transport different chemicals/bio-fluids into different microchambers. Essentially, the technology that we have developed is scalable, i.e., the number of vortex micropumps and number of fluid chambers can be dictated entirely by the experimental needs.

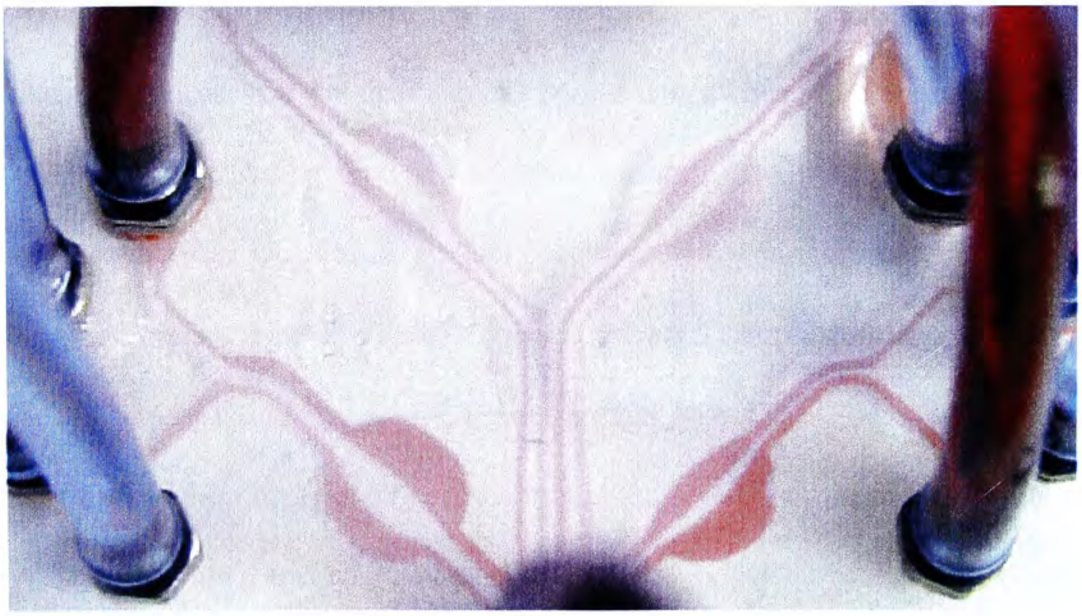

Figure 41. Fluid Pattern of the microchambers pumped with DI water (inlets B and D) and red dye (inlets A and C)

CHAPTER

SIX

MICROFLUIDIC MIXING MODULE ARRAY

6-1 SYSTEM CONFIGURATION

6-1-1 Microfluidic Chip Design

Due to the rapid advancement on the performance of the existing microfluidic devices, biological and chemical sensing systems and analyses can be practically miniaturized. However, besides improving the signal acquisition capabilities of these mini-sensing systems, the preciseness of sample preparation and handling is also a vital requirement for the system miniaturization. Most biochemical sensing components can function well within only specific ranges of environmental condition parameters. The flow rate, temperature and sample concentration control are some of the requisite factors in the biochemical sensation. The condition control in the current biochemical detection systems is achieved by macro-equipment with superior stability and accuracy. Nevertheless, the controlling equipment highly reduces the portability of the miniaturized microfluidic systems. The microfluidic system can only operate at the places where the controlling equipment is available. Moreover, the bulky fluid and electricity connections are other significant problems. Consequently, the sample preparation components and the controlling equipment should also be miniaturized and integrated into the microfluidic chip.

A digitally controllable microfluidic chip consisting of multiple mixing modules for chemical sample preparation was developed for the bio-fluid preparation applications. The microfluidic chip was capable of mixing fluid with adjustable mixing ratio, a function which could be used in applications such as surface plasmon resonance (SPR) detection of the concentration level of bio-chemicals [48]. A schematic diaphragm of the device design is shown in Figure 42. Six vortex micropumps, six tesla valves [59] and three active micromixers were integrated into a microfluidic chip using an identical Polymer-MEMS process.

In the mixing module array, we chose pillared-surface diaphragm active micromixer because it provided greater mixing rate enhancement when compared to the FSD active micromixer. For each module, two vortex micropumps were connected to the PSD active micromixer with 500 μm wide microchannels. The discharges of inlet fluids were adjustable with different input voltages of micropumps. As mentioned in section 1-2-3, when fluids were first pumped into the mixing chamber, they could not mix easily due to the laminar flow in the chamber. But, by applying appropriate input voltage, the micromixer could enhance the mixing rate inside the chamber by the mechanical vibration of diaphragm. The mixing performance of each mixing module was identical to the characteristics of the PSD micromixer discussed in section 4-4. In each mixing module, a chemical could be pumped into an inlet, while another inlet was pumped with DI water (or any given solution). The concentration of chemical could be controlled by the pumping rate ratio between the two vortex micropumps. After the fluids mixed thoroughly inside the microchamber, a specific chemical with desired concentration could be obtained at the outlet of each mixing module.

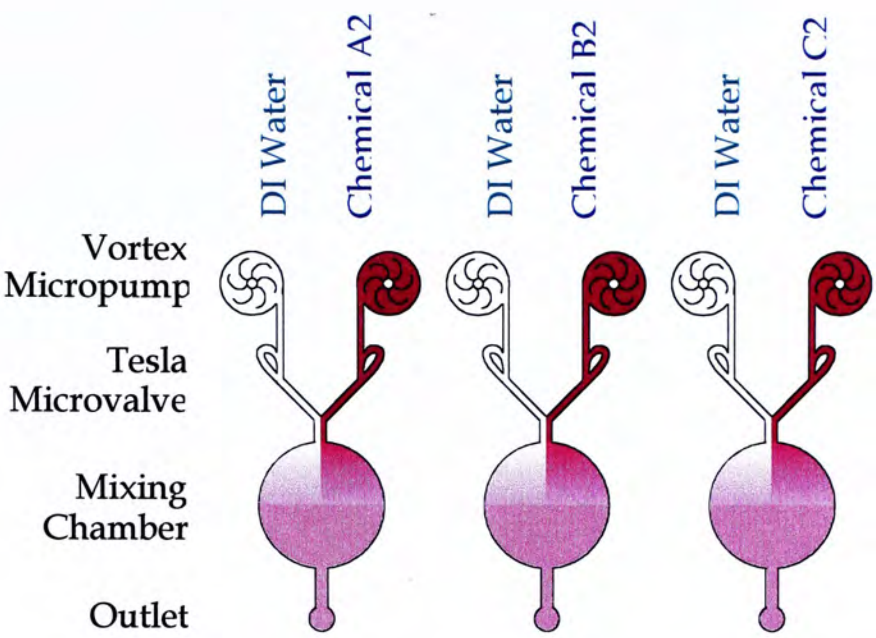

Figure 42. Schematic drawing of the digitally controllable mixing module array.

6-1-2 Backward Flow Elimination by Tesla Valve

In each mixing module, the fluid pumping of a micropump can induce backward fluid flow in another pump channel. A typical example is a “Y”-shape microchannel with two micropumps as illustrated in Figure 43. When micropump A is on and micropump B is off, the pumping pressure of micropump A causes backward flow in pump channel B (Figure 43 (a)), and vice versa (Figure 43 (b)). The flow leakage problem will reduce the pumping efficiency and, at the same time, cause an unexpected flow in the adjacent channel.

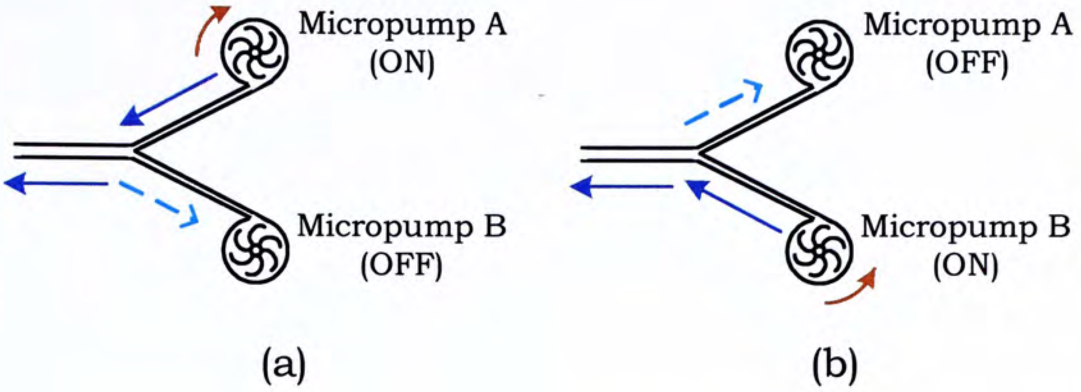

Figure 43. Backward fluid flows in "Y"-shape microchannel caused by (a) micropump A and (b) micropump B.

To eliminate the interference of the pressure between different micropumps, tesla valves can be added in the inlet channels. The geometry design of tesla valve is illustrated in Figure 44. When the fluid passes through the valve in the backward direction, the flow direction of the turning channel should be from A to B. The flow pressure induced at region B can reduce the further backward flow and retain the flow rate of the adjacent output channel.

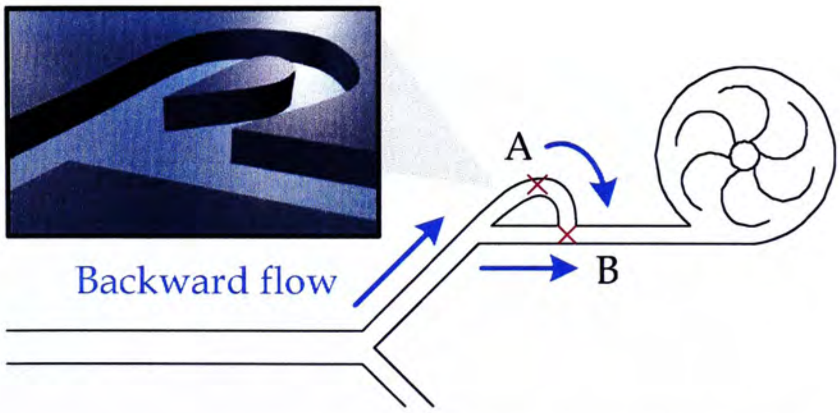

Figure 44. Top view and isometric view of the tesla valve geometry.

A simulation on the fluid flow in a tesla valve was performed to investigate the backward flow resistance by the valve geometry. Average flow velocity of 3 cms^{-1} was set at the valve inlet for forward fluid flow while the same velocity was set at the outlet for backward flow. Results showed that the back pressure in the forward flow and backward flow simulations were 0.41656 kPa and 1.28528 kPa, respectively. The pressure difference between the flows in different directions shows that the flow rectification property can effectively reduce the backward flow problem in microchannel networks.

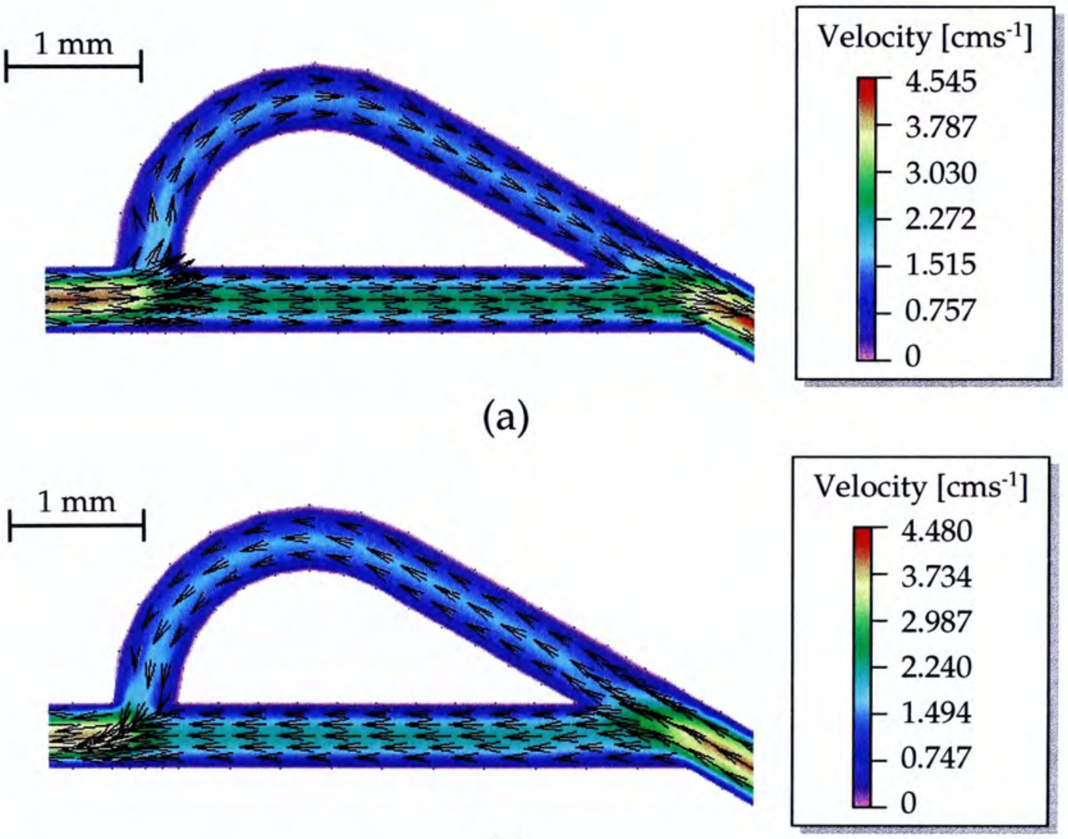

(a)

(b)

Figure 45. Simulation results of (a) forward and (b) backward flows of tesla valve.

6-1-3 System Controller and Operation Mechanism

The microfluidic mixing module array could be controlled by the identical digital control system described in section 5-1-2. Based on the fluid flow characteristics of vortex micropump, multiple fluids with variable proportion could be pumped with digital input voltage. Besides, the microfluidic mixer used square wave input voltage to actuate the diaphragm vibration. Therefore, a digitally controllable microfluidic mixing system can be integrated with the mixing and pumping devices. However, the control system needs to be modified before connecting to the mixing module array. A supplementary oscillating signal generator should be added in the output ports of micromixers (The circuitry design is presented in Appendix B). Furthermore, the interface program was modified as illustrated in Figure 46. Because the supplementary module required constant input voltage, the signal output of the mixer channels was set to steady voltages, instead of that in PWM format. Integrating the control system with the mixing module array could potentially automate the bio-fluidic manipulation and preparation.

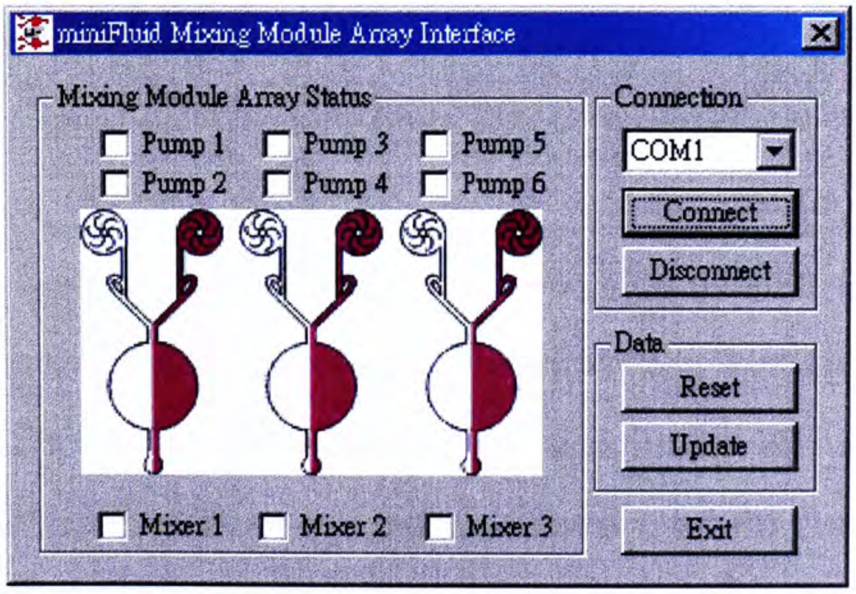

Figure 46. Layout of the interface program for the mixing module array application.

6-2 FABRICATION

The fabrication process of the microfluidic mixing module array is illustrated in Figure 47. The dimension of a fabricated microfluidic chip is 42.5 mm × 60 mm, and contains three mixing modules (Figure 48). PMMA substrate is used because of its biocompatibility and transparency. The walls of channels and chambers are patterned by photolithography. MicroChem™ SU-8 2075 photoresist is spun on the substrate at 3000 rpm rotational speed. After soft bake at 50 °C for 5 min and 70 °C for 40 min, the SU-8 layer should be exposed under the mask with the channels and chamber pattern for 60 s. Post bake should be performed at 50 °C for 30 min. The baked SU-8 should then be immersed in MicroChem's SU-8 Developer for 20 min at room temperature. The pillars could be obtained after brief rinse with isopropyl alcohol (IPA) and DI water. The second layer with chambers and channels patterns should be fabricated with the same photolithography technique. The inlets and outlet can be made by drilling holes with diameter of 2.9 mm at the patterned terminals to allow the insertion of faucets. Then a polyester film, with predrilled holes for micropumps and mixing chambers, should be bonded with the substrate using a layer of UV-curing epoxy resin, spun on at 4,000 rpm for 40 s. After UV-exposure, the closed channels can be built between the substrate and the film. Then the brass diaphragm can be bonded around the hole of polyester layer. A biocompatible diaphragm can be achieved by spinning a 40 μm layer of PDMS on the brass layer. Since a PZT ceramic layer is adhered under the diaphragm, the region below the mixing chamber could provide the mechanical oscillation of fluid. The upper and lower sides of the PZT ceramic are connected with electrical wires to receive the driving voltage. The micropump modules, each consists of a motor and an SU-8 impeller, should then be adhered to the cavity below each inlet.

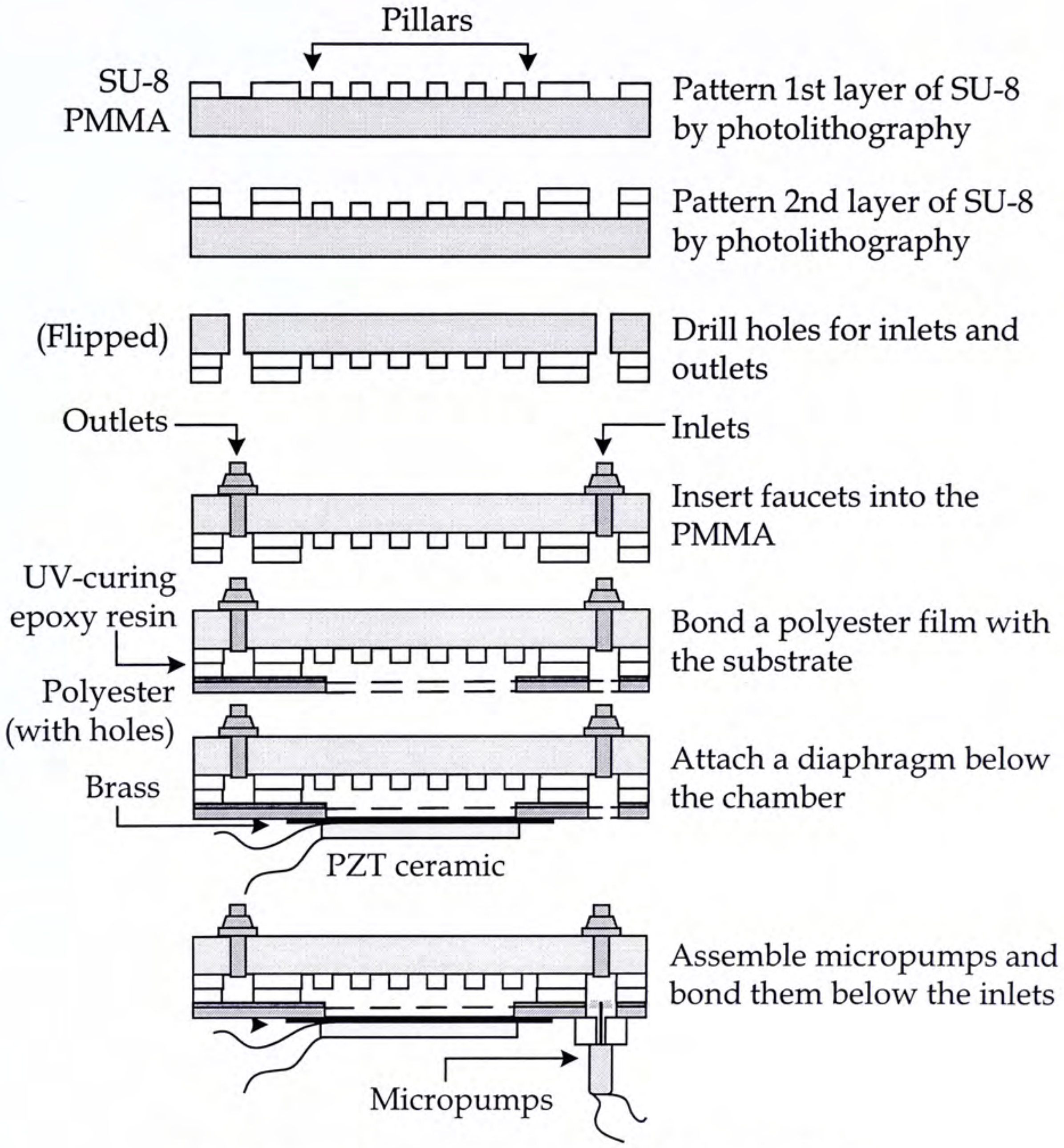

Figure 47. Fabrication process of the microfluidic mixing module array.

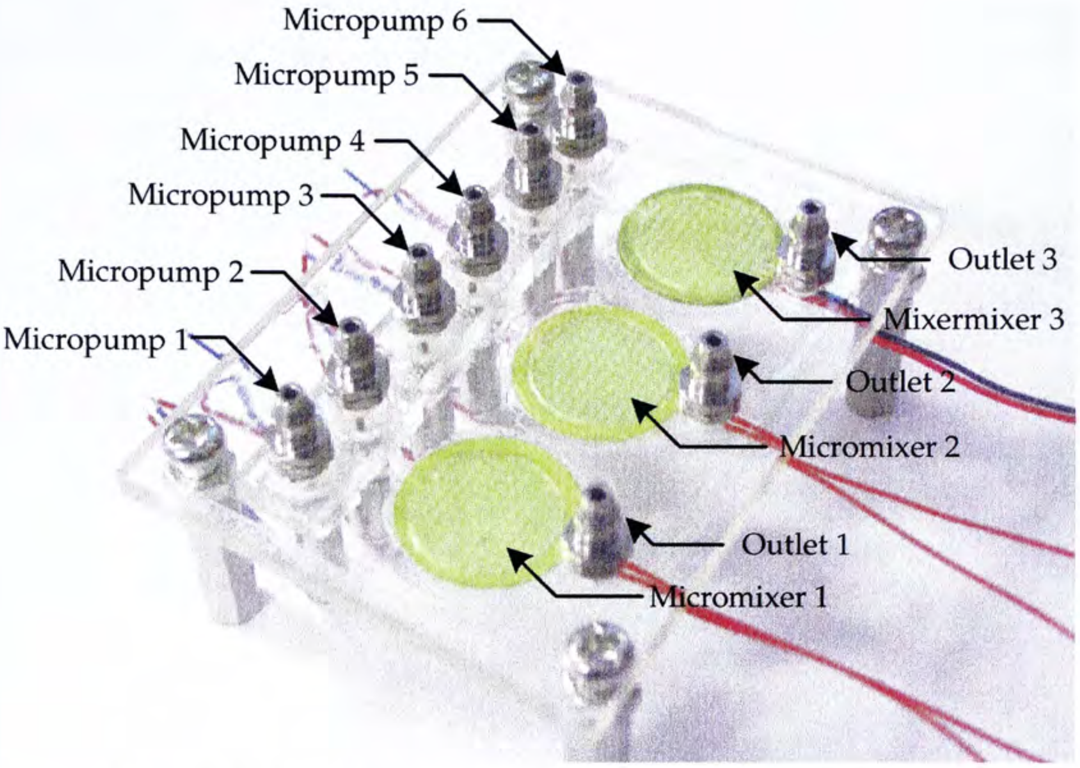

Figure 48. Photograph of an array of digitally controllable microfluidic mixing modules.

6-3 MIXING RATIO ESTIMATION

The estimation of the pumping ratio between two inlet fluids in a micromixer is complicated. Due to the geometry variation of chambers and channels, the pressure reduction of fluid flow cannot be directly predicted. Besides the approach of calculating the pumping pressure difference between two inlet channels, the ratio can also be approximated by the chamber pattern. When the micromixer is inactivated, an interfacial line can be observed inside the mixing chamber. The position of interfacial line is related to the discharge ratio, and so it can also be viewed as the visual feedback of the mixing ratio.

The discharge ratio of fluid 1 and 2 can be roughly estimated by the equation of continuity. It is assumed that the flow velocity is evenly distributed on the selected cross-section area such that the velocities of the two fluids are the same, i.e., $V_1 = V_2$

= *V*. The intermediate cross-section, *z* = *z'*, should be selected to estimate the discharge ratio. Along the cross-section, the interfacial line between fluids is sharpest since the passive mixing caused by the change of chamber geometry is minimal ($\delta x / \delta y = 0$). Given the position of an interfacial line x_i, the discharge ratio of fluid 1 and 2 would be

$$\frac{Q_1}{Q_2} = \frac{V_1 A_1}{V_2 A_2} = \frac{V(2Z)(X - x_i)}{V(2Z)(X + x_i)} = \frac{X - x_i}{X + x_i}. \tag{4.1}$$

where X equals the half of chamber width, referring to Figure 2.

However, the above linear estimation is accurate only for small $|x_i / X|$ because the velocity profile should be in the form of equation (2.5). Recall equation (2.7), the discharge of fluid 1 and 2 can be adjusted to

$$\begin{cases} Q_1(x_i) = k(\frac{4}{3}Z)(x - \frac{x^2}{X^2})\Big|_{x_i}^{X} \\ Q_2(x_i) = k(\frac{4}{3}Z)(x - \frac{x^2}{X^2})\Big|_{-X}^{x_i} \end{cases}. \tag{4.2}$$

Hence the discharge ratio can then be expressed as

$$\frac{Q_1}{Q_2} = \frac{2X^3 - 3x_i X^2 + x_i^3}{2X^3 + 3x_i X^2 - x_i^3}. \tag{4.3}$$

Note that *k* is a constant. Therefore the relation holds for fluids with different properties such as density and viscosity.

6-4 EXPERIMENTAL RESULTS

To illustrate the interfacial line and mixing performance in our experiment, DI water and red dye were used as the inlet fluids (Figure 49 (a)). When the fluids were pumped into the microchamber, the width ratio (or the ratio of cross-section area) of fluid flow, d1 / d2, could indicate the ratio of pumping volume due to the pressure imbalance inside the chamber. The flow patterns for different pumping ratio are shown in Figure 49 (b) – (d). It indicates that the mixing performance depends on the overall flow rate inside the chamber, rather than the individual fluid flow rate. Hence, the ratio of fluid flow rates can be adjusted flexibly. Based on the characteristics of vortex micropump, the pumping ratio could be estimated to obtain the desired concentration of red dye after mixing. Multiple chemicals concentration control could be achieved by replacing red dyes with the chemicals in the array of mixing modules.

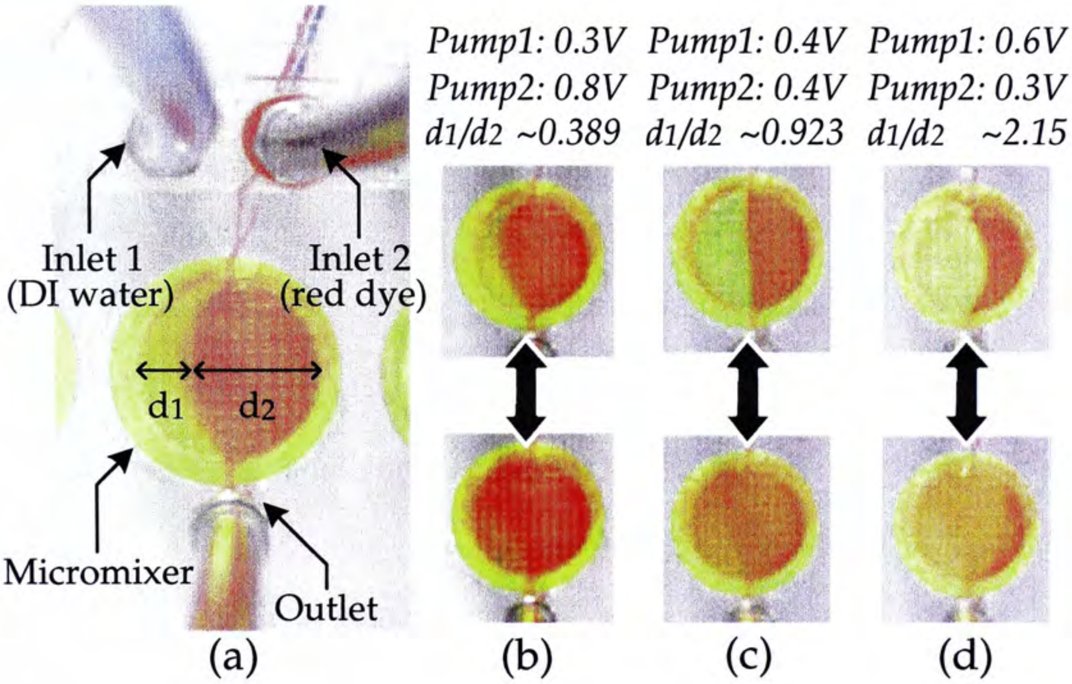

Figure 49. (a) Top view of a mixing module during operation. Ratios of pumping volume and the typical chamber patterns of mixing operations corresponding to different pump voltage inputs: (b) 0.3V:0.6V, (c) 0.4V:0.4V and (d) 0.6V:0.3V.

CHAPTER
SEVEN

CONCLUSION

The polymer-based vortex micropumps, active micromixers and tesla microvalves were successfully developed in this project. The microfluidic devices could be fabricated by hot embossing process or polymer–photolithography. In a vortex micropump, the flow rate was proportional to its applied voltage (~ 0.4 V – 2.5 V) or impeller rotational speed (up to ~5422 rpm in water). Experiments showed that the double layer impeller design could improve the pumping efficiency. In our designs, the flow rate and the pumping pressure actuated with the double layer impeller design could achieve 1.02 ml/min and 0.850 kPa at ~2.5 V, respectively. The inverted chamber configuration of vortex micropump was also developed, which could potentially be integrated with other devices into a single chip system. Furthermore, the pump model indicated that the dimension and geometry of the impeller could be adjusted for different application requirements.

Two types of micromixers, FSD and PSD active micromixers, based on the piezoelectric mechanical vibration were designed, fabricated and investigated with experiments. The experimental setup was integrated with two vortex micropumps and an active micromixer. It showed that the oscillating frequency, pump rate and peak-to-peak voltage were key factors affecting the microfluidic mixing in the micromixing chambers. The optimal frequencies of the input oscillating voltages for the FSD and PSD pumps were 1.5 kHz and 0.9 kHz, respectively. This also indicated that adding pillars could shorten the mixing time to <5 s.

We have also developed the microfluidic chip integrated with four microchambers and sixteen micropumps for the potential application of the parallel detection with multiple microchambers. The computer-controlled system could potentially automate the multiple fluid delivery and bio-detection process. Furthermore, arrayed sensing surface with multiple analyses and parallel detection chambers will certainly be a very exciting direction for the further development.

The polymer-based vortex micropump, PSD active micromixers and tesla microvalves were integrated into a microfluidic mixing module array capable of delivering and mixing multiple bio-fluids/chemicals with adjustable fluid ratios. The vortex micropumps could deliver a wide range of flow rates and pumping pressure. Moreover, the tesla valves eliminated backward flow by increasing the backpressure of the inactive pump channels. It has been shown that the proportion between two inlet fluids can be estimated analytically and be regulated with different input voltages of micropumps. We have also demonstrated the functionality of the mixing module array on chemical concentration control. The system can be extended to further integrate with other microfluidic systems, which can potentially miniaturize the fluid preparation, delivery and detection processes into a single polymer microfluidic chip. In essence, this system demonstrates a technology that can be extended to build large-scale integrated microfluidic system.

CHAPTER

EIGHT

FUTURE WORK

8-1 SELF DRIVEN MICROFLUIDIC FLOW PLANNING SYSTEM

Further integration of the microfluidic flow planning system can greatly reduce the chip size and inlet connections as illustrated in Figure 50. The microfluidic chip consists of four microchambers and sixteen micropumps. It is designed to prepare samples with any combination of the four crude chemicals (A – D). The pattern design can reduce the fluidic connection from sixteen to four inlets. In the microfluidic chip, the dual-layer configuration of the microchannels would effectively increase the capability of fluid flow manipulation. Channel patterns are fabricated on both upper and lower sides of the substrate, linked with the vertical microchannels (diameter 500μm). The channel pattern on the substrate should be fabricated with SU-8. Further machining processes should then be performed to construct inlets, outlets, impeller chambers and the linking holes between upper and lower microchannels.

With the designed channel configuration, samples could be delivered to the four target chambers (1 – 4) by micropumps. Each micropump is used to adjust the fluid flow rate from a particular chemical inlet to a target chamber. The combination and concentration of chemicals can be controlled by the pump rate ratios among the micropumps. Integrated with the motor control system discussed in section 5-1-2, the system potentially enables the parallel sample preparations of the four microchambers, with different pump rates and chemical combinations.

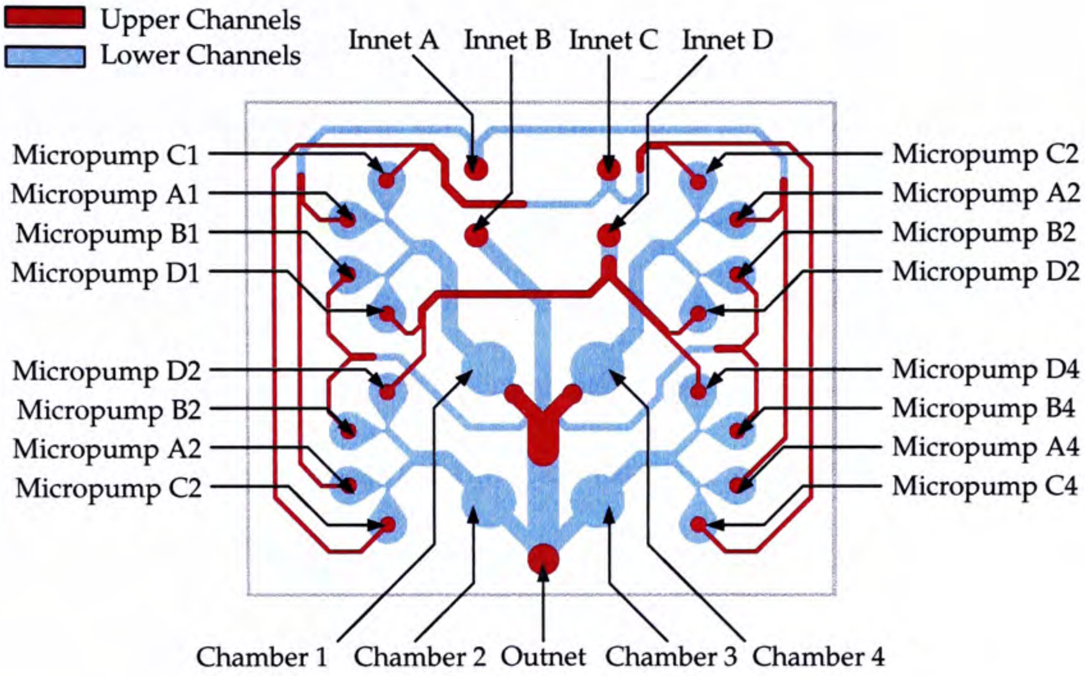

Figure 50. Channel design of the microfluidic system integrated with four microchambers and sixteen micropumps.

8-2 MIXING ENHANCEMENT BY CAVITATION MICROSTREAMING

The micromixing can also be enhanced by the bubble-induced acoustic microstreaming [60], in addition to the chamber diaphragm vibration. When an acoustic wave is transferred into a solution, the air bubbles inside the solution will vibrate under the frequency of the applied wave. The expansion and contraction of the bubbles can be viewed as the oscillation of a circular membrane. It was also discovered in [61] that the performance of mixing enhancement was predominantly determined by the resonance characteristics of air bubbles. The relation between the resonance frequency f and the radius r of an air bubble can be expressed as

$$f = \frac{\sqrt{3\gamma P / \rho}}{2\pi r} \tag{8.1}$$

where γ is the specific heat of air, P is the hydrostatic pressure in dynes/cm^2 and ρ is the solution density in g/cc.

A bubbled-surface diaphragm (BSD) active micromixer using the technique of cavitation microstreaming can be achieved by a modified chamber design as illustrated in Figure 51. In the modified micromixer, the mixing enhancement element is an array of air bubble, instead of the SU-8 pillars. Multiple air bubbles with fixed size can be trapped by the cylindrical caves fabricated on the top size of the microchamber. When a fluid is pumped into the micromixer, it will not fill into the caves because of significant cave depth. The optimal dimension of the cave can be estimated using equation (8.1). For instance, with $\gamma = 1.4$, $P = 106$ dynes/cm^2, $\rho = 1.0$ g/cc and the resonant vibration frequency $f = 5$ kHz, the cave radius can be calculated as 0.65 mm [43]. Furthermore, the BSD active micromixer can still retain the flat geometry on the top side of microchamber, and so this design should be applicable for solutions and fluids that containing mixtures.

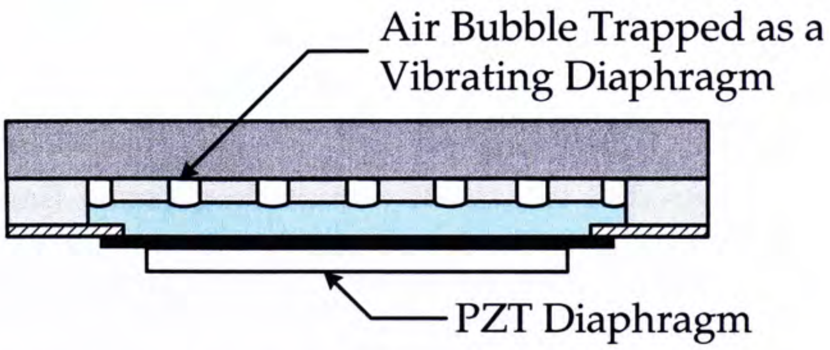

Figure 51. Cross section schematic of a BSD active micromixer.

The proposed fabrication process of the BSD mixer is identical to the PSD one. Double-layer photolithography process should be used to fabricate the flow patterns as illustrated in Figure 52. The first layer of SU-8 can construct the structure of air traps while the second layer of SU-8 should contain the pattern of chamber and channels. The complete fabrication process can be referred to section 4-2-2 (except the pattern of the photolithography process).

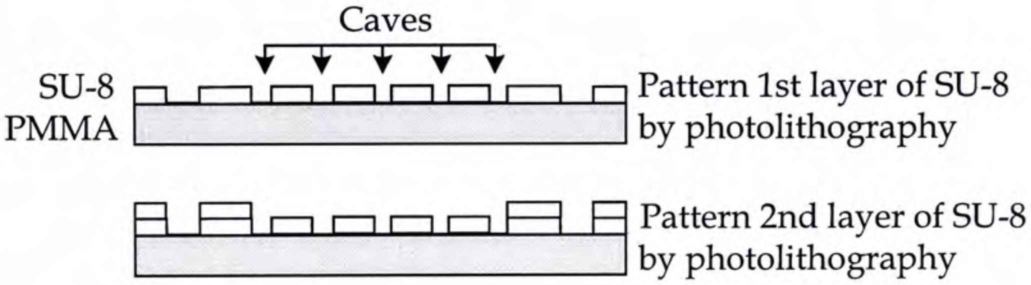

Figure 52. Photolithography process of the BSD active micromixer.

It has been shown an acoustic based on cavitation microstreaming could induce micromixing for 2 min [43]. The device was actuated with only 5 V peak-to-peak voltage at 5 kHz frequency. The chamber design of the BSD mixer is a combination of two mixing components: a PZT-oscillating diaphragm and an array of passively vibrating bubbles. By varying the dimension of cylindrical caves, the resonant vibration frequency of trapped bubbles could match that of the diaphragm and obtain the optimal mixing performance. Hence, the BSD active micromixer can potentially further enhance the PZT-driven mixing performance.

REFERENCES

[1] Tai-Ran Hsu, "MEMS and Microsystems: Design and Manufacture," McGraw-Hill, 2002.

[2] K. J. Gabriel, W. S. N. Trimmer and J. A. Walker, "A Micro Rotary Actuator Using Shape Memory Alloys," Sensors and Actuators (A), vol. 15, pp 95-102, 1988.

[3] Andrew R. Atwell, Robert S. Okojie and Kevin T. Kornegay, "Simulation, Fabrication and Testing of Bulk Micromachined 6H-SiC High-g Piezoresistive Accelerometers," Sensors and Actuators (A), vol. 104, pp 11-18, 2003.

[4] Heng Yang, Minhang Bao, Hao Yin and Shaoqun Shen, "A Novel Bulk Micromachined Gyroscope Based on a Rectangular Beam-mass Structure," Sensor and Actuators (A), vol. 96, pp 145-151, 2003.

[5] P. Bley, "The LIGA Process for Fabrication of Three-Dimensional Microcale Structures," Interdisciplinary Science Reviews, vol. 18, no. 3, pp 267-272, 1993.

[6] Stephen D. Senturia, "Microsystem Design," Kluwer Academic Publishers, Norwell, Massachusetts, USA, 2000.

[7] Y. N. Xia and G. M. Whitesides, "Soft Lithography," Annual Review of Materials Science, vol. 28, pp 153-184, 1998.

[8] Nam-Trung Nguyen and Steven T. Wereley, "Fundamentals and Applications of Microfluidics," Artech House Inc., Norwood, Massachusetts, USA, 2002.

[9] D. J. Harrison, K. Fluri, K. Seiler, Z. Fan, C. S. Effenhauser and A. Manz, "Micromachining a Miniaturized Capillary Electrophoresis-based Chemical Analysis System on a Chip," Science, vol. 261, pp 895-897, 1993.

[10] T. Thorsen, S. J. Maerkl and S. R. Quake, "Microfluidic Large-Scale Integration," Science, vol. 298, pp 580-584, 2002.

[11] R. Linnemann, P. Woias, C.-D. Senfft and J. A. Ditterich, "A self-Priming and Bubble-tolerant Piezoelectric Silicon Micropump for Liquids and Gases," Proceedings of Micro Electro Mechanical Systems 1998 (MEMS 98), pp 532-537, 1998.

[12] Chaun Hua Chen and J. G. Santiago, "A Planar Electroosmotic Micropump," Journal of Microelectromechanical Systems, vol. 11, pp 672-683, 2002.

[13] Yo Han Choi, Son Sanguk and S. S. Lee, "Novel Micropump Using Oxygen as Pumping Source," Proceedings of Micro Electro Mechanical Systems 2003 (MEMS 03), pp 116-119, 2003.

[14] Marc A. Unger, Hou-Pu Chou, Todd Thorsen, Axel Scherer and Stephen R. Quake, "Monolithic Microfabricated Valves and Pumps by Multilayer Soft Lithography," Science, vol. 288, pp 113-116, 2000.

[15] N. Vandelli, D. Wroblewski, M. Velonis and T. Bifano, "Development of a MEMS Microvalve Array for Fluid Flow Control," Journal of Microelectromechanical Systems, vol. 7, pp 395-403, 1998.

[16] Hsin Yu Wu and Cheng Hsien Liu, "A Novel Electrokinetic Micromixer," Transducers, Solid-State Sensors, Actuators and Microsystems, vol. 1, pp 631-634, 2003.

[17] Z. Yang, M. Matsumoto, H. Goto and R. Maeda, "Ultrasonic Micromixer for Microfluidic Systems," Sensors and Actuators (A), vol. 93, pp 266-272, 2001.

[18] J. D. Zahn, A. A. Deshmukh, A. P. Pissano and D. Liepmann, "Continuous On-chip Micropumping through a Microneedle," Proceedings of Micro Electro Mechanical Systems 2001 (MEMS 01), pp 503-506, 2001.

[19] Gerlinde Bedö, Heike Fannasch and Rudolf Müller, "A Silicon Flow Sensor for Gases and Liquids Using AC Measurements," Sensors and Actuators (A), vol. 85, pp 124-132, 2000.

[20] Shifeng Li and Shaochen Chen, "Analytical Analysis of a Circular PZT Actuator for Valveless Micropumps," Sensor and Actuaotr (A), vol. 104, pp 151-161, 2003.

[21] A. Bertsch, S. Heimgartner, P. Cousseau and P. Renaud, "3D Micromixers-downscaling Large Scale Industrial Static Mixers," Proceedings of Micro Electro Mechanical Systems 2001 (MEMS 01), pp 507-510, 2001.

[22] S. D. Muller, I. F. Sbalzarini, J. H. Walther and P. D. Koumoutsakos, "Evolution Strategies for the Optimization of Microdevices," Proceedings of the 2001 Congress on Evolutionary Computation, vol. 1, pp 302-309, 2001.

[23] S. Kuiper, "Fabrication of Microsieves with Sub-Micron Pore Size by Laser Interference Lithography," Journal of Micromechanics and Microengineering, Vol. 11, no. 1, pp 33-37, 2001.

[24] J. C. Rife, M. I. Bell, J. S. Horwitz, M. N. Kabler, R. C. Y. Auyueny and W. J. Kin, "Miniature Valveless Ultrasonic Pumps and Mixers," Sensors and Actuators, vol. 86, pp 135-140, 2000.

[25] N. T. Nguyen and X. Y. Haung, "Miniature Valveless Pumps Based on Printed

Circuit Board Technique," Sensor and Actuators (A), vol. 88, no. 2, pp 104-111, 2001.

[26] H. T. G. Van Lintel, F. C. M. van den Pol, and S. Bouwstra, "A Piezoelectric Micropump Based on Micromachining in Silicon, " Sensors and Actuators (A), vol. 15, pp 153-167, 1988.

[27] C. H. Ahn, and M. G. Allen, "Fluid Micropumps Based on Rotary Magnetic Actuators," Proceedings of MEMS'95, 8th IEEE International Workshop on Micro ElectroMechanical System, Amsterdam, pp 408-412, Netherlands, 1995.

[28] M. J. Madou, et al., "Design and Fabrication of CD-Like Microfluidic Platforms for Diagnostics: Microfluidic Functions," Journal of Biomedical Microdevices, vol. 3, no. 3, pp 245-254, 2001.

[29] J. R. Webster, et al., "Electrophoresis System with Integrated On-Chip Fluorescence Detection," Proceedings of MEMS'00, 13rd IEEE International Workshop Micro Electromechanical System, pp 306-310, Japan, 2000.

[30] W. E. Morf, O. T. Guenat and N. F. de Rooij, "Partial Electroosmotic Pumping in Complex Capillary Systems. Part 1: Principles and General Theoretical Approach," Sensors and Actuators (A), vol. 72, pp 266-272, 2001.

[31] S. Shoji and M. Esashi, "Microflow Devices and Systems," Journal of Micromechanics and Microengineering, vol. 4, pp 157-171, 1994.

[32] E. Stemme, and G. Stemme, "A Valveless Diffuser/Nozzle-Based Fluid Pump," Sensors and Actuators (A), vol. 39, pp 159-167, 1993.

[33] N. Tesla, "Valvular Conduit," US patent, no. 1,329,559, 1920.

[34] M.A. Unger, H.-P. Chou, T. Thorsen, A. Scherer and S.R. Quake, "Monolithic Microfabricated Valves and Pumps by Multilayer Soft Lithography", Science, vol. 288, pp 113-116, 2000.

[35] M. Esashi, S. Shoji and A. Nakano, "Normally Closed Microvalve and Micropump Fabricated on a Silicon Wafer," Proceedings of MEMS'89, 1st IEEE International Workshop Micro Electromechanical System, pp 29-34, UT, 1989.

[36] M. Shikida and K. Sato, "Characteristics of an Electrostatically-Driven Gas Valve Under High-Pressure Conditions," Proceedings of MEMS'94, 7th IEEE International Workshop Micro Electromechanical System, pp 235-240, Japan, 1994.

[37] R. Miyake, T. S. J. Lammerink, M. Elwenspoek and J. H. J. Fluitman, "Micromixer with Fast Diffusion," Proceedings of Micro Electro Mechanical Systems 1993 (MEMS 93), pp. 248-253, 1993.

[38] J. Branebjerg, et al., "Fast Mixing by Lamination," Proceedings of MEMS'96, 9th IEEE International Workshop on Micro Electromechanical System, pp 441-446, CA, 1996.

[39] R. M. Moroney, R. M. White and R. T. Howe, "Ultrasonically Induced Microtransport," Proceedings of MEMS'91, 3th IEEE International Workshop on Micro Electromechanical System, pp 277-282, Japan, 1991.

[40] H. H. Bau, J. Zhong and M. Yi, "A Minute Magneto Hydro Dynamic (MHD) Mixer," Sensors and Actuators (B), vol. 79, no. 2-3, pp 207-215, 2001.

[41] Stoll, "Electrofluidic Circuit Board Assemply with Flud Ducts and Electrical Connections," US patent, no. 4,549,248.

[42] J. C. Fettinger, "Staked Modules for Micro Flow Systems in Chemical Analysis Cncept and Studies using an enlarged model," Sensors and Actuators (B), vol. 17, no. 19, 1993.

[43] Francis E. H. Tay, "Microfluidics and BioMEMS Applications," Kluwer Academic Publishers, Norwell, MA, 2002.

[44] Matthew W. Losey, Rebecca J. Jackman, Samara L. Firebaugh, Martin A. Schmitt and Klavs F. Jensen, "Design and Fabrication of Microfluidic Devices for Multiphase Mixing and Reaction," Journal of Microelectromechanical Systems, vol. 22, no. 6, 2002.

[45] M. Heckele, W. Bacher and K. D. Müller, "Hot Embossing – The Molding Technique for Plastic Microstructures," Microsystem Technologies, vol. 4, pp. 122-124, 1998.

[46] M. Niggemann, W. Ehrfeld, L. Weber, R. Günther and O sollbhömer, "Miniaturized Plastic Micro Plates for Applications HTS," Microsystem Technologies, vol. 6, pp. 48-53, 1999.

[47] K. Kim, S. Park, J.-B. Lee, H. Manohara, Y. Desta, M. Murphy and C. H. Ahn, "Rapid Replicatioin of Polymeric and Metallic High Aspect Ratio Microstructures Using PDMS and LIGA Technology," Microsystem Technologies, vol. 9, pp. 5-10, 2002.

[48] Raymond H. W. Lam, Kin Fong Lei, Lei Miao, Zaili Dong, Wing Cheung Law, Yick Keung Suen, Wen J. Li, Aaron Ho Pu Ho and Siu-Kai Kong, "Towards Automating Micro Cellular Detection Process Using Micro Vortex Pump Arrays", IEEE/ASME International Conference on Advanced Intelligent Mechatronics, Monterey, California, 2005.

[49] Frank M. White, "Fluid Mechanics," McGraw-Hill, Hightstown, NJ, 1994.

[50] Raymond Mulley, "Flow of Industrial Fluids-Theory and Equations," CRC Press, Boca Raton, Florida, 2004.

[51] Samir Bandib and Olivier Français, "Analytical Study of Microchannel and Passive Microvalve – Application to Micropump Simulator," Design, characterization and packaging for MEMS and Microelectronics II,

Proceedings of SPIE, Australia, 2001.

[52] Josh H. M. Lam, Raymond H. W. Lam, Kin Fong Lei, Winnie W. Y. Chow and Wen J. Li, "A Polymer-based Microfluidic Mixing System Driven by Vortex Micropumps," 5th World Congress on Intelligent Control and Automation, China, 2004.

[53] Kin Fong Lei, Raymond H. W. Lam, Josh H. M. Lam and Wen J. Li, "Polymer-based Vortex Micropump Fabricated by Micro Molding Replication Technique," IEEE/RSJ International Conference on Intelligent Robots and Systems 2004, Japan, 2004.

[54] Raymond H. W. Lam, Josh H. M. Lam, Kin Fong Lei and Wen J. Li, "Digitally Controllable Large-Scale Integrated Microfluidic Systems," IEEE International Conference on Robotics and Biomimetics, China, 2004.

[55] Kin Fong Lei, Wen J. Li and Yeung Yam, "Fabrication, Modeling, and Experimental Analysis of a Novel Vortex Micropump for Applications in PMMA-Based Micro Fluidic Systems," submitted to Journal of Micromechanics and Microengineering, 2005.

[56] Kin Fong Lei, Wen J. Li and Yeung Yam, "Microfluidic Discretized Mixing by Vortex Micropump," accepted in Transducer 2005, 13th International Conference on Solid State Sensors, Actuators and Microsystems, Korea, 2005.

[57] Tasos C. Papanastasiou, "Applied Fluid Mechanics", P T R Prentice Hall, 1994.

[58] Z. Yang, M. Matsumoto, H. Goto, M. Matsumoto and R. Maeda, "Ultrasonic Micromixer for Microfluidic Systems", Sensors and Actuators, vol. 93, pp. 266-272, 2001.

[59] F. K. Forster, L. Bardell, M. A. Afromowitz, N. R. Sharma and A. Blanchard, "Design, Fabrication and Testing of Fixed-valve Micro-pumps," ASME Annual Meeting in Fluids Engineering Division 1995, USA, 1995.

[60] R. H. Liu, R. Lenigk, R. L. Druyor-Sanchez, J. Yang and P. Grodzinski, "Hybridization Enhancement Using Cavitation Microstreaming," Analytical Chemistry, vol. 75, no. 8, pp 1911-7, 2003.

[61] S. A. Elder, "Cavitation Microstreaming," J. Acoust. Soc. Am., vol. 31, no. 54, 1959.

APPENDIX

A

BONDING TEST ON UV-CURING EPOXY RESIN

Polymer is a kind of materials that is non-reactive to many chemicals and is biocompatible. Therefore, the adhesion between polymer layers becomes a challenge on the fabrication process. Adhesives are usually used to provide the bonding force between layers. Hence, an appropriate adhesive is necessary to be chosen to achieve the desirable bonding profile of channels.

UV-curing epoxy resin was used as adhesive in both the micropump and the micromixer. To examine the quality of adhesion, a bonding strength test was performed by the MTS system as shown in Figure 53. A layer of UV-curing epoxy resin was used to bond a polyester film with two PMMA substrates. Two external PMMA sheets adhered to both the top and bottom surfaces of the sample using Chloroform. After the PMMA sheets were mounted on the machine, the bonding strength of an adhesion layer was measured by vertically pulling the sample. The bonding strength was >0.856 MPa, which was sufficient to bond the polymer layers. Thickness of the interfacial layer did not have significant effect on the bonding strength. However, a larger bonding area contributed to a stronger bonding strength.

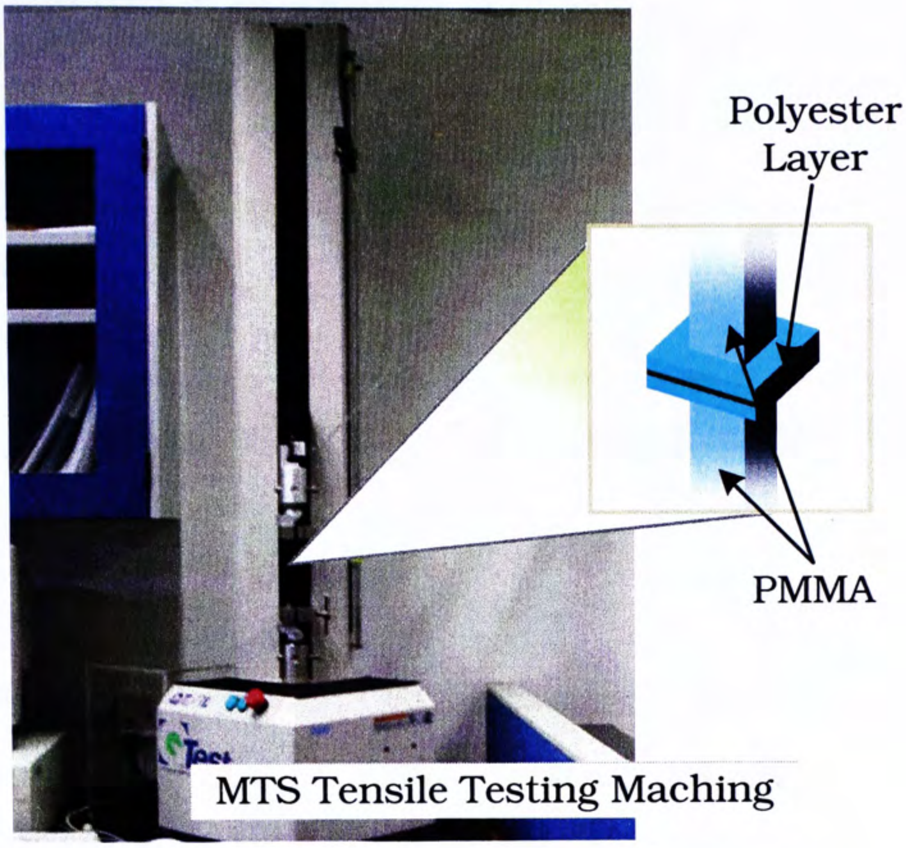

Figure 53. The tensile bonding test used MTS tensile testing machine. In the experimental setup, two PMMA adhered to the top and bottom surfaces of the bonded substrates to fit the grippers of the machine.

APPENDIX
B

CIRCUIT SCHEMATIC OF DIGITAL CONTROLLER

The circuit design of the digital control system described in section 5-1-2 and 6-1-3 is illustrated in Figure 54. The driving power of the system (port A) required 9 V voltage and 1 A current. The 3 V and 5 V step-down regulators were used to adjust input voltages for the signal processing board and the amplifier arrays, respectively. Operation commands were read from the serial port (port C). The microprocessor 8515 would decode the received commands and generate the output voltage in PWM format with two ports (PA and PC). The microprocessor board was connected to two amplifier arrays (Each array contained eight amplifiers). Because of the input voltage of amplifiers, the PWM signals would scale down to 3 V on-state voltage with larger maximum current. Connecting to the output ports (port D and E), target microfluidic devices could be controlled by the controller interface program eventually.

Some microfluidic devices require oscillating driving power, for example the micromixers presented in this dissertation. Hence an additional signal conversion circuitry should be inserted between the controller output port and the target device. The circuit schematic is illustrated in Figure 55. In the signal-generating module, capacitances of C1 and C2 could control the oscillating frequency while the module input voltage regulated the oscillation amplitude. This shows that developing various signal-generating modules would greatly the applicability of the digital control system.

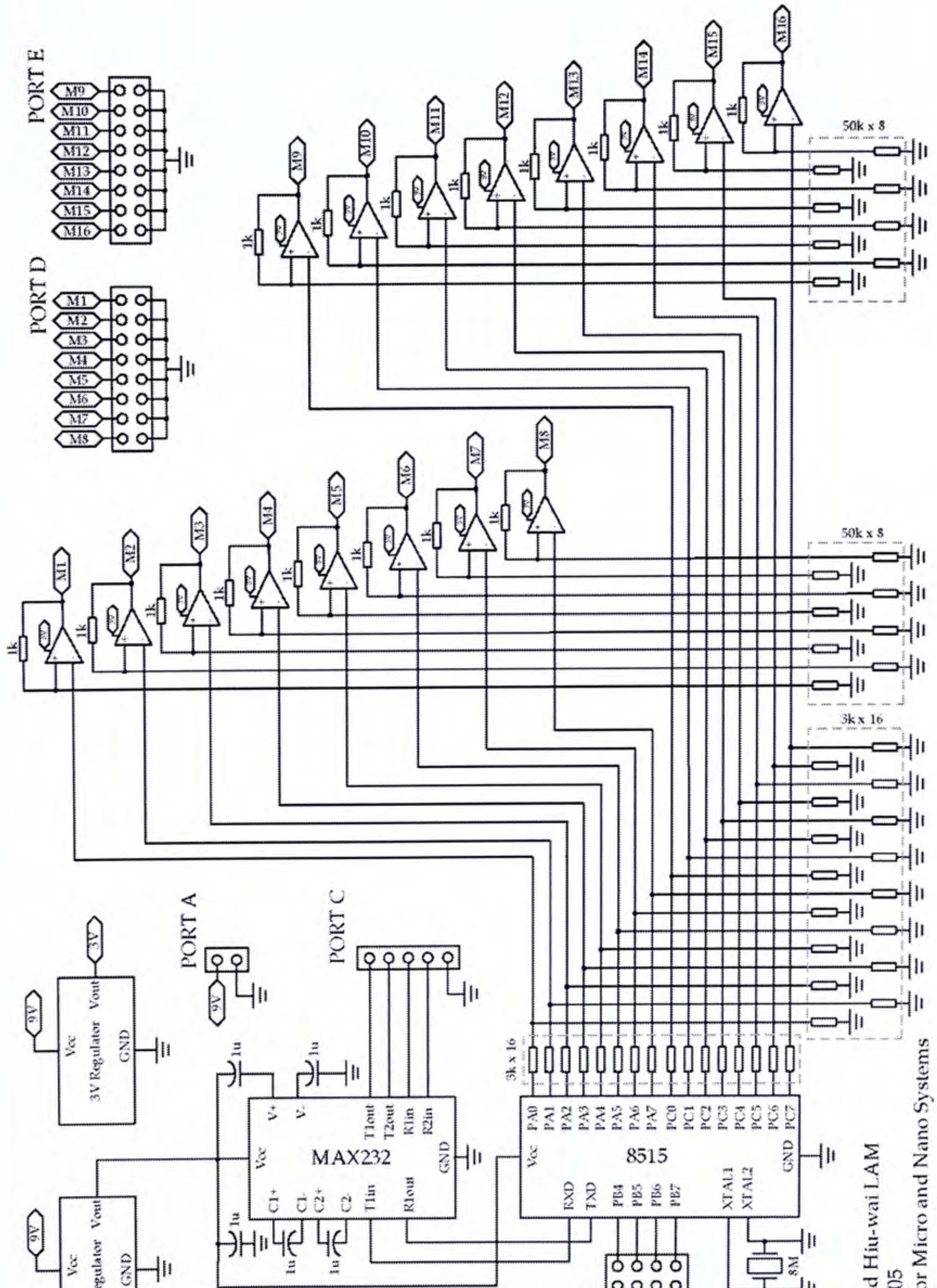

Figure 54. Schematic of the digital controller circuit.

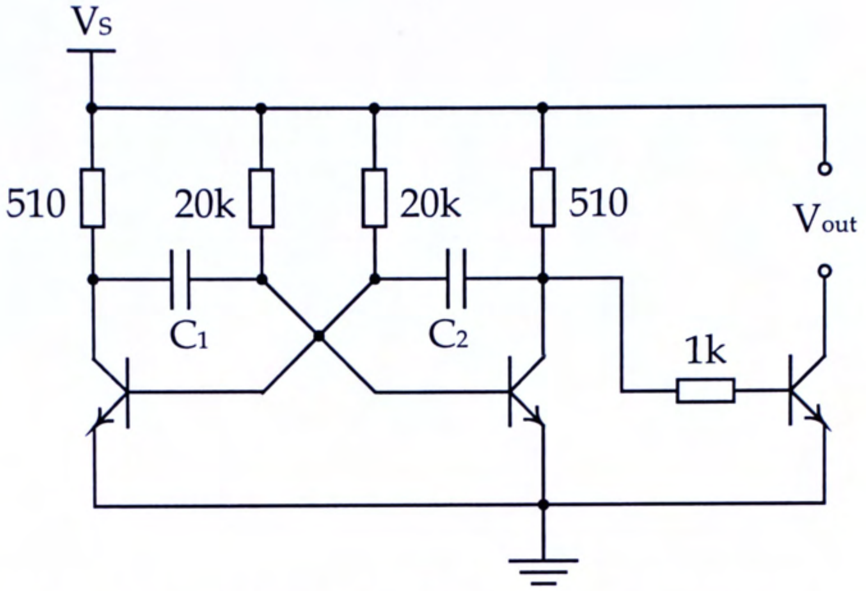

Figure 55. Circuit schematic of the oscillating signal generator.

APPENDIX
C

ADVANCED DIGITAL MICROFLUIDIC CONTROLLER

The fluid manipulation control circuit, which has been developed by Micro and Nano Automation Laboratory in Shenyang Institute of Automation recently, consists of a digital-to-analog (DA) interface card and a power amplifier board for the power control of motors (Figure 56 (a)). Multiple micropumps, up to sixteen channels, could be driven simultaneously using the control system. The built-in function of the interface card enabled the direct execution using a computer, which induced a faster response time than the serial port connection. A simple interface program was also developed. It was designed to generate real-time output signals with variable voltages and currents. An extended amplifier board was designed to control the output signals with sufficient driving currents (~1 A per channel) for the motors in the vortex micropumps. The board was mainly composed of sixteen PA60EU motor controllers with fast response (1.1 MHz bandwidth) and flexible outputs (bipolar voltage). The elementary circuit diagram for a controller unit is shown in Figure 56 (b). The voltage values from the interface card were fed to the positive input channel of the controller unit. The steady rotation of the micropump impellers could be accomplished by regulating the resistances of R1 and R2.

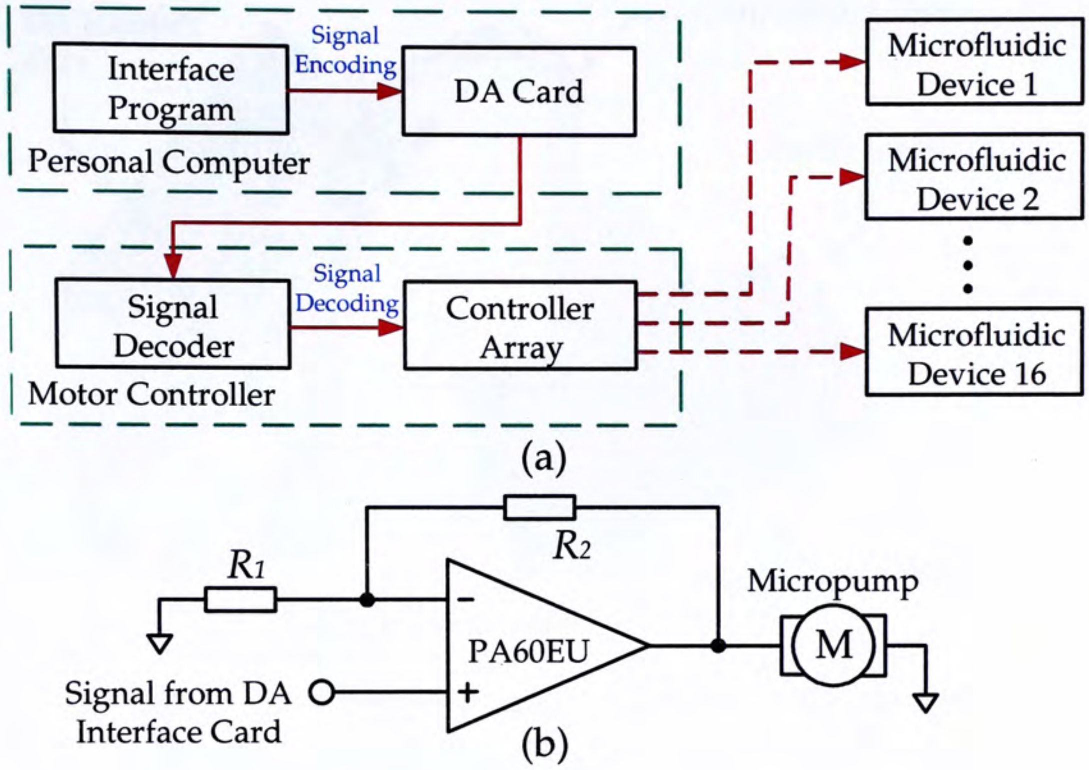

Figure 56. Schematics of (a) fluid manipulation control system and (b) controller unit.

The developed control system hardware is shown in Figure 57. The DA interface card supports sixteen output analog channels with 0 – 5 V voltage and 4 – 20 mA current. This system can have higher output stability because the signal processing ICs and voltage regulators are included in the card. Signals can be passed to the amplifier board via a connection cable. With further development of the interface program, it is believed that the control system could potentially generate different signal formats and operate various microfluidic devices.

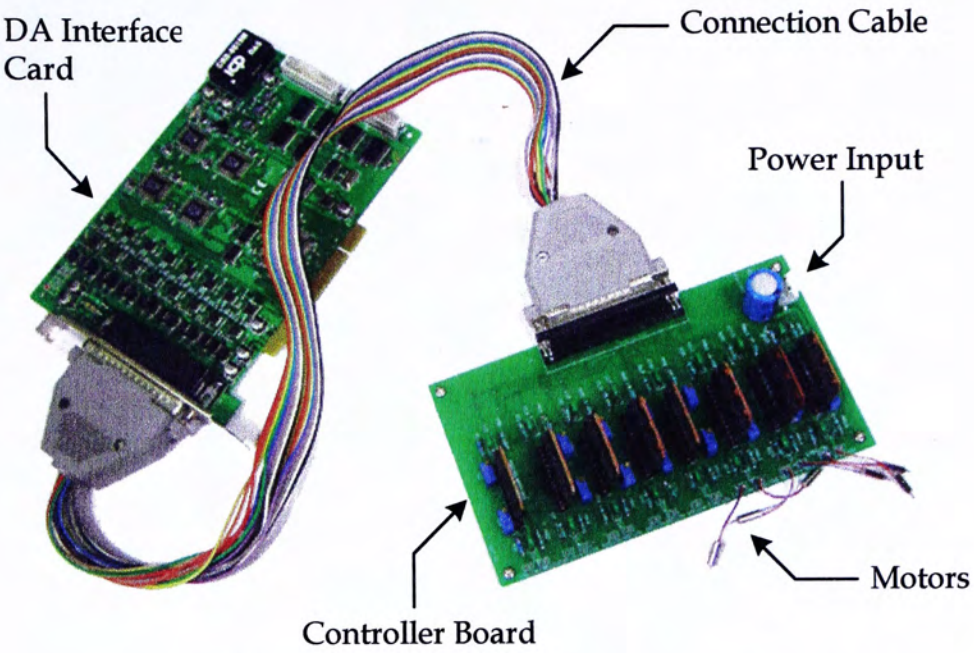

Figure 57. Interface card and circuit board of the advance digital controller for intergrated microfludic system.